AD-A074 701 NAVAL RESEARCH LAB WASHINGTON DC SHOCK AND VIBRATION--ETC F/G 20/11
THE SHOCK AND VIBRATION BULLETIN. PART 3. STRUCTURE MEDIUM INTE--ETC(U)
SEP 79
UNCLASSIFIED BULL-49-PT-3 NL

1 OF 2
ADA 074701

AD A074701

LEVEL II

Bulletin 49
(Part 3 of 3 Parts)

THE SHOCK AND VIBRATION BULLETIN

DDC
RECEIVED
OCT 5 1979
E

Part 3
Structure Medium Interaction,
Case Studies in Dynamics

SEPTEMBER 1979

A Publication of
THE SHOCK AND VIBRATION
INFORMATION CENTER
Naval Research Laboratory, Washington, D.C.

Office of
The Director of Defense
Research and Engineering

Approved for public release; distribution unlimited.

DDC FILE COPY

79 10 01 008

SYMPOSIUM MANAGEMENT

THE SHOCK AND VIBRATION INFORMATION CENTER

Henry C. Pusey, Director
Rudolph H. Volin
J. Gordan Showalter
Barbara Szymanski
Carol Healey

Bulletin Production

Graphic Arts Branch, Technical Information Division,
Naval Research Laboratory

Bulletin 49
(Part 3 of 3 Parts)

THE SHOCK AND VIBRATION BULLETIN

SEPTEMBER 1979

A Publication of
THE SHOCK AND VIBRATION
INFORMATION CENTER
Naval Research Laboratory, Washington, D.C.

The 49th Symposium on Shock and Vibration was held at the International Inn, Washington, DC on October 17-19, 1978. The NASA Goddard Space Flight Center, Greenbelt, Maryland, was the host.

Office of
The Director of Defense
Research and Engineering

CONTENTS

PAPERS APPEARING IN PART 3

STRUCTURE MEDIUM INTERACTION

FAILURE OF UNDERGROUND CONCRETE STRUCTURES SUBJECTED TO BLAST LOADINGS 1
C.A. Ross, University of Florida Graduate Engineering Center, Eglin AFB, FL, P.T. Nash and G.R. Griner, USAF Armament Laboratory, Eglin AFB, FL

OPTIMIZATION OF REINFORCED CONCRETE SLABS 11
J.M. Ferritto, Civil Engineering Laboratory, Naval Construction Battalion Center, Port Hueneme, CA

A NUMERICAL COMPARISON WITH AN EXACT SOLUTION FOR THE TRANSIENT RESPONSE OF A CYLINDER IMMERSED IN A FLUID 23
M.E. Giltrud and D.S. Lucas, Naval Surface Weapons Center, White Oak, Silver Spring, MD

CASE STUDIES IN DYNAMICS

FOIL SYSTEM FATIGUE LOAD ENVIRONMENTS FOR COMMERCIAL HYDROFOIL OPERATION 29
D.L. Graves, Boeing Marine Systems, Renton, WA

EVALUATION OF ROTOR-BEARING SYSTEM DYNAMIC RESPONSE TO UNBALANCE 41
R.E. Thaller and D.W. Ozimek, Aeronautical Systems Division, Wright-Patterson AFB, OH

SELECTED TOPICS FROM THE STRUCTURAL ACOUSTICS PROGRAM FOR THE B-1 AIRCRAFT 55
P.M. Belcher, Rockwell International Corporation, Los Angeles, CA

EXPERIMENTAL INVESTIGATION OF DYNAMIC CHARACTERISTICS OF TURBINE GENERATORS AND LOW-TUNED FOUNDATIONS 69
S.P. Ying and M.E. Forman, Gilbert/Commonwealth, Jackson, MI and R.R. Drumm, Pennsylvania Power and Light Company, Allentown, PA

COMBINED VIBRATION/TEMPERATURE/SIDELOAD ENVIRONMENTAL TESTING OF UHF BLADE ANTENNAS 79
R. Volker, McDonnell Douglas Corporation, St. Louis, MO

SHOCK ISOLATION PLATFORM FOR SEASPARROW LAUNCHER 85
P.V. Roberts, Raytheon Company, Bedford, MA

PAPERS APPEARING IN PART 1

FOREWORD
Henry C. Pusey, Director, Shock and Vibration Information Center, Naval Research Laboratory, Washington, DC

INVITED PAPERS

THE DYNAMICS OF THE DOD SCIENCE AND TECHNOLOGY PROGRAM
Dr. George P. Milburn, Office of the Deputy Director of Research and Engineering (Research and Advanced Technology), Washington, DC

THE DEVELOPMENT OF A METHOD FOR PREDICTING THE NOISE EXPOSURE OF PAYLOADS IN THE SPACE SHUTTLE ORBITER VEHICLE
John F. Wilby and Larry D. Pope, Bolt Beranek and Newman, Inc., Canoga Park, CA

Accession For
NTIS GRA&I
DDC TAB
Unannounced
Justification
By
Distribution/
Availability Codes
Dist. | Avail and/or special
A

VIBRATION AND ACOUSTICS

PROBABILITY OF FAILURE PREDICTION FOR STEP-STRESS FATIGUE UNDER SINE OR RANDOM STRESS
R.G. Lambert, General Electric Company, Utica, NY

ON THE USE OF COHERENCE FUNCTIONS TO EVALUATE SOURCES OF DYNAMIC EXCITATION
S. Barrett, Martin Marietta Corporation, Denver, CO

STATUS OF CAVITY NOISE PHENOMENA MEASUREMENT AND SUPPRESSION ON THE B-1 AIRCRAFT
A.G. Tipton and C.H. Hodson, Los Angeles Division, Rockwell International, El Segundo, CA

SPACE SHUTTLE SOLID ROCKET BOOSTER AFT SKIRT REENTRY NOISE INDUCED BY AN AERODYNAMIC CAVITY-FLOW INTERACTION
L.A. Schutzenhofer, P.W. Howard, W.W. Clever, and S.H. Guest, George C. Marshall Space Flight Center, Marshall Space Flight Center, AL

BLAST AND SHOCK

SNAPS IN STRUCTURES
M. Zak, Jet Propulsion Laboratory, California Institute of Technology, Pasadena, CA

A SIMPLIFIED METHOD OF EVALUATING THE STRESS WAVE ENVIRONMENT OF INTERNAL EQUIPMENT
J.D. Colton and T.P. Desmond, SRI International, Menlo Park, CA

HIGH G PYROTECHNIC SHOCK SIMULATION USING METAL-TO-METAL IMPACT
M. Bai and W. Thatcher, Motorola Government Electronics Division, Scottsdale, AZ

AN EXPERIMENTAL DESIGN FOR TOTAL CONTAINER IMPACT RESPONSE MODELING AT EXTREME TEMPERATURES
V.P. Kobler, U.S. Army Missile Research and Development Command, Huntsville, AL, and R.M. Wyskida, J.D. Johannes, The University of Alabama in Huntsville, Huntsville, AL

EMPIRICAL PROCEDURES FOR ESTIMATING RECOILLESS RIFLE BREECH BLAST OVERPRESSURES
P.S. Westine and R.E. Ricker, Southwest Research Institute, San Antonio, TX

BLAST FROM BURSTING FRANGIBLE PRESSURE SPHERES
E.D. Esparza and W.E. Baker, Southwest Research Institute, San Antonio, TX

TEST EVALUATION OF SHOCK BUFFERING CONCEPT FOR HYDRODYNAMIC RAM INDUCED BY YAWING PROJECTILE IMPACTING A SIMULATED INTEGRAL FUEL TANK
P.H. Zabel, Southwest Research Institute, San Antonio, TX

PREDICTION OF FRAGMENT VELOCITIES AND TRAJECTORIES
J.J. Kulesz, L.M. Vargas, and P.I. Moseley, Southwest Research Institute, San Antonio, TX

PAPERS APPEARING IN PART 2

MODAL AND IMPEDANCE ANALYSIS

AN IMPEDANCE TECHNIQUE FOR DETERMINING LOW FREQUENCY PAYLOAD ENVIRONMENTS
K.R. Payne, Martin Marietta Corporation, Denver, CO

A STATISTICAL LOOK AT MODAL DISPLACEMENT RESPONSE TO SEQUENTIAL EXCITATIONS
W.J. Kacena, Martin Marietta Corporation, Denver, CO

ON DETERMINING THE NUMBER OF DOMINANT MODES IN SINUSOIDAL STRUCTURAL RESPONSE
W.L. Hallauer, Jr., and A. Franck, Department of Aerospace and Ocean Engineering, Virginia Polytechnic Institute and State University, Blacksburg, VA

LATERAL AND TILT WHIRL MODES OF FLEXIBLY MOUNTED FLYWHEEL SYSTEMS
C.W. Bert and T.L.C. Chen, School of Aerospace, Mechanical and Nuclear Engineering, The University of Oklahoma, Norman, OK

HUMAN RESPONSE TO VIBRATION AND SHOCK

WHOLE-BODY VIBRATION OF HEAVY EQUIPMENT OPERATORS
D.E. Wasserman, W.C. Asburry, and T.E. Doyle, National Institute for Occupational Safety and Health, Cincinnati, OH

RESEARCH RELATED TO THE EXPANSION AND IMPROVEMENT OF HUMAN VIBRATION EXPOSURE CRITERIA
R.W. Shoenberger, Aerospace Medical Research Laboratory, Aerospace Medical Division, Wright-Patterson AFB, OH

ISOLATION AND DAMPING

COMPUTER AIDED DESIGN OF PASSIVE VIBRATION ISOLATORS FOR AIRBORNE ELECTRO-OPTICAL SYSTEMS
P.W. Whaley, Air Force Institute of Technology, Wright-Patterson AFB, OH and J. Pearson, Air Force Flight Dynamics Laboratory, Wright-Patterson AFB, OH

DESIGN OF TURBINE BLADES FOR EFFECTIVE SLIP DAMPING AT HIGH ROTATIONAL SPEEDS
D.I.G. Jones, Air Force Materials Laboratory, Wright-Patterson AFB, OH and A. Muszynska, Institute of Fundamental Technological Research, Polish Academy of Sciences, Warsaw, Poland

A SIMPLE LOW-COST TECHNIQUE FOR MEASURING MATERIAL DAMPING BEHAVIOR
D.I.G. Jones, Air Force Materials Laboratory, Wright-Patterson AFB, OH

THE EFFECTS OF FREQUENCY, AMPLITUDE, AND LOAD ON THE DYNAMIC PROPERTIES OF ELASTOMERS
J.E. Cole, III, Cambridge Acoustical Associates, Inc., Cambridge, MA

LIQUID SPRING SHOCK ISOLATOR MODELING BY SYSTEM IDENTIFICATION .....
P.H. Sonnenburg, B.H. Wendler, and W.E. Fisher, The U.S. Army Corps of Engineers, Construction Engineering Research Laboratory, Champaign, IL

A GENERALIZED DERIVATIVE MODEL FOR AN ELASTOMER DAMPER .....
R.L. Bagley and P.J. Torvik, Air Force Institute of Technology, Wright-Patterson AFB, OH

SHOCK RESPONSE OF NON-LINEAR SYSTEMS
K. Peleg, Schook of Packaging, Michigan State University, East Lansing, MI

DYNAMIC ANALYSIS

STABILITY ANALYSIS AND RESPONSE CHARACTERISTICS OF TWO-DEGREE OF FREEDOM NONLINEAR SYSTEMS
M. Subudhi and J.R. Curreri, Brookhaven National Laboratory, Upton, NY

APPLICATION OF RANDOM TIME DOMAIN ANALYSIS TO DYNAMIC FLIGHT MEASUREMENTS
S.R. Ibrahim, Department of Mechanical Engineering and Mechanics, Old Dominion University, Norfolk, VA

SHOCK SPECTRA DESIGN METHODS FOR EQUIPMENT-STRUCTURE SYSTEMS
J.M. Kelly and J.L. Sackman, University of California, Berkeley, Berkeley, CA

A COMPUTATIONAL MODEL DESCRIBING THE INITIATION OF SILVER ACETYLIDE-SILVER NITRATE EXPLOSIVE BY AN INTENSE LIGHT SOURCE
F.H. Mathews, Sandia Laboratories, Albuquerque, NM

TERMINAL VELOCITY AND ROTATION RATE OF A FLYER PLATE PROPELLED BY A TUBE-CONFINED EXPLOSIVE CHARGE
R.A. Benham, Sandia Laboratories, Albuquerque, NM

A STABILITY THEOREM FOR A DYNAMICALLY LOADED LINEAR VISCOELASTIC STRUCTURE
D.W. Nicholson, Naval Surface Weapons Center, White Oak, Silver Spring, MD

ANALOG DOUBLE INTEGRATION OF SHOCK PULSES
K. Peleg, School of Packaging, Michigan State University, East Lansing, MI and R.A. Lund, MTS Systems Corporation, Minneapolis, MN

TITLES AND AUTHORS OF APPERS PRESENTED IN THE SHORT DISCUSSION TOPICS SESSION

NOTE: These papers were only presented at the Symposium. They are not published in the Bulletin and are only listed here as a convenience.

RESEARCH IN COLLISION DYNAMICS OF SURFACE SHIPS
M.P. Pakstys, General Dynamics, Groton, CT

FORCED VIBRATION RESONATORS AND VIBRATIONS OF THE SHIP
G. Volcy, Bureau Veritas, Paris, France

RINGING PLATE SIMULATION OF PYROTECHNIC SHOCKS
S.H. Neff, Sandia Laboratories, Albuquerque, NM

QUARTZ CRYSTAL RESONATORS FOR HIGH G ENVIRONMENTS
R.L. Filler, ET&D Laboratory, Fort Monmouth, NJ

THE BENCHLESS LASER
J. Pearson, Air Force Flight Dynamics Laboratory, Wright-Patterson AFB, OH

PULSED HOLOGRAPHIC ANALYSIS OF LARGE VEHICLE COMPONENTS
G. Arutunian and G.R. Gerhart, U.S. Army Tank Automotive Research and Development Command, Warren, MI

CALIBRATION OF SHOCK AND VIBRATION MEASURING TRANSDUCERS
R.R. Bouche, Bouche Laboratories, Sun Valley, CA

CRITICAL SPEEDS OF MULTITHROW NONUNIFORM CRANKSHAFTS USING SPATIAL FINITE LINE ELEMENT TECHNIQUE
C. Bagci, Tennessee Tech. University, Cookeville, TN

VIBRATION OF INPLANE LOADED ISOTROPIC AND ORTHOTROPIC RECTANGULAR PLATES
S.M. Dickinson, The University of Western Ontario, London, Ontario, Canada

ATTENUATION OF VIBRATIONS IN VISCOELASTIC SOLIDS CONTAINING MULTIPLE DEFECTS
M.P. Wnuk, South Dakota University, Brookings, SD

SOLVING PC-CARD VIBRATION PROBLEMS WITH UNIQUE DAMPING APPLICATIONS
W.J. Vitaliano, Harris GISD, Melbourne, FL

MINI COMPUTER SWEPT SINUSOIDAL DATA PROCESSING TECHNIQUES
F.E. Anderson, U.S. Army Missile R&D Command, Redstone Arsenal, AL

SHUTTLE PAYLOADS TEST FACILITIES
E.J. Kirchman, NASA Goddard Space Flight Center, Greenbelt, MD

AERODYNAMIC COUPLING BETWEEN CLOSELY SPACED PANELS
C.V. Stahel, Jr., General Electric Company, Philadelphia, PA

UPDATE ON COMBINED ENVIRONMENT GROWTH TESTING OF A BLACK BOX
J. Hutchinson, Vought Corporation, Dallas, TX

FAILURE OF UNDERGROUND CONCRETE STRUCTURES SUBJECTED TO BLAST LOADINGS*

C. A. Ross
University of Florida Graduate Engineering Center
Eglin AFB, Florida 32542

and

P. T. Nash and G. R. Griner
USAF Armament Laboratory
Eglin AFB, Florida 32542

This study presents the results of analytical predictions of response and failure of two-edges-free reinforced concrete slabs subjected to intermediate blast loadings. Approximate theoretical methods using stationary and moving plastic hinge mechanisms with linearly varying and time dependent loadings are developed. Reasonable agreement between analysis and experimental observations was obtained.

INTRODUCTION

Failure of reinforced concrete structures, as well as other structural elements subjected to distributed normal loads, may be defined in terms of the degree of damage. In this study failure of reinforced concrete structures will be defined as a condition where actual separation or fracture of the reinforcing elements has occurred. This essentially means the structure will have been rendered almost completely incapable of any load carrying ability. To reach this damage level the reinforcing elements at the failed position will have passed through the yield and ultimate stresses. For this type condition a reasonable assumption is that the tensile strength of the concrete is negligible when compared to the strength of the reinforcing elements. Failure in this case is then based on the ultimate strength or elongation of the reinforcing elements. For plates and beams with transverse loads where bending is present, an idealized rigid perfectly plastic stress-strain assumption may be used to estimate the true moment carrying capacity of the structure. This assumption is justified for ductile steel reinforcing elements whose true stress-strain relation shows a rather small elastic portion when compared to the overall stress-strain diagram. The "fully plastic" or "ultimate" moment as applied to statically loaded reinforced concrete beams and plates is summarized by Szilard [1]. The "fully plastic moment" and "plastic hinge" for metal beams is covered in detail by Timoshenko and Gere [2] and plastic hinges and yield lines as applied to reinforced concrete beams are shown in some detail in [1]. Abrahamson, et al [3] used both stationary and moving plastic hinges to describe the deformation process of thin metal beams subjected to various kinds of transverse dynamic pressure loadings. Jones [4] used this simple rigid-plastic method to successfully predict the large inelastic behavior of thin metal beams when subjected to impulsive loads and analytically verified the experimental work of Menkes and Opat [5].

Experimental evidence of Fuehrer and Keeser [6] shows that buried reinforced concrete beams exhibit a plastic hinge type deformation when subjected to a small underground explosion of close proximity. The results of this experimental program [6] show two kinds of failure; 1) a beam failure, with a

*This study funded by the Joint Technical Coordinating Group/Surface Target Survivability Vulnerability Program through USAF Office of Scientific Research Grant 78-3592 in cooperation with the USAF Armament Laboratory, Eglin AFB, Florida.

plastic hinge on each end and in the middle, with no appreciable concrete cracking elsewhere, associated with lowered pressure loads, and 2) failure of reinforcing elements at sides and middle with large areas of cracked concrete over the interior section of the beam showing evidence of moving hinges associated with loadings larger than those of number 1 above. The failure associated with complete shearing at the ends was not evidenced but should not be discounted as the loadings may not have approached those necessary for complete end shearing. Based on the experimentally determined failure modes described above, a study was initiated to analytically describe these type failure modes and predict reinforced concrete beam deflections and failures. The approach to be used was chosen as the previously described plastic hinge methods and the remainder of this paper is concerned with development and results obtained by this analytical approach.

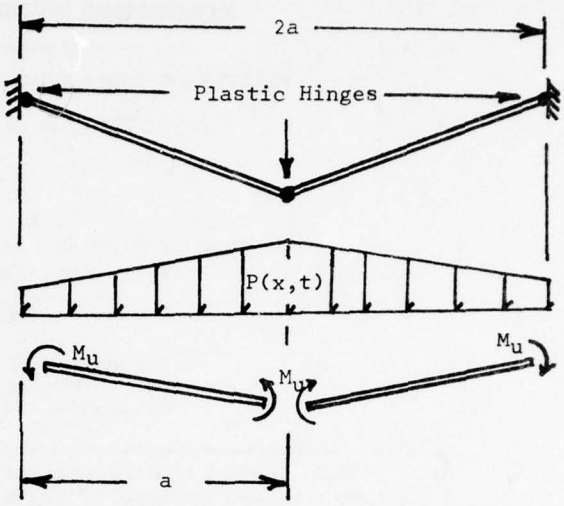

Figure 1a. Mechanism 1, showing stationary hinges at ends and midspan M_u=hinge moment per unit length.

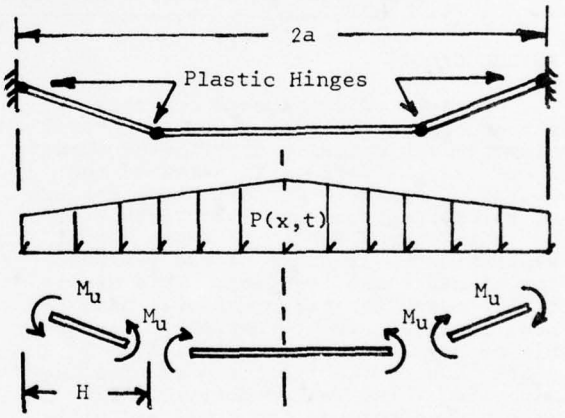

Figure 1b. Mechanism 2, showing stationary hinges at ends and two traveling hinges.

ANALYSIS

Based on a method used by Abrahamson [3], using two failure mechanisms as shown in Figure 1 for fixed end beams with a linear load distribution of Figure 2, equations have been developed to predict deflection and failure of reinforced concrete beams. The beam loading shown in Figure 2 is assumed linear spatially and every point on the beam has the same time variation given as

$$f(t) = (1-t/\tau)\exp(-\alpha t/\tau) \qquad (1)$$

where t is time, α is a dimensionless decay constant and τ is the length of the pressure pulse in seconds. The loading is expressed in terms of a uniform loading denoted by P_E at the edges and a uniformly varying triangular load of magnitude P_C at the center and zero at the edges. These loads are assumed constant across the beam width b. Using Figure 2 the beam loading, in force per area of the beam, at a distance x from the beam end is given as

$$P(x,t) = (P_E+P_C\frac{x}{a})f(t)$$

$$\text{for } 0 \le x \le a \text{ and } 0 \le t \le \tau \qquad (2)$$

$$P(x,t) = 0 \text{ for all } x \text{ and } t>\tau$$

where f(t) is given by Equation (1).

The equation of motion for mechanism 1 is given by

$$\theta = \frac{f(t)}{2ma}(3P_E+2P_C) - \frac{3nw}{2ma} - \frac{3FM_u}{ma^3} \qquad 0 \le t \le \tau \quad (3)$$

$$\theta = -\frac{3nw}{2ma} - \frac{3FM_u}{ma^3} \qquad t>\tau$$

where θ is the angular rotation in radians at the hinge moment as shown in Figure 3, M_u is the plastic hinge moment/unit length, m is the beam mass per unit area, w is the weight per unit area, F

is edge fixity term, and n determines loading direction. F equals 1.0 for simply supported edges and 2.0 for fixed edges. The load direction indicator n equals +1, -1, 0 for beams with loads from above, from below, and vertical beams respectively. The center point deflections and velocity are given as

$$\dot{\Delta} = \dot{\theta}a, \quad \Delta = \theta a \tag{4}$$

where a is the beam half span.

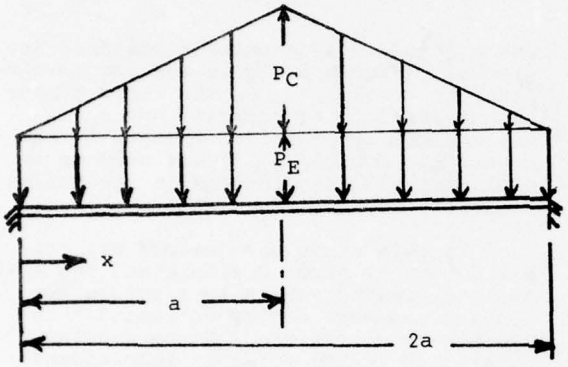

Figure 2. Beam loading for linearly varying load. P_C, P_E, force per unit area.

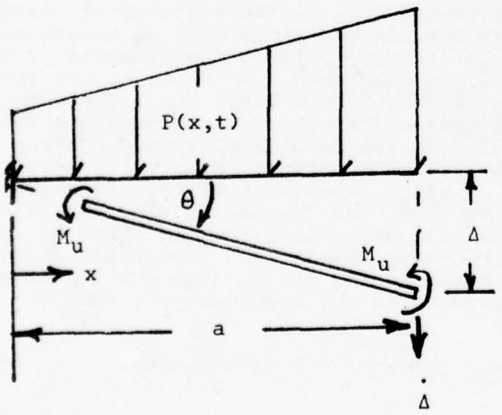

Figure 3. Beam notation and deflection for mechanism 1.

The equation of motion for the flat center portion is given by

$$\ddot{\Delta} = \frac{f(t)}{m}\left(P_E+\frac{P_C}{2}\right)-\frac{nw}{m}, \quad 0<H\leq a, \ 0\leq t\leq\tau,$$
$$\ddot{\Delta} = 0, \quad t>\tau, \tag{5}$$

where H is the hinge location.

Using the assumption of zero shear at the hinge the equation of motion for rotation of the outer portion of length H has been determined to be

$$\ddot{\theta} = \frac{ft}{2mH}\left(3P_E+2\frac{H}{a}P_C\right)-\frac{3nw}{2m}-\frac{3FM_u}{mH^3}, \quad 0<H\leq a, \ 0\leq t\leq\tau,$$
$$\ddot{\theta} = -\frac{3nw}{2m}-\frac{3FM_u}{mH^3}, \quad t>\tau. \tag{6}$$

Equations (6) reduces to Equation (3) when H reaches a and a beam deforming initially in a mechanism 2 mode will reduce to a mechanism 1 mode in the final stages of the deflection process. Equations (5) and (6) are coupled through the continuity condition that

$$\Delta = H\theta$$

and

$$\dot{\Delta} = \dot{H}\theta \tag{7}$$

The initial hinge location H_0 may be determined by the initial condition that

$$\left(\ddot{\Delta} = H_0\ \ddot{\theta}\right)_{t=0} \tag{8}$$

where H_0 is the initial hinge location for $t = 0$. Applying the initial condition of Equation (8) results in an equation from which the initial hinge location is determined knowing the applied loads and the hinge moment M_u. The equation for H_0 is given as

$$\frac{H_0^2}{2}\left[P_E+P_C\left(\frac{H_0}{a}-1\right)-nw\right] = 3FM_u. \tag{9}$$

The static collapse load P_{ES} (at edge of beam) for a mechanism 1 mode is that load required to produce a bending moment M_u at the ends or midpoint of the beam. For the loading assumed with $K = P_C/P_E$,

$$P_{ES} = \frac{12M_u}{a^2(2K+3)}. \tag{10}$$

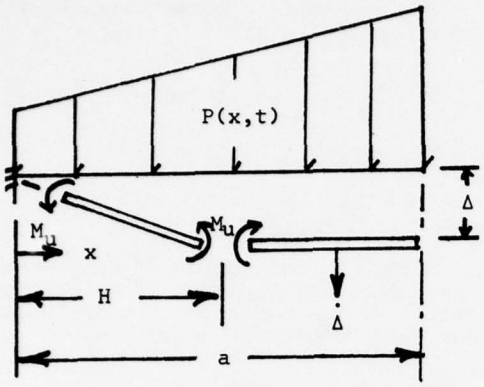

Figure 4. Beam notation and deflection for mechanism 1.

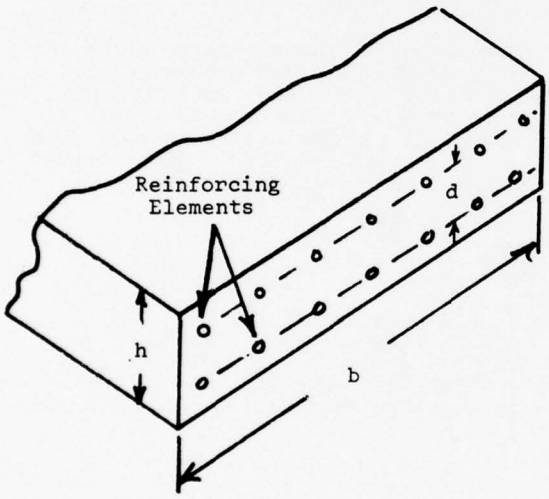

Figure 5. Beam cross section used for calculating M_u.

Solving Equation (10) for M_u and substituting into the right hand side of equation (9) results in

$$Y^2[1+K(Y-1)-nw] = \frac{(2K+3)F}{2\lambda} \qquad (11)$$

where $Y = H_0/a$ and λ is the ratio of the applied edge load P_E to the center load P_{ES} required for static collapse. The solution for $K = 0$ results in $Y = 1$ for $\lambda = 3$ which agrees with the results of Abrahamson, et al [3] for the uniformly loaded fixed end vertical beam. The solution of equation (12) then dictates the mechanism and type of equations of motion to be used. For $0<Y<a$ equations (5), (6) and (7) are used and for $Y = 1$ equations (3) and (4) are used. Solutions where $Y>1$ the mechanism 1 solution is used. As $\lambda\to\infty$, $Y\to 0$, therefore very large values of λ are not allowed in these solutions.

The plastic or hinge moment is given by Szilard [1] as

$$M_0 = 0.9\ [d^2\, q\, \sigma_R (1-0.59 q \sigma r/\sigma_C)] \qquad (12)$$

where d is distance between reinforcing elements (Figure 5), q is the reinforcing ratio in tension, σ_R is the yield stress of the reinforcing material and σ_C is the maximum compression strength of the concrete. Equation (12) was used as a basis for all calculations in the following sections.

In this study the failure criteria was chosen as steel fracture and the localized plastic strain to fracture appears to be more easily estimated than the stress at failure. Since angular rotation θ is the foremost independent parameter, strain in the reinforcing element will be expressed in terms of the rotation. In the usual manner strain will be presented in two parts, i.e. ε_t strain due to change in length and ε_b strain due to rotation. The deformed length ℓ at the plastic hinges for homogeneous metal beams [4] was assumed to be some multiple or fraction of the thickness. In this case the deformed length of the reinforcing elements at the plastic hinge will be chosen as the distance between the elements of the reinforcing mesh. This assumption seems justified on the basis that, although the free distance of an element in tension is imbedded in concrete, contraction due to Poisson effect will occur and allow elongation of the element between the two transverse adjacent parallel reinforcing elements fixed in the concrete. Neglecting higher order terms, change in the halfspan length may be approximated for a mechanism 1 mode as

$$\delta = \sqrt{\Delta^2+a^2} - a = a\left(1+\frac{1}{2}\frac{\Delta^2}{a^2}+\cdots-1\right) \qquad (13)$$

$$\simeq \frac{\Delta^2}{2a}$$

where a is the halfspan length and Δ is the midspan deflection. If half of this change takes place at the end support and the remainder at the midspan, then

δ is given in terms of ε_t and ℓ as

$$\delta = \varepsilon_t \ell = a\left(\frac{\Delta^2}{4a^2}\right) \tag{14}$$

The rotation Θ may be expressed as $\Theta = \Delta/a$ and the strain ε_t becomes

$$\varepsilon_t = \frac{a\Theta^2}{4\ell} \tag{15}$$

The strain ε_b due to bending at the plastic hinge may be expressed as d/2R where R is the radius of curvature and d is the distance between the reinforcing mats as shown in Figure 6. The radius of curvature is defined by

$$\ell = R\,\Theta \tag{16}$$

and the strain due to bending becomes

$$\varepsilon_b = \Theta d/2\ell \tag{17}$$

The total strain ε may be written as

$$\varepsilon = \varepsilon_t + \varepsilon_b = \frac{\theta a}{\ell}\left(\frac{\theta}{4} + \frac{d}{2a}\right) \tag{18}$$

A similiar equation may be determined for the mechanism 2 case where H the current hinge position is used in place of the midspan length a.

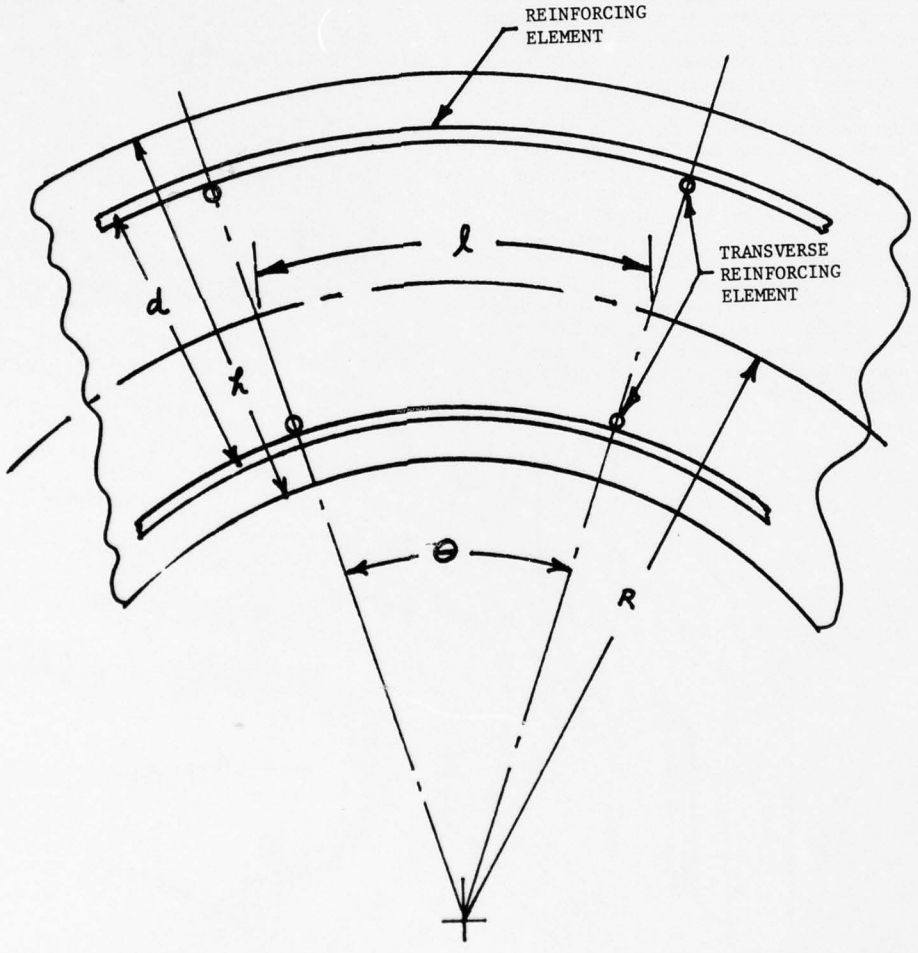

Figure 6. Schematic of slab thickness showing notation, arrangement of reinforcing elements and the assumed hinge length.

EXPERIMENTAL TESTS

Tests [6] were performed on several sizes of reinforced slabs with two edges fixed and selected specimens from these tests are presented here for comparison with analytical results.

The specimens were fabricated using 6000 psi compression concrete reinforced with a steel wire 4 in x 4 in (10.16 x 10.16 cm) mesh both top and bottom. Additional reinforcements were placed at the ends of the specimens as seen in the fractured specimen of Figure 13. The general schematic of test specimens is shown in Figure 7 and a test specimen in place is shown in the photograph of Figure 8. The legs of the specimen were placed against an upright concrete wall and were prevented from parallel outward motion at the wall by steel angles as shown in Figure 8. The explosive charge was placed on a line normal to and at various distances from the center of the slab. Pressure wave speeds were measured at various distances from the charge.

All tests were performed with the test specimen vertical. The specimens were then covered and packed with soil to a height approximately 3 ft (.91m) above the top of the specimen. This experimental configuration eliminated the weight of overburden. The top of the upright specimen was covered to prevent backfill behind the test slab.

RESULTS AND DISCUSSION

The deflection or rotation of the slab may be determined using equations (3) or (5) and (6), however the key to the initial response is found using equation (11). The initial position of the plastic hinge Y may be found using equation (11) and this position is necessary if a solution of deflection versus time is required.

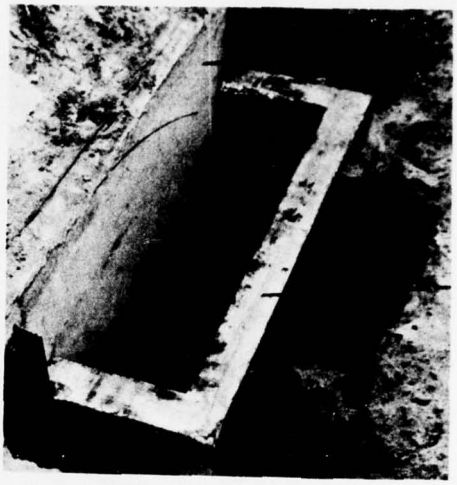

Figure8. Photograph showing topsoil removed with test specimen in place.

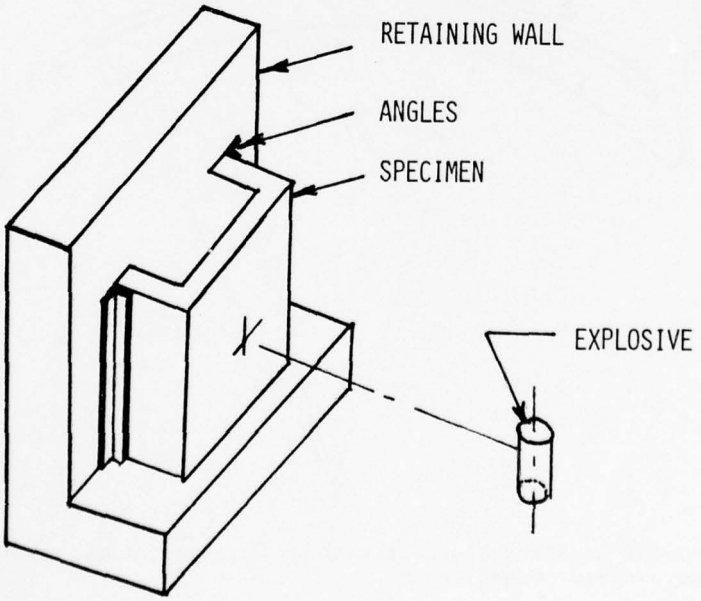

Figure 7. Schematic of test setup with soil removed. Test arrangement is completely covered with soil before tests.

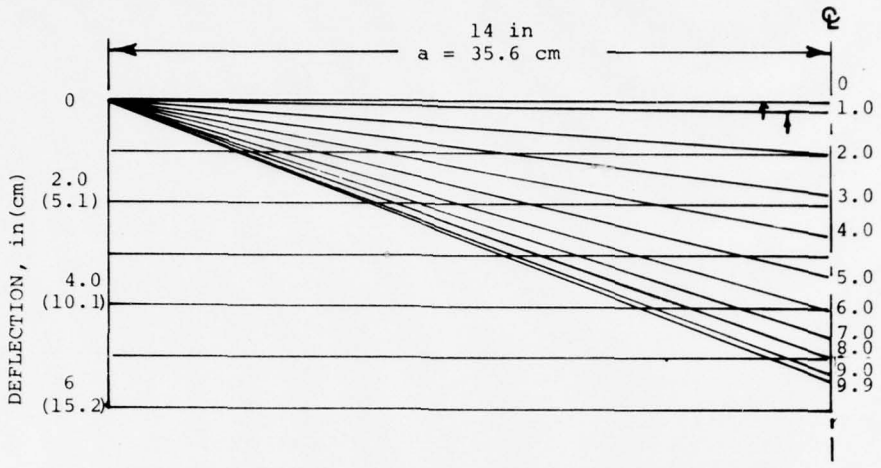

Figure 9. Calculated deflection-time curves for Case 1. Deflection scaled to length of beam as shown. Numbers to right give time in milliseconds for each curve Arrow indicates position of moving hinge.

Figure 10. Post-test photograph of Case 1.

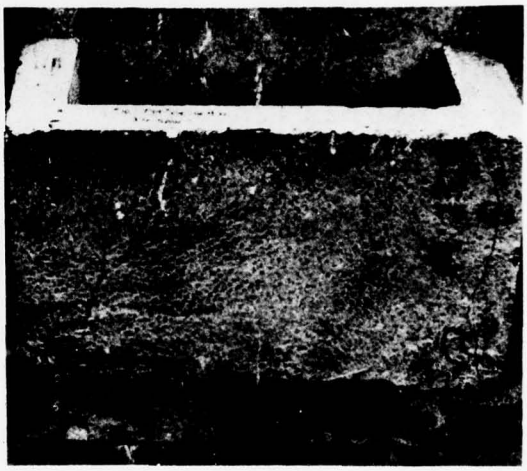

Figure 11. Post-test photograph of Case 2.

However a simple check on the expected response may be determined, for example, on a fixed end beam, by letting Y=1, F=2, n=0, and solving for $\lambda=2K+3$, which is the boundary between the mechanism 1 and mechanism 2 initial response. Therefore for $\lambda \leq (2K+3)$ the initial response is by mechanism 1 and for $\lambda > (2K+3)$ the initial response is by mechanism 2. The use of equation (11) in the determination of the initial response mechanism requires the maximum pressure of the pressure loading, as well as the pressure distribution over the slab. The general shape of the pulse is necessary for a complete solution however general relations for certain cases similiar to those of reference [3] may be written using only the impulse and peak pressure of the pressure loading. The pressure loadings used were estimated from the measured pressure time curves of reference [6]. Well-defined pressure loadings are desired due to the requirement for

initial peak loading and total impulse, however, only estimates were available.

Equations (1) through (12) have been coded and solutions of the three cases given below in Table I were programmed. The analytical predicted response of Case 1 is shown in a scaled drawing of Figure 9 and the experimental final position and failure of this same slab is shown in Figure 10. Analytical prediction of Case 2 gave a maximum midspan deflection of approximately 1.0 inch (2.54 cm). Experimentally, one test of Case 2 showed about 1.5 inch (3.81 cm) midspan deflection, however, a second test, shown in Figure 11, indicates no deflection and minimal cracking. The analysis of Case 3 gives a mechanism 2 initial response and the response-time relation is shown in the scaled drawing of Figure 12. The final experimental deflection for Case 3 is shown in Figure 13.

Using the failure criteria as presented in the Analysis Section, the rotation for failure θ_m may be determined if the strain to failure ϵ_m is known. Post failure observations show that the distance between reinforcing elements is a reasonable estimate of the deformed hinge width.

Fractures of the reinforcing elements occur either at the welds of the mesh or at localized points between the welds. Post test measurements of reinforcing elements show a very localized reduction in area near the fracture point with very little or no plastic deformation at positions away from the fracture point. Laboratory measurements on the mesh verified the post test measurements and deflection load curves indicate a yield/ultimate of 60,000-70,000 psi (414 - 483 MPa) and a strain to failure of 0.10 to 0.15.

Using an experimentally observed strain to failure of 0.125 and equation (19) gives a rotation to failure of 0.22 radians for a 28 in (.71 m) slab initially deforming in a mechanism 1 mode. Experimental evidence shows that for the 28 in (.71 m) long slabs some reinforcing steel was fractured for all rotations above 0.20 radians.

Mathematically, the distinction between mechanism 1 and mechanism 2 is a line, however, for a real structure, where the hinge may only have to fall within half the hinge length of the midspan to be classified as a mechanism 1 mode. For Case 1, the predicted initial hinge location was found to be only about 10% of the half span from the center and the response mode is distinctly mechanism 1 as shown in Figure 10. However, for the Case 3 the free span is so short it is difficult to determine what

TABLE I

REINFORCED CONCRETE SLAB TEST, 2% STEEL, FIXED TWO EDGES.

CASE	Effective Size ft(m)	Explosive Size lbs (kg)	Explosive Distance ft(m)	P_C psi (MP_a)	P_E psi (MP_a)	τ Sec	α
1	3X2.33X.33 (.91X.71X.1)	8 (3.63)	3 (.91)	140 (.97)	420 (2.90)	.015	6
2	3X2.33X.33 (.91X.71X.1)	8 (3.63)	4 (1.22)	50 (.34)	190 (1.31)	.015	2
3	3X1.33X.33 (.91X.41X.1)	8 (3.63)	2 (.61)	380 (2.62)	1520 (10.48)	.015	30

initial mode shape really occurred although the predicted initial hinge location was about 20% of the length of the span from the center. Much better success is expected for prediction of actual beam response rather than the slabs as presented here.

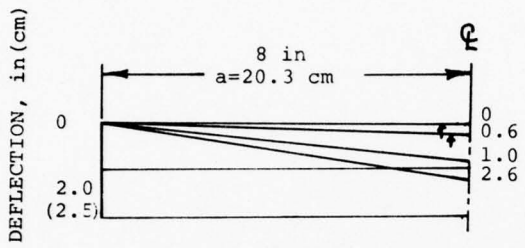

Figure 12. Calculated deflection-time curves for Case 3. Deflection sealed to length of beam shown. Numbers to right give time in milliseconds for each curve Arrows indicate position of moving hinge.

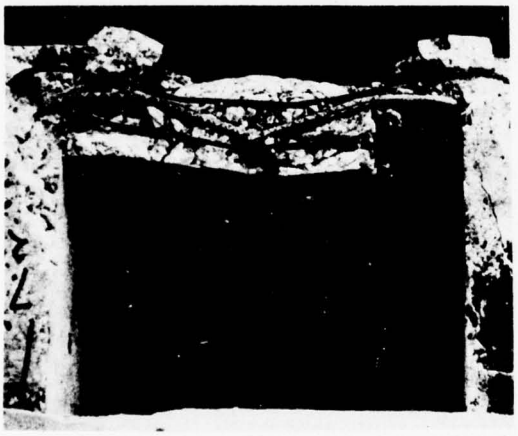

Figure 13. Post-test photograph of Case 3.

At present the analysis predicts response using the constant hinge moments as resistive forces and fracture of the tensile steel may be determined by monitoring the rotation. If fracture of the steel occurs while the structure still has considerable kinetic energy, the reduced resistive force will give rise to a larger experimental deflection than that predicted analytically. This is evidenced by the large experimental deflection of Case 1.

However, due to the simplified motion of the model, adjustments in resistive forces, after fracture first occurs, could be made to predict failure of the remaining steel, especially for the mechanism 1 mode. Experimentally, the steel at the midspan fractures first and is probably due to the fact that the majority of the membrane strain associated with increased slab length occurs at midspan and not at fixed ends. Also, the failure of the remaining steel appears to occur at midspan first and is attributable to the translational inertia and increased length at the midspan as compared to simple rotation at the edges.

SUMMARY AND CONCLUSIONS

Experimental observations indicate that failure of underground reinforced concrete slabs, for slabs with thickness approximately 25% of length, occurs by plastic hinges or hinge lines when subjected to intermediate blast loadings. Modelling using plastic hinges and hinge lines shows promise as an analytical tool for predicting fracture of the reinforcing steel in tension. Care must be exercised in that intense or high peaked loadings may cause complete concrete fracture or shear type fractures taking place at edges before appreciable response takes place.

REFERENCES

1. Szilard, R., Theory and Analysis of Plates, Prentice-Hall, Inc., 1974, pp. 571-612.

2. Timoshenko, S. P., and Gere, J. M., Mechanics of Materials, Van Nostrand Reinhold Co., 1972, pp. 289-316.

3. Abrahamson, G. R., Florence, A. L., and Lindberg, H. E., "Radiation Damage Study (RADS) - Vol. XIII, Dynamic Response of Beams, Plates and Shells," BSDTR 66-372, Vol. XIII, Ballistics System Div., Norton AFB, CA, Sept. 1966.

4. Jones, N., "Plastic Failure of Ductile Beams Loaded Dynamically," J. of Eng. for Industry. TRANS. ASME, Vol. 98, Series B, No. 1, Feb. 1976, pp. 131-136.

5. Menkes, S. B. and Opat, H. J., "Broken Beams," Experimental Mechanics, Vol. 13, 1973, pp. 480-486.

6. Fuhrer, H. R., and Kesser, J. W., "Response of Buried Concrete Slabs to Underground Explosions," AFATL TR-77-115, USAF Armament Lab., Eglin AFB, FL, Sept. 1977.

OPTIMIZATION OF REINFORCED CONCRETE SLABS

J. M. Ferritto
Civil Engineering Laboratory
Naval Construction Battalion Center
Port Hueneme, California

The Department of Defense uses reinforced concrete cells composed of concrete slabs to limit the effects of accidental explosions during hazardous explosives operations. An automated design procedure is discussed which considers the dynamic nonlinear behavior of the reinforced concrete of arbitrary geometrical and structural configuration subjected to dynamic pressure loading. Optimum design of the slab is accomplished by use of an interior penalty function. The paper discusses the optimization procedure and a discussion of the results is given. The results are compared with finite element analysis.

INTRODUCTION

The Department of Defense has numerous facilities engaged in the production of various types of explosives and munitions used by military services. In most cases the production of ammunition utilizes assembly line procedures. Projectiles pass through various stages of preparation: filling with explosive, fuzing, marking, and packing. Hazardous operations, such as the filling of the projectile case with an explosive in a powder form and the compaction of the powder by hydraulic press, are accomplished in protective cells that are intended to confine the effects of an accidental explosion.

Most of the existing production facilities were built in the 1940s. With few exceptions, the manufacturing technology and existing equipment represent the state of the art as of 1940. The production equipment was operated extensively during World War II, again during the Korean conflict, and recently during the Southeast Asia war. Much of this equipment and the housing structures have been operating beyond their designed capacities [1]. The Department of Defense is conducting an ammunition plant modernization program [2] that is intended to greatly enhance safety in the production plants by protective construction, automated processing, and reduction of personnel involved in hazard operations. An automated procedure was required to give structural designers the capability to perform rapid analysis of the structural safety of blast-resistant construction. The design parameters interact in a complex way since the procedure is both nonlinear and dynamic. From a design point of view an optimization procedure was required to minimize cost and

maximize safety since blast-resistant construction has been reported to cost 3 to 5 times as much as conventional construction. Therefore, the first objective was to automate the analysis procedures for determining structural response of reinforced concrete slabs having a bilinear stiffness representation and subjected to blast shock and gas pressures. Concrete slabs are the basic element forming sidewalls, roofs and floors of cells designed to confine the effects of accidental explosions. The second objective was to provide an optimum design procedure for laced (shear reinforced) and unlaced reinforced concrete slabs that will automatically produce a least-cost design for a given slab geometry, material properties, and explosive weight for both feasible and nonfeasible starting points.

Analysis Procedure

The procedure treats reinforced rectangular slabs with arbitrary boundary conditions, cross section properties, material properties and loading. The determination of the equivalent pressure load based on the quantity of explosive and cell geometry is based on Reference [3]. The computational procedure for the slab analysis utilizes reinforced concrete section properties to determine resisting moment, from which using yield line analysis techniques, the static resistance of the slab is determined. The stiffness of the slab is calculated using elastic plate theory. Using the loading, resistance, stiffness and mass of the slab, the dynamic response of the slab is computed by time step iteration. The slab is modeled as an equivalent single degree-of-freedom elasto-plastic system [4]. The design of the slab, based on its ultimate strength allows large nonlinear deformations to confine the effects of an accidental explosion. The deflections are limited in terms of support rotations.

Structural Optimization

The optimization problem consists of finding the least-cost structure that satisfies all the design constraints; or, stated in optimization terms: Find $\overset{\leftarrow}{X}$ such that $M(\overset{\leftarrow}{X})$ is a minimum and

$$g_i(\overset{\leftarrow}{X}) \leq 0 \qquad i = 1, 2, \ldots N$$

where $\overset{\leftarrow}{X}$ = vector of design variables
N = number of design constraints
g = vector of design constraints
M = objective function

Specifically for this problem the design variables selected are areas of steel reinforcement and thickness of concrete. The design constraints are minimum section properties and the flexural and shear limits. The objective function consists of the costs of formwork, concrete, and flexural and shear (lacing) reinforcement.

Fixed Variables

W = explosive weight
H = wall height
EL = wall length
h = height of explosive above floor
ℓ = distance of explosive from left side of wall
R_a = distance of explosive from wall
I = reflection code
f_{dc} = ultimate dynamic concrete strength
f_{dy} = dynamic yield strength of reinforcing steel
θ = rotation criterion

Design Parameters, X

$X =$

t_c	concrete thickness
AVT	area of vertical reinforcing steel tension
AVC	area of vertical reinforcing steel compression
AHT	area of horizontal reinforcing steel tension
AHC	area of horizontal reinforcing steel compression
AS	area lacing steel

Constraints, g (X)

$\delta(X) = \delta(\theta)$, maximum deflection

$V(X) \leq VC$ for $\theta \leq 2$ deg, maximum shear

$t_c \geq 12$, minimum thickness

$AV \geq 0.0025\ bd$, $AH \geq 0.0025\ bd$ } minimum steel reinforcement tension or compression

The methodology [5,6] selected used the unconstrained minimization approach. The problem is converted to an unconstrained minimization by constructing a function, ϕ, of the general form

$$\phi(\vec{X}, r) = M(\vec{X}) + P[g_1(\vec{X}), \ldots, g_n(\vec{X}), r]$$

For this problem the interior penalty function technique was selected. This methodology is suitable when gradients are not available, and, because the method uses the feasible region (region where all constraints are satisfied), a useable solution always results. The objective function is augmented with a penalty term that is small at points away from the constraints in the feasible region, but increases rapidly as the constraints are approached. The form is as follows:

$$\phi(X, r) = M(X) + r \sum_{j=1}^{N} \frac{1}{g_j(\vec{X})}$$

where M is to be minimized over all $\vec{X}$ satisfying $g(\vec{X}) \leq 0$, $j = 1 \ldots N$. Note that if r is positive, then, since at any interior point all of the terms in the sum are negative, the effect is to add a positive penalty to $M(\vec{X})$. As the boundary is approached, some $g(\vec{X})$ will approach zero, and the penalty will increase rapidly. The parameter, r, will be made successively smaller in order to obtain the constrained minimum of M.

Objective Function

$$\text{Cost} = M = H \cdot EL \cdot t_c \cdot C_c + (AV + AH)(EL \cdot H)C_s + (A_s)(EL \cdot H)C_L$$

where C_c = cost of concrete ($/cu ft)

C_s = cost of horizontal and vertical reinforcement ($/cu in.)

C_L = cost of lacing reinforcement ($/cu in.)

A_s = area lacing reinforcement ($/cu in.)

AV = vertical steel (tension and compression)

AH = horizontal steel (tension and compression)

$$\phi = M + r \sum_{j=1}^{N} \frac{1}{g_j(X)}$$

where r = penalty parameter.

The program requires a starting point in the feasible region before optimization can proceed. This is accomplished automatically by the program by incrementing the design variables until a feasible point is reached.

An algorithm which comprises the steps most commonly used is as follows:

1. Given a starting point, X_o, satisfying all $g_j(X) > 0$ and an initial value for r, minimize ϕ to obtain X_{min}.
2. Check for convergence of X_{min} to the optimum.
3. If the convergence criterion is not satisfied, reduce r by $r \leftarrow rc$, where $c < 1$.
4. Compute a new starting point for the minimization, initialize the minimization algorithm, and repeat from step 1.

The logic diagram for the interior penalty functions technique is shown in Figure 1.

The minimization for $\phi(X, r)$ shown in Figure 1 is accomplished by a method developed by Powell using conjugate directions [5,6].

Powell's method can be summarized as follows: Given that the function has been

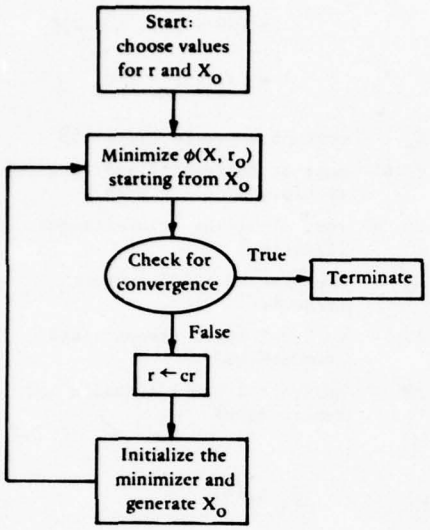

Figure 1. Logic diagram for interior penalty function technique.

minimized once in each of the coordinate directions and then in the associated pattern direction, discard one of the coordinate directions in favor of the pattern direction for inclusion in the next minimizations, since this is likely to be a better direction than the discarded coordinate direction. After the next cycle of minimizations, generate a new pattern direction, and again replace one of the coordinate directions.

Figure 2 is a logic diagram for the unconstrained minimization algorithm. The pattern move is constructed in block A, then used for a minimization step (blocks B and C), and then stored in S_n (block D) as all of the directions are up-numbered and S_1 is discarded. The directions S_n will then be used for a minimizing step just before the construction of the next pattern direction. Consequently, in the second cycle, both X and Y in block A are points that are minima along S_n, the last pattern direction. This sequence will impart special properties to $S_{n+1} = X - Y$ that are the source of the rapid convergence of the method.

Figure 2 shows a block requiring a one-dimensional minimization of α^* of the function $\phi(\overset{*}{X} + \alpha S_q)$. The one-dimensional minimization uses a four-point cubic interpolation. It finds the minimum along the direction S_q, where $\overset{*}{X}$ is the coordinate of the previous minimum. By trial and error it finds three points with the middle one less than the other two. It makes a quadratic interpolation, and then a cubic interpolation. If the actual function evaluated at the new interpolated point is not sufficiently close to that of the preceding point or if it is not sufficiently close to the interpolated function, then another cubic interpolation is made.

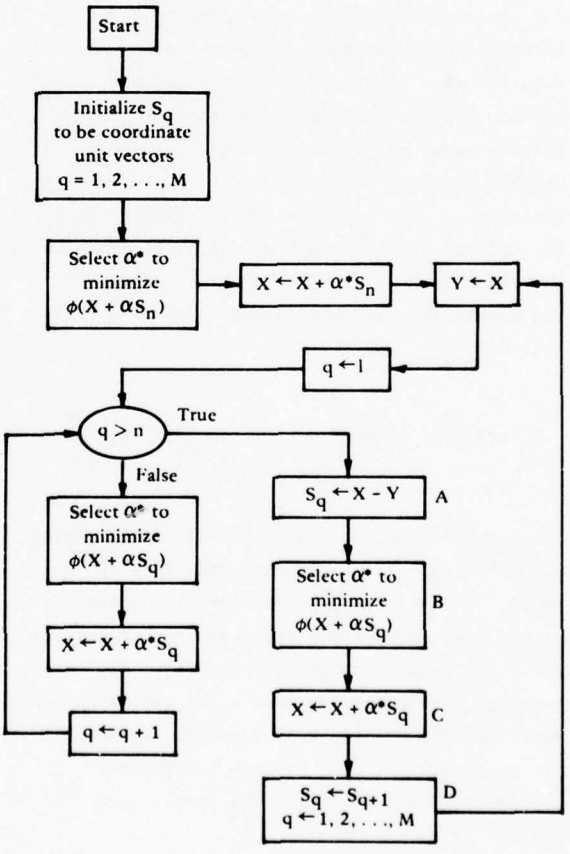

Figure 2. Logic diagram for minimization of $\phi(X)$.

Discussion of Results

The objective function is segmentally linearly dependent on the design variables; however, the constraints are both linearly and nonlinearly related to the design variables. The minimum area of steel and minimum concrete thickness are linear constraints. Figure 3 shows the constraints and objective function considering for this example that reinforcement in tension and compression is the same and that vertical reinforcement is related to horizontal reinforcement (thus reduced variables for a 2-dimensional presentation). The shear stress and deflection are nonlinearly related to the thickness of concrete. The shear stress is

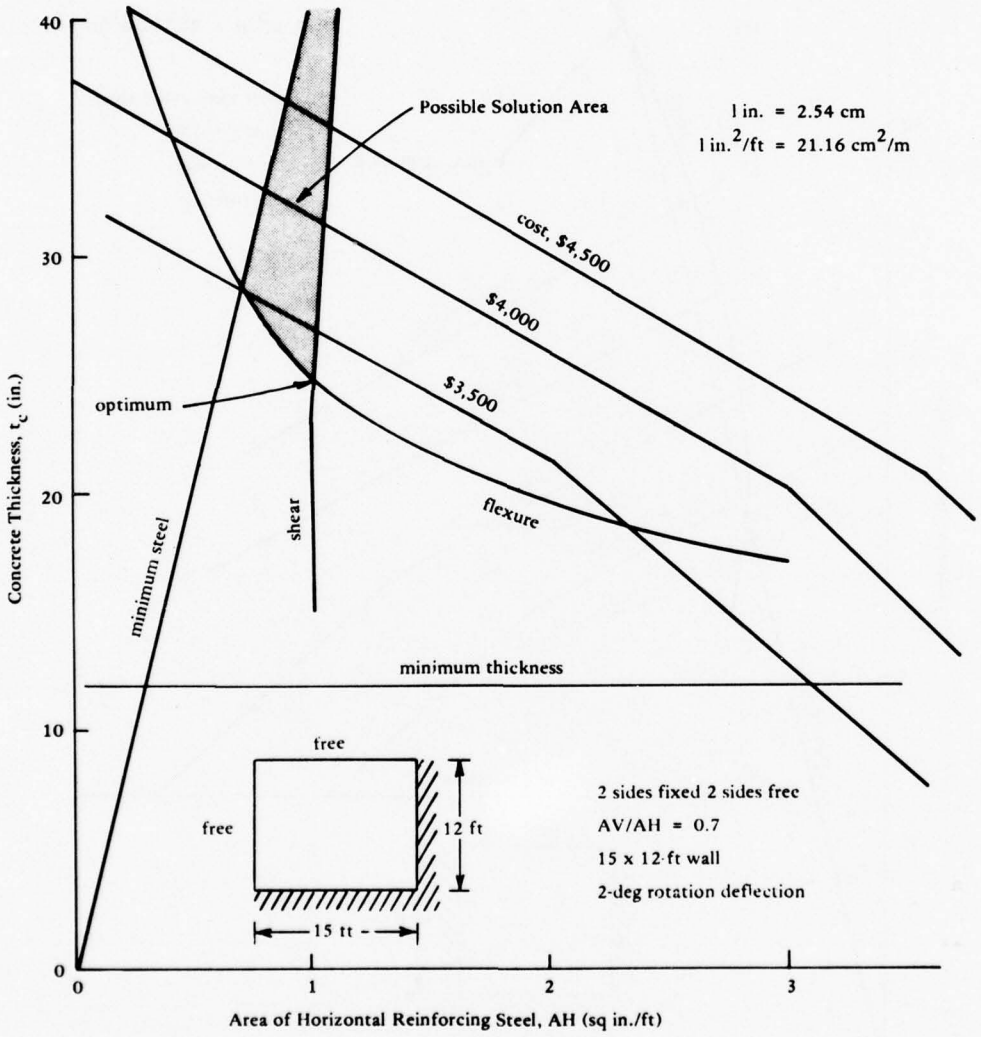

Figure 3. Design space, 2 sides fixed.

further noted not to be convex. This will be discussed later. Figure 3 shows the useable region bounded by flexure, shear, and minimum steel constraints. The optimum least-cost solution is shown. This specific example solution considers an unlaced section; thus, the maximum shear constraint is active. Laced sections eliminate the shear constraint. If the number of sides supported were increased from 2 to 3, the design space would change as shown in Figure 4. There are two regions that are useable areas. Obviously, the lower one offers the least cost and, therefore, is more desirable.

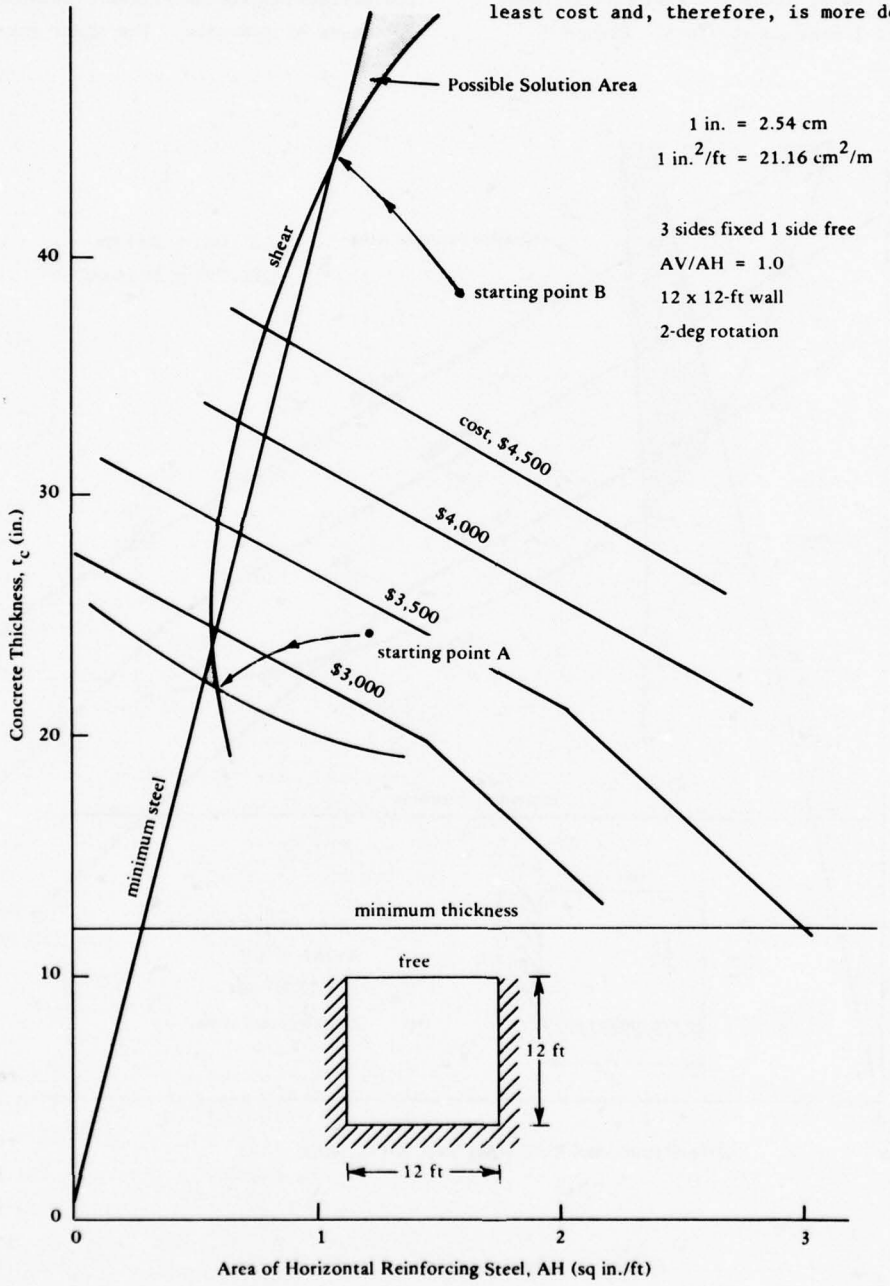

Figure 4. Design space, 3 sides fixed.

There is clearly a complex interaction of constraints showing the effect of shear. Unfortunately, the optimum solution found by the program depends on the starting point selected. The program converges on the closest relative optimum. Several alternative starting points should be used to verify a questionable optimum. Revising the design parameters could possibly shift the constraints such that only one useable solution would appear. However, a slight increase in shear stress (10%) can significantly reduce cost by allowing the near-optimum nonfeasible solution to be accepted, Figure 5.

The dual-space problem of finding a useable solution is peculiar to unlaced concrete slabs only because lacing (shear reinforcement) modifies the shear constraint. Nonautomated optimum design for unlaced conditions is almost impossible when one considers the complexity of the design space and the large number of iterations required when an initial solution is not feasible.

Cost data used in the program can be selected by the user. However, the data herein is based on work by Picatinny Arsenal on contract with Ammann and Whitney [7]. Table 1 shows a comparison of unlaced and laced concrete walls for various boundary conditions. The example considers a 15-foot-high by 12-foot-wide (4.6 m x 3.7 m) wall subjected to a 200-psi (1,400 kPa) 10-ms triangular loading function. In all cases the laced concrete (12-degree rotation) is less expensive than unlaced (2-degree rotation) designs. For the unlaced sections ultimate deflections expressed as support rotation capacity must be limited to 2 degrees whereas laced sections are allowed to reach 12 degrees by virtue of the added concrete confinement provided by the lacing.

COMPARISON OF RESULTS TO FINITE ELEMENT TECHNIQUES

To evaluate the accuracy of the approximations made in the analytical technique described above, a comparison was made to a finite element program, INSLAB [8]. Program INSLAB is a finite element program having plate element with 12 degrees freedom. An elasto-plastic material model was used throughout this work. The model was defined by the elastic modulus, yield modulus, equivalent yield stress assuming rectangular section (yield moment divided by thickness squared) and Poisson's ratio. Yielding is determined by principal moments. Uniform pressure loading is input and mass is lumped at the modes based on material density and integrating the mass over the element interpolation function. The solution procedure uses time step integration assuming a constant acceleration between successive time increments.

A reinforced concrete slab supported on three sides was analyzed for a 400 psi (2,800 kPa) pressure load with 1.17 msec duration. The slab measured 4 ft by 4 ft with 6-inch thickness (1.2 m x 1.2 m x 15 cm). Horizontal and vertical reinforcement was 0.18 sq in./ft (3.8 sq cm/m) both sides. A comparison of peak displacement from both the finite element and approximate solutions is shown in Figure 6.

The finite element analysis was performed using the computer program INSLAB, [8]. The mesh consisted of 80 elements each having 12 degrees of freedom. A time increment of 0.01 ms was used. The displacement difference at maximum value is about 13 percent.

Both techniques used an elasto-plastic analysis. The approximate solution uses a cracked moment of inertia averaged with a gross moment of inertia to determine stiffness. The finite element method uses a gross moment of inertia based on section thickness. However, the modulus of the concrete was reduced to account for reduction in stiffness resulting from cracking. The rise time of the load for the finite element solution was increased to allow a number of steps before peak load. This effect is minimal since the loading is impulsive in nature and is thought to result in about a 5 percent reduction in peak displacement.

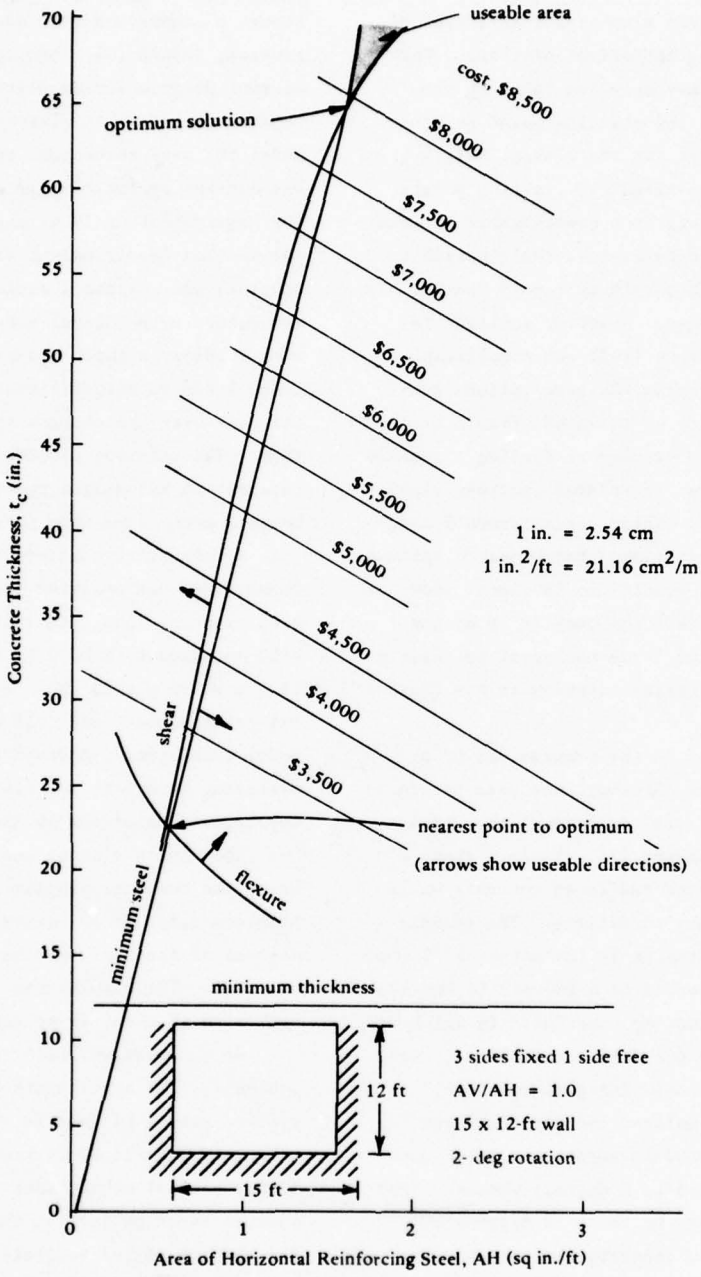

Figure 5. Revised design space, 3 sides fixed.

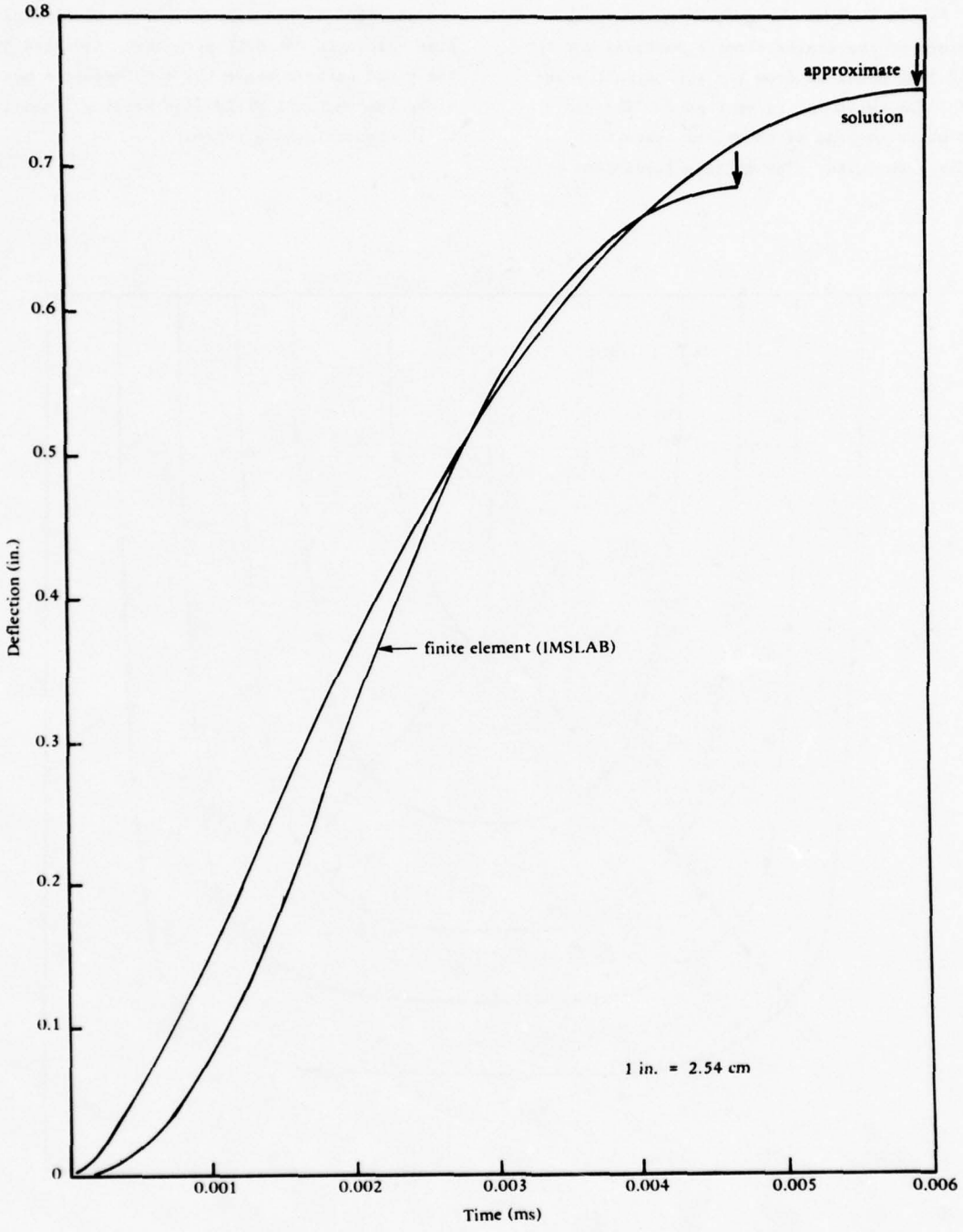

Figure 6. Displacement history 4 ft x 4 ft (1.2 m x 1.2 m) concrete slab.

Figure 7 shows the deflection contours obtained by the finite element analysis and the yield line obtained from the approximate solution. The agreement is very good. The yield line marks regions of the plate assumed to displace as units. The contour lines tend to run parallel to the support and vertical yield line. This is the same mechanism predicted by the yield pattern since the slab deflects most along the vertical yield line varying linearly to the nondeflecting support.

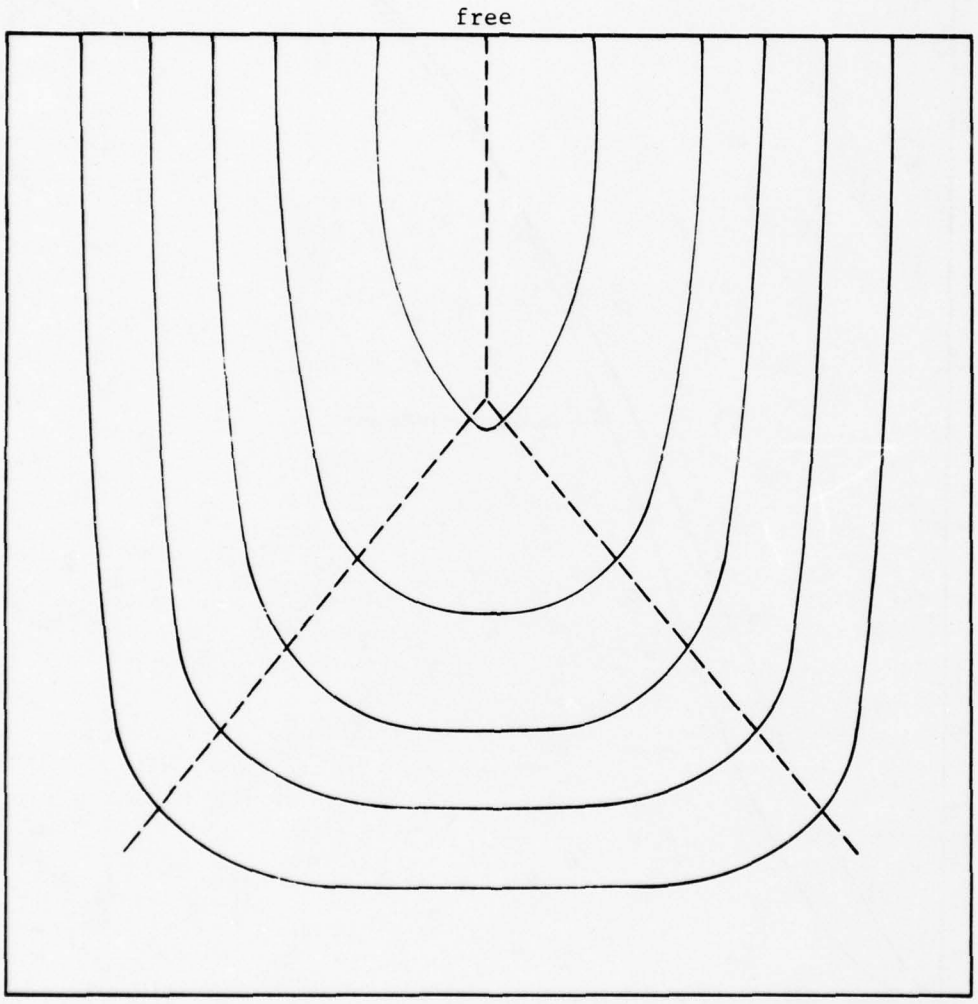

Figure 7. Deflection contour of 4 ft x 4 ft (1.2 m x 1.2 m) slab.

Table 1. Comparison of Optimum Solutions

(200 psi; 10 ms; wall, 12 ft L x 15 ft H)
(1,400 kPa; 10 ms; wall 3.7 m L x 4.6 m H)

N Side	Shear Reinforcement/ Deflection	Cost ($)
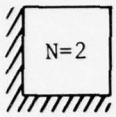	unlaced 2 degrees	3,290
	laced 12 degrees	2,289
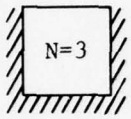	unlaced 2 degrees	2,753[a]
	laced 12 degrees	2,019
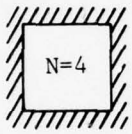	unlaced 2 degrees	2,001[a]
	laced 12 degrees	1,958

[a]Shear capacity slightly exceeded.

CONCLUSION

An optimum design procedure is given for reinforced concrete slabs using the internal penalty function approach. The solution has been found to converge rapidly and at minimum computer cost. Results agree well with more refined element analysis. This program is in use by the Navy in the design of facilities to resist dynamic pressures, such as from accidental explosions.

REFERENCES

1. J. O. Gill et al. "Preliminary report on the modernization of the Naval ordnance production base and application of hazard risk analysis technique," paper presented at the Fifteenth Explosive Safety Seminar, Department of Defense Explosive Safety Board, San Francisco, Calif., Sep 1973.

2. Arthur Mendolia. "A new approach to explosives safety," paper presented at the Fifteenth Explosive Safety Seminar, Department of Defense Explosive Safety Board, San Francisco, Calif., Sep 1973.

3. Departments of the Army, Navy, and Air Force. TM51300, NAVFAC P-397, and AFM 88-22: Structures to resist the effects of accidental explosions. Washington, D.C., Jun 1969.

4. Civil Engineering Laboratory. Technical Note TN-1434: Development of a computer program for the dynamic nonlinear response of reinforced concrete slabs under blast loading, by J. M. Ferritto. Port Hueneme, Calif., Apr 1976.

5. R. L. Fox. Optimization methods for engineering design. Addison Wesley, Reading, Mass., 1971.

6. Advisory Group for Aerospace Research and Development. AGAARD No. 149: Structural design applications of mathematical programming techniques. NATO.

7. Picatinny Arsenal. TR-4441: Preliminary estimate of concrete thickness and construction costs of laced reinforced concrete structures, by R. Dede, R. Dobbs, N. Porcaro, and J. Rindner. Dover, N.J., Oct 1972.

8. Users Guide for INSLAB Code, Agbabian Associates, El Segundo, Calif., Sep 1975.

A NUMERICAL COMPARISON WITH AN EXACT SOLUTION FOR THE TRANSIENT RESPONSE OF A CYLINDER IMMERSED IN A FLUID

M. E. Giltrud, D. S. Lucas
Naval Surface Weapons Center
White Oak, Silver Spring, Maryland 20910

The transient response of an elastic cylindrical shell immersed in an acoustic media that is engulfed by a plane wave is determined numerically. The method applies to the USA-STAGS code which utilizes the finite element method for the structural analysis and the Doubly Asymptotic Approximation (DAA) for the fluid-structure interaction. The calculations are compared to an exact analysis for two separate loading cases: a plane step wave and an exponentially decaying plane wave. The results of the comparisons are most favorable which supports the applicability of USA-STAGS for fluid-structure interaction problems.

INTRODUCTION

Fluid structure interaction problems have recently become quite important to the Navy. Fundamental knowledge of the fluid-structure interaction problem is a basis for a more thorough understanding of damage to submerged structures from underwater shock loading. The difficulty in developing analytical models to predict the response of submerged structures to underwater explosions is twofold. First, the structure must be suitably modeled in order to determine its elastic-plastic response. This certainly is within the capability of many structural analysis computer codes. Secondly, the loading effects are altered according to the state of motion of the structure in the fluid. Thus, the problem in determining the loading is one in which the state of motion of the fluid and structure are coupled.

Analytical solutions have been obtained for simple elastic structural geometries with simple temporal and spatial waveforms. However, in some cases the results have to be generated numerically since the resulting solution is quite complex. In addition, analytical solutions seldom address the problem of internal structure in any detail. Analytical investigations have resulted in the adoption of methods for uncoupling the structure from the fluid.

These procedures, known as surface approximation techniques, have been compared by Geers [1]. It is apparent from his analysis that the Doubly Asymptotic Approximation (DAA) [1-3] is the most accurate for early and late times in predicting the behavior of submerged shells. The DAA also affords a smooth transition between early and late time response. More recently, the DAA has been used in conjunction with several linear elastic finite element computer codes to predict the response of submerged targets to underwater shock loading [4, 5].

Since the close-in underwater detonation of high explosives causes large local plastic deformation, a structural analysis computer code capable of performing such analyses for general shell structures is required. The STAGS [6, 7] (Structural Analysis of General Shells) code has been selected since it is highly efficient in performing such analyses.

The STAGS code has been combined with a DAA code, USA (Underwater Shock

Analysis), with the resulting code called USA-STAGS. In the following sections we discuss the application of USA-STAGS to the problem concerning the response of a linear elastic cylindrical shell immersed in a fluid that is engulfed by a plane acoustic wave. The results of the USA-STAGS calculations are compared to an exact analysis by Huang [8].

EXACT ANALYSIS METHODOLOGY

Huang's analysis focuses upon the problem of the transient interaction of a plane acoustic wave with a circular cylindrical shell immersed in a fluid. For the circular cylindrical shell, Huang states that "this paper presents an exact formulation by simple transformations of the basic differential equations governing the coefficients of the series solution for the shell deflections and the wave pressure for each "mode" into a Volterra integral equation of the second kind." The integral equations are then solved by a step-by-step integration scheme. This method is also very efficient for parametric studies, and the entire computation process is quite straight forward, and can easily be controlled to have a high degree of accuracy.

Exact series solutions are presented in this work for the cases of a neutrally bouyant shell submerged in water subjected to step and exponentially decaying incident waves. The complete pictures of the total motion and stress responses of the shell are revealed. The material properties used were those of steel for the shell and water for the fluid. The case which has been chosen to model on USA-STAGS is that for a thickness to radius ratio of 1/31, which corresponds to the dimensionless parameter M = 2. [8]

In the derivation of the shell equations, the relative changes in length and shear of the shell middle surface and the change of curvature and twist have been accounted for as in Junger [9]. Thus, the shell equations used are quite general and are exact for the elastic behavior of the shell within the Kirchoff assumption of shell theory [10]. The geometry of the problem for the circular cylindrical shell and the non-dimensionalized velocity responses are shown in Figures 1 and 2.

USA-STAGS ANALYSIS PROCEDURE

The USA-STAGS code makes use of the finite element method for the structure and the DAA for the fluid-structure interaction. The coupled system of equations are

$$\underset{\sim}{M}\,\ddot{\underline{x}} + \underset{\sim}{K}\,\underline{x} = -\,\underset{\sim}{T}\,\underset{\sim}{A}\,(\underline{P}_S + \underline{P}_I) \qquad (1)$$

$$\underset{\sim}{A}\,\dot{\underline{P}}_S + \rho\, c\, \underset{\sim}{A}\,\underset{\sim}{M}_F^{-1}\,\underset{\sim}{A}\,\underline{P}_S = \rho\, c\, \underset{\sim}{A}\,(\underset{\sim}{T}^T\,\ddot{\underline{x}} - \ddot{\underline{x}}_I) \qquad (2)$$

Variables appearing here are defined as:

- $\underset{\sim}{M}$ — Structural mass matrix
- $\underset{\sim}{K}$ — Linear or nonlinear structural stiffness operator
- $\underline{x}$ — Structural displacement vector
- $\ddot{\underline{x}}$ — Acceleration vector
- $\underset{\sim}{T}$ — A transformation matrix (rectangular) which relates displacement variables in fluid to those in structure
- $\underset{\sim}{A}$ — Fluid element area matrix (diagonal)
- $\underline{P}_S$ — Vector representing scattered fluid pressure
- $\underline{P}_I$ — Vector representing incident fluid pressure
- $\underset{\sim}{M}_F$ — Fluid mass matrix
- ρ — Fluid density
- c — Speed of sound in fluid
- $\ddot{\underline{x}}_I$ — Vector of fluid particle acceleration due to the incident wave

Step by step integration of these equations carried out with a staggered solution procedure described below:

(1) estimate $\ddot{\underline{x}}$ at next step by extrapolation of previous value

(2) solve (2) for $\underline{P}_S$

(3) solve (1) for $\underline{x}$

This solution procedure is conditionally stable. Therefore, the fluid equation (2) has been altered to achieve unconditional stability [11].

In order to predict the transient response of a cylindrical shell immersed in a fluid excited by an acoustic wave, a finite element model of the cylinder has been constructed. Since the plane strain response of the cylinder is desired, a finite element model of arbitrary length could be used. In fact, a finite element model consisting of one element along the length is adequate. However, in order to model the added mass effects (described by $\underset{\sim}{M}_F$ in equation (2)) a longer model is required. The actual model used for the analyses has a length to diameter ratio of 10.

RESULTS AND DISCUSSION

Two analyses have been performed with USA-STAGS and the results have been compared to the exact analyses by Huang. The first analyses concerns a step pressure wave that is shown in Figure 3a and the second concerns an exponentially decaying pressure wave that is shown in Figure 3b. The standoff distance from front of the cylindrical shell to the point source of 100 diameters is used. This effectively reduced the sphericity of the wave to nearly a plane wave.

The integration procedure used for the staggered solution is the Park's linear multi-step method [12]. Since the integration procedure for the coupled equations is unconditionally stable, a time step is chosen to achieve accuracy in the solution. A time step of about 1/50 of a transit time has been used for all analyses. (The transit time is the time required for the acoustic wave to traverse the shell. In this case it is 1.67×10^{-4} sec.)

The result of the USA-STAGS calculations are compared to the exact analyses in Figures 4 and 5. Figure 4 gives the velocity response of the shell at the horizontal centerline for the step wave loading. The calculations compare very well with the exact analyses for the 1.75 transit time shown. The USA-STAGS results show good agreement for both frequency and amplitude.

The velocity response comparisons for the exponential wave are shown in Figure 5. USA-STAGS results tend to oscillate more than the exact analysis. This can be accounted for by the observation that the exact solution contain contributions from the first seven modes. The USA-STAGS calculations contain contributions from higher modes. These higher modes are excited by the rapidly decaying incident pressure wave (the duration of the loading is 0.06 transit time).

SUMMARY

A comparison of an exact solution for the velocity response of a cylindrical shell immersed in a fluid with that of a solution generated by a fluid analyzer and structural code (USA-STAGS), for plane shock wave loading has been presented. Good agreement has been obtained between the two results for step and exponential pressure wave loading. These comparisons are supported by previous investigations.

REFERENCES

1. Geers, T. L., "Transient Response Analysis of Submerged Structures," in Finite Element Analysis of Transient Non-linear Behavior, AMD Vol. 14, ASME, New York, 1975

2. Geers, T. L., "Response of an Elastic Cylindrical Shell to a Transverse Acoustic Shock Wave in a Light Fluid Medium," J. Acoust. Soc. Am., Vol. 48, No. 3, Sep 1970, pp 692-701

3. Geers, T. L., "Excitation of an Elastic Cylindrical Shell by a Transient Acoustic Wave," J. Appl. Mech., Vol. 36, No. 3, Sep 1969, pp 459-469

4. DeRuntz, J. A., Geers, T. L., Felippa, C. A., "The Underwater Shock Analysis (USA) Code, A Reference Manual," LMSC-D624328, Contract No. DNA 001-76-C-0285, Feb 28, 1978

5. Everstine, G. C., Wang, Yung-Fa, "The Response of a Cylindrical Hull with Internal Structure (Configuration 1) to Underwater Nuclear Shock Waves," Report No. 77-0037, DTNSRDC, April 1977

6. Almroth, B. O., Brogan, F. A., "The STAGS Computer Code," Report No. LMSC-DS58853, Structural Mechanics Laboratory, Lockheed Palo Alto Research Lab, Palo Alto, California

7. Almroth, B. O., Brogan, F. A., Stanley, G. M., "Structural Analysis of General Shells," Volume II, User Instructions for STAGS, Structural Mechanics Laboratory, Lockheed Palo Alto Research Lab, Palo Alto, California, March 1978

8. Huang, H., "An Exact Analysis of the Transient Interaction of Acoustic Plane Waves with a Cylindrical Elastic Shell," J. Appl. Mech., Vol. 37, No. 4, Dec 1970, pp 1091-1106

9. Junger, M. C., "Vibrations of Elastic Shells in a Fluid Medium and the Associated Radiation of Sound," J. Appl. Mech., Vol. 19, Trans. ASME, Vol. 74, 1952, pp 435-439

10. Novozhilov, V. V., Thin Shell Theory, translated by Lowe, P. G., and edited by Radok, J. R. M., P. Noerdhoff Ltd., Groniger, The Netherlands, 2nd revised edition, Chapter 1, 1964

11. Park, K. C., Felippa, C. A., DeRuntz, J. A., "Stabilization of Staggered Solution Procedures for Fluid-Structure Interaction Analysis," pp 95-124 of Computational Methods for Fluid Structure Interaction Problems, AMD Vol. 26, ASME, New York, 1977

12. Park, K. C., "An Improved Stiffly Stable Method for Direct Integration of Non-linear Structural Dynamics," J. Appl. Mech., Vol. 42, 1975, pp 464-470

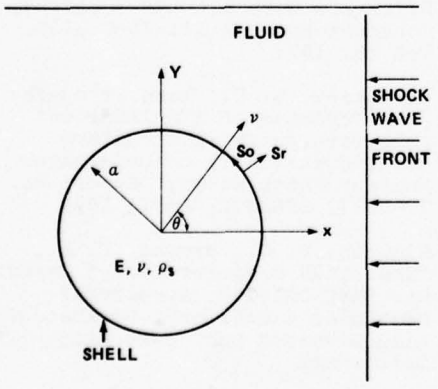

FIGURE 1 GEOMETRY OF PROBLEM

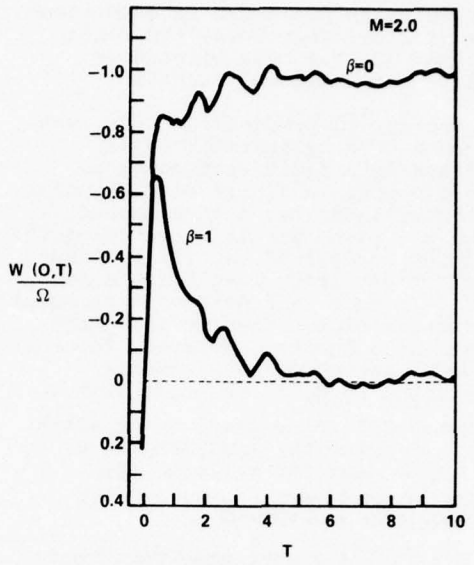

FIGURE 2 HUANG'S DIMENSIONLESS RESULTS FOR h/a=1/31

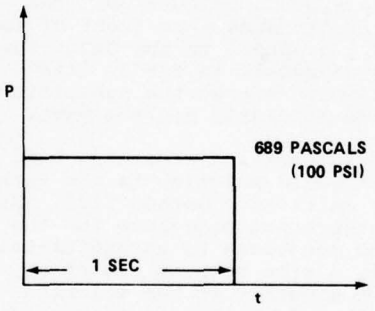

FIGURE 3a STEP WAVE PRESSURE

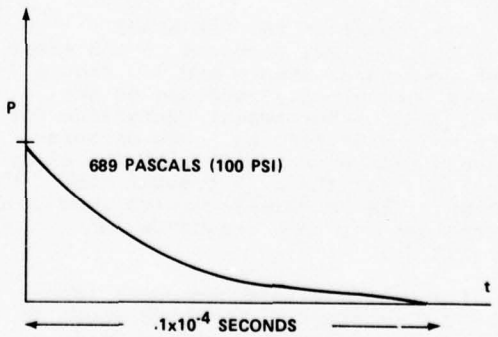

FIGURE 3b EXPONENTIAL WAVE PRESSURE

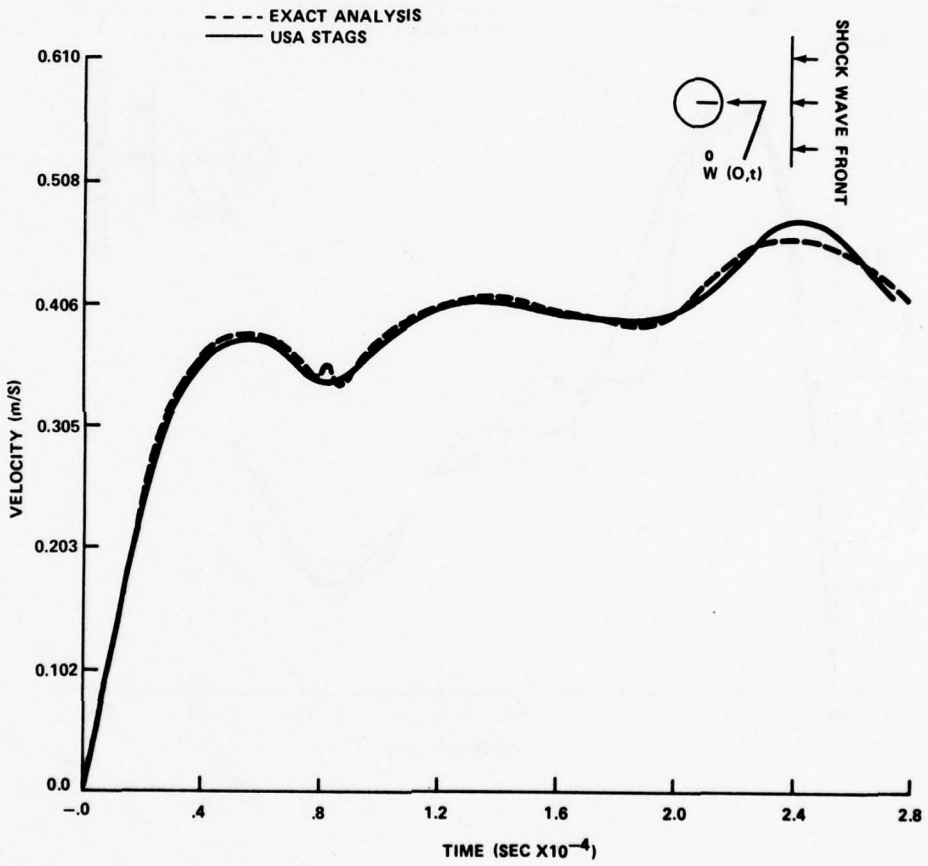

FIGURE 4 VELOCITY COMPARISONS FOR STEP WAVE $\overset{o}{W}$ (O,t)

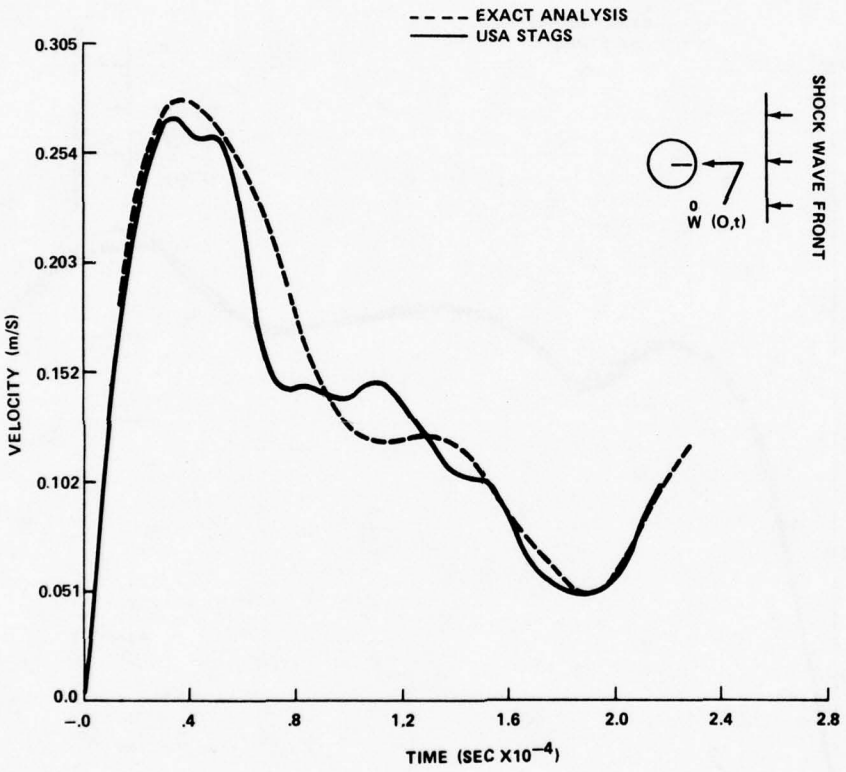

FIGURE 5 VELOCITY COMPARISONS FOR EXPONENTIAL WAVE $\overset{0}{W}$ (O,t)

CASE STUDIES IN DYNAMICS

FOIL SYSTEM FATIGUE LOAD ENVIRONMENTS FOR COMMERCIAL HYDROFOIL OPERATION

D. L. Graves
Boeing Marine Systems
Renton, Washington

Complexity and severity of the hydrofoil fatigue loads environment in the open sea is without parallel in terms of flight vehicle environments. The random nature of wave orbital velocities, periods and heights plus boat heading, speed and control system design must all be considered to assess the structural fatigue requirements. Major nonlinear load events such as hull slamming and foil unwetting are key contributors to the fatigue environment. Full scale "rough water" load tests, field experience plus analytical loads work on the Model 929 JETFOIL commercial hydrofoil provided a major increase in knowledge of the hydrofoil loads environment. The problem of developing an overall sea environment for design is discussed. Structural fatigue damage is shown to be dominated by the most severe and infrequent load environments which are also the most difficult to define statistically. State of the art analytical approaches were found to be limited in providing satisfactory predictions of the complex fatigue load environments.

Nomenclature

Symbol	Definition
$E(x)$	Exceedance frequency for load level X
f_w	Average wave encounter frequency measured from moving craft
H_{sig}	Significant wave height, equal to the average of 1/3 highest waves
L_F	Total dynamic lift load on front foil semispan
$L_{F_{s.s}}$	Nominal steady state lift on front foil semispan
L_{F_m}	Maximum expected lift on front foil semispan
L_{F_Δ}	Incremental load factor, $(L_F - L_{F_{s.s.}})/L_{F_m}$
L_{AA}	Total dynamic antisymmetric lift load on aft foil
L_{AS}	Total dynamic Symmetric lift load on aft foil
L_A	Nominal steady state lift on aft foil
L_{A_m}	Maximum expected lift on aft foil
L_{AA_Δ}	Incremental antisymmetric foil load factor, $(L_{AA} - L_{A_{s.s.}})/L_{A_m}$
L_{AS_Δ}	Incremental symmetric foil load factor, $(L_{AS} - L_{A_{s.s.}})/L_{A_m}$
N	Fatigue life, cycles
$P(X_i>X)$	Probability that peak value X_i exceeds X
T_{sig}	Average stationary wave period of 1/3 highest waves, seconds
V_w	Orbital wave velocity
σ	Standard deviation
ω	Circular frequency, rad/sec

I. Introduction

The general problem of developing design criteria for a random loading environment is a familiar one. However, in the specific case of a hydrofoil operating in the open sea, the problem has received minimal theoretical development. In terms of practical design experience, the state of the art of hydrofoil fatigue environments has been nonexistent. Even though displacement hull ships have been a common form of transportation for centuries, it is only within the last several years that the problem of determining displacement hull statistical behavior in a random sea has received serious attention in the technical literature. For the hydrofoil craft, the need for accurately assessing fatigue load environments is more urgent. Weight and performance are both critical and the loading environments more severe than for displacement hulls. For these design considerations the hydrofoil is closer to a fighter airplane than a displacement hull ship.

It is accurate to categorize the fatigue load environments of a modern sea going hydrofoil craft with submerged foils as being more severe and complex than that of most, if not all, other flight vehicles. At foilborne speeds the sea imposes a continuous spectrum of random gusts on the foils and struts. If an active control system which operates flap surfaces is used, it is continuously interacting with the environment to control and stabilize hull motions. The wetted area on the struts is in a state of dynamic transition. Cavitation is an important hydrodynamic phenomena which affects the load behavior. In large seas, major nonlinear load events occur when the foils approach or break the water surface or the hull slams into a wave. Not only the magnitude but the frequency of these load events must be predicted to provide adequate load criteria for the structural design.

The Model 929-100 JETFOIL is currently the only commercial hydrofoil in operation which employs submerged foils and operates on a daily basis in open seas at various locations throughout the world. Operational experience to date has included routes in Hong Kong, the Pacific Ocean off Hawaii, Caribbean waters off Venezuela, the Sea of Japan and the English Channel. Full scale "rough water" load tests, commercial field experience and analytical simulation studies of the JETFOIL have provided a major increase in understanding and appreciation of the hydrofoil fatigue load environment.

II. Vehicle Configuration and Design

Figure 1 illustrates the basic JETFOIL hydrofoil craft. The hull is of aluminum construction to achieve low weight while the foils and struts are made of a high strength steel alloy. The JETFOIL has an upside down "T-Tail" for the front foil system. The aft foil system consists of port and starboard foil segments joined together by a large center strut and "capped" on each end by an outboard strut. Propulsion is accomplished by two waterjet pumps which receive water from a duct inlet on the aft center strut. Cruise speed while foilborne is over 40 knots. An automatic control system essentially flies the JETFOIL. Activation of full span flaps on the foils is accomplished by the control logic to stabilize hull motions and maintain a nominal foil depth (6.5 feet). Onboard accelerometers and gyros provide hull motion inputs to the control logic. A sonic height sensor on the bow is used to sense the water surface and thus provide a means of controlling the depth of the submerged foils. A steerable front strut is used for turn coordination and also reacts to lateral acceleration feedback commands. Roll stability is maintained by differential flap deflections on the aft foil.

Two control modes are used: a platform mode and a contour mode. In the platform mode the control system has strong acceleration feedback gains and attempts to nullify boat accelerations and pitch angle, irrespective of the seas. In the contour mode the feedback gains are much lower and the boat has a greater tendency to contour the wave profiles. Load environments are fundamentally affected by the control system mode.

III. Full Scale Testing Conditions and Instrumentation

The major portion of the hydrofoil load behavior was obtained from strain gage instrumentation placed on the foil structure during "rough water" testing of a production JETFOIL craft. Analytical tools were available for examining the statistical load behavior but could not be used to confidently establish design criteria. The complexity of the environment and the absence of sufficient data to verify the simplified analytical representations necessitated a strong test oriented approach. Limited data available prior to the full scale test program indicated that the analytical estimates of foil loads seriously underestimated the actual environments.

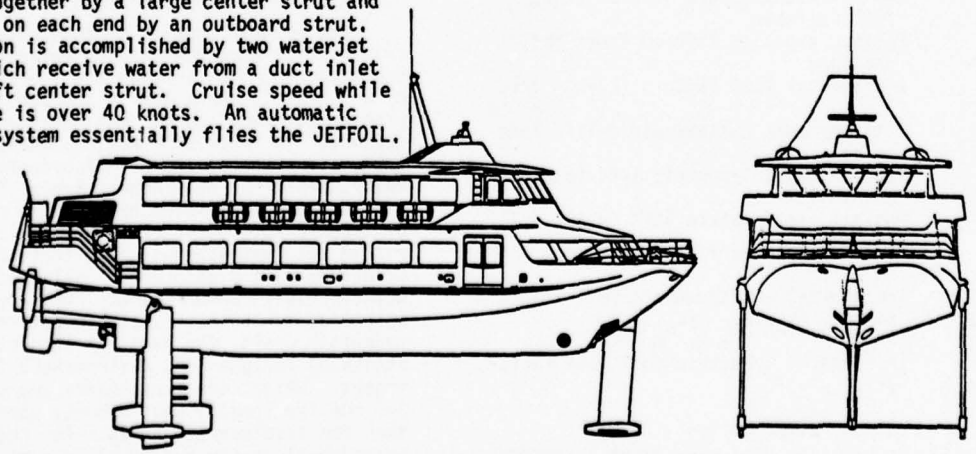

FIGURE 1 MODEL 929-100 JETFOIL CONFIGURATION

Figure 2 illustrates the basic strain gage instrumentation used in the full scale testing. Arter installation a comprehensive static loading program was conducted to load calibrate the gages. With the appropriate combination of strain gages at a particular foil section, shear, bending moment and torsion loads could be determined. A multiplicity of gage locations allowed determination of distributed loads.

Many of the gages, particularly those on the foil surface, were exposed to high speed water flow when the boat was foilborne. This severe environment necessitated careful consideration of the strain gage installation technique to insure a good test life. Figure 3 illustrates the gage installation used on the foil surfaces. The strain gage was a weldable gage with an integral waterproof stainless steel jacketed lead which was secured with retention straps. A flexible, strong epoxy was faired over the gage and lead. After curing it was sanded to provide a smooth contour with the steel surface of the foil.

Foilborne testing in rough water was accomplished in the Pacific Ocean and the Straits of Juan de Fuce near Neah Bay, Washington. Total testing activity was of several days duration performed at three separate calendar periods and encountered a diverse range of sea conditions. Operation in sea state five with significant wave heights up to 12 feet was accomplished. Data in all sea headings (head, bow, beam, quarter and follow) was obtained.

A fundamental part of the data analysis was not only to define basic loads behavior but to associate the load information to specific sea environments. To accomplish this, the sea environment was measured by an onboard wave height instrument. This instrument gave a reading of inertial wave profile versus time by subtracting measured boat motion from the sonic height sensor measurement taken at the bow of the JETFOIL. The wave profile was then statistically analyzed to determine the generic parameters generally used for sea state characterization (e.g., H_{sig} and T_{sig}).

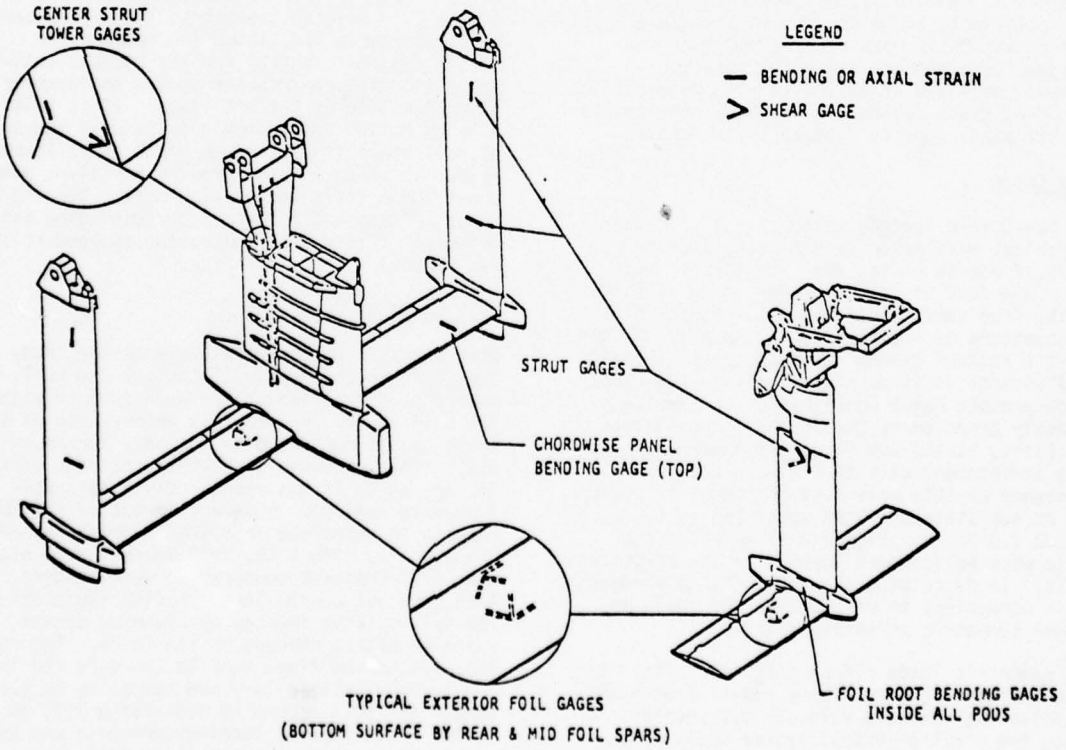

FIGURE 2 FOIL SYSTEM STRAIN GAGE LOCATIONS FOR ROUGH WATER LOADS TESTING

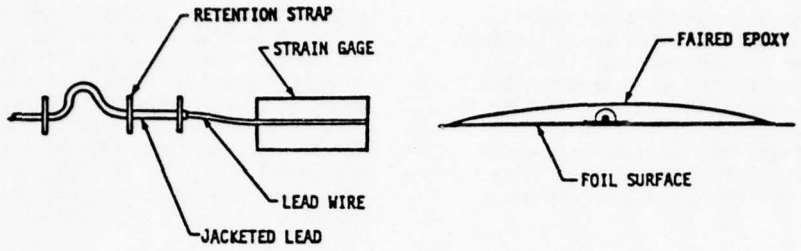

FIGURE 3 EXTERIOR FOIL STRAIN GAGE INSTALLATION

IV. Load mechanisms

Because a hydrofoil ship consists of a normal displacement hull plus a foil system which functions very similar to an airplane wing, the variety of loading possibilities becomes quite numerous. The foil systems individually experience many types of loading. However, when foilborne in very large seas, load interactions can also occur which involve both the hull and foil systems. The primary foil load environments can be categorized into three basic load mechanisms: wave loads, hull slamming loads, and foil unwetting loads. These phenomena produce the basic beam bending and torsion fatigue loads which dictate the structural design. Detailed attention is also required for local pressure loading which is required to analyze panel bending fatigue environments.

Wave Loads

The basic wave loading phenomena is produced by orbital wave velocities causing a change in angle of attack on the foil and struts. Because the foil is not submerged at an infinite depth, free surface effects also result in load fluctuations as the foil depth changes. As the craft's control system attempts to stabilize hull motions it is constantly moving the flaps which produce major modification of the loads directly produced by the waves. In essence, the foils, struts and flaps are experiencing a gust environment each time a wave passes. Frequency of this wave load phenomena is dependent on sea state and boat speed but is typically around 1.0 Hertz. Figure 4 illustrates the basic wave environment imposed on the struts and foils. In describing the wave loading phenomena it is convenient to distinguish the loads as either symmetric or antisymmetric.

The symmetric loads affect only the foils. As illustrated in Figure 4 they result from head or following sea wave velocity components. Since the craft's control system operates on acceleration feedback, the flaps deflect in an attempt to null symmetric lift forces. The flaps are continuously operating as gust alleviators. In the process, however, torsion loads are increased because of the difference in center of pressure locations between flap lift and angle of attack lift. Likewise, a severe environment is imposed on the flap mechanisms.

Antisymmetric wave loads primarily result from beam sea orbital velocity components. The beam sea components cause side loads on the struts which in turn result in antisymmetric lift on the foils. Some antisymmetric lift is caused by hydrodynamic flow induction between the struts and foils but by far the biggest antisymmetric lift contributor is the antisymmetric aileron action of the aft flaps. It is this aileron action which provides the only source of roll stability while the craft is foilborne. As the strut side loads produce a rolling moment about the craft's center of gravity, the aft flaps deflect and produce a corresponding antisymmetric lift which negates the induced rolling moment.

Hull Slamming Loads

When the seas become relatively severe, many of the waves encountered will contact the hull. A moderate interaction of the wave surface with the hull of the hydrofoil is referred to as a crest and is dominated by buoyancy forces on the hull. This produces a moderate increase of foil loading which is not readily distinguishable from wave loading. A severe impact of the hull results in hydrodynamic slamming pressures which dramatically affect the foil loads. Hull slamming is infrequent compared to wave loading frequency but causes large loading fluctuations. The hull motions induced by slamming create angle of attack changes on the foils. The control system and flaps tend to increase the loading changes because they are operating to counteract the hull forces by decreasing lift on the foils. This type of loading mechanism can be particularly severe on the front foil where large negative flap angles are concurrent with negative angle-of-attacks. Figure 5 illustrates

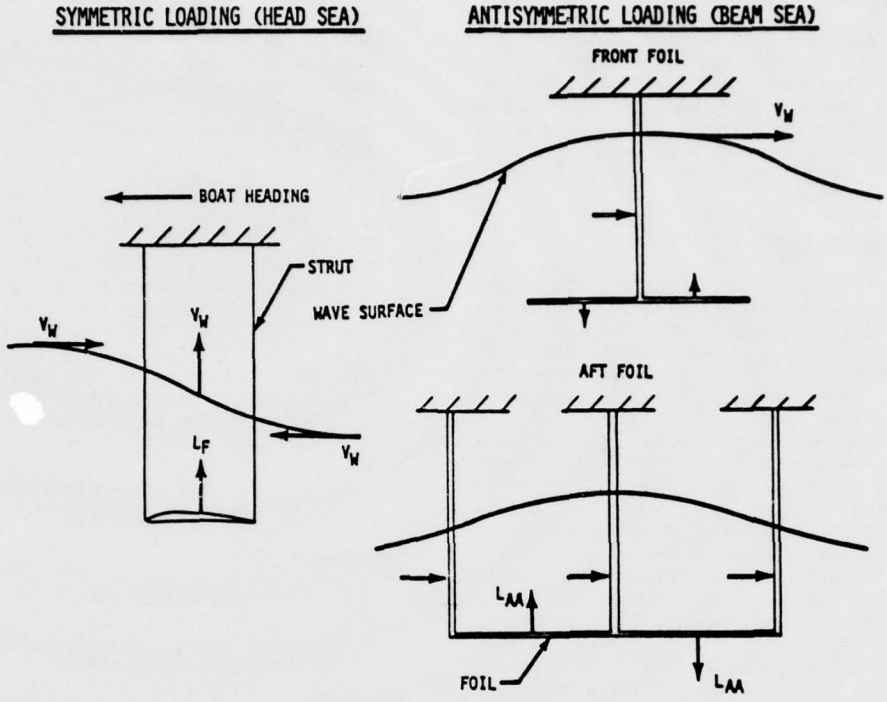

FIGURE 4 FOIL SYSTEM WAVE FORCES

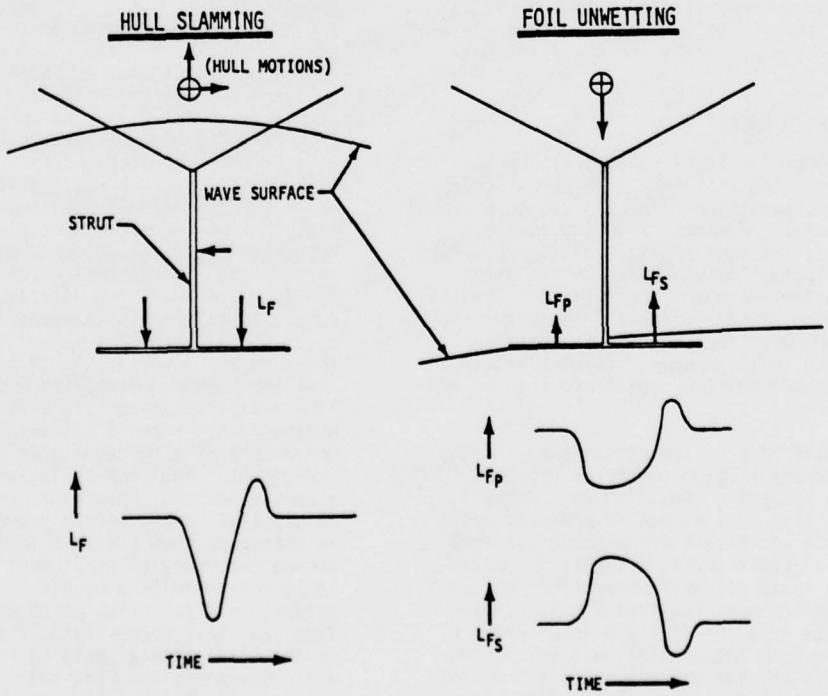

FIGURE 5 FOIL HULL SLAMMING AND UNWETTING FORCE

foil loads which typically result from a hull slam event. Strut side loads can also be significant during a slam because of lateral hull motion. The typical load cycle illustrated involves a large negative lift fluctuation and a following positive incremental lift which normally occurs after the hull slam as the craft stabilizes itself. Full load reversal of the front foil was observed from many hull slams during sea trials.

Foil Unwetting Loads

When the foil comes sufficiently close to the water surface, a ventilation or unwetting of the top foil surface will occur because the low flow pressures on the upper surface cannot be sustained in the vicinity of atmospheric pressure. This event, as for hull slamming, occurs in larger seas and although infrequent, causes large load fluctuations. Because conditions are never completely symmetric, unwetting generally occurs on one semispan of the foil as illustrated in Figure 5. The semispan which unwets loses lift and the other semispan will subsequently experience an increase in lift because the flaps are deflected down to offset the initial lift loss and downward hull motion. This unsymmetric lift results in large bending moments on the strut. For the JETFOIL this loading event was more critical to the strut than to the foil. In the extreme event where the foil completely breaks the water surface the lift of both semispans obviously goes to zero. This is called a broach. Although possible, it is very difficult to achieve unwetting of the aft foil. Foil unwetting is a fatigue concern primarily for the front foil and strut.

Local Pressure Loads

Although so called local panel pressure loading primarily results from the basic wave loading mechanism, separate consideration of this problem is needed. Factors affecting local pressure include wave orbital velocities, flap motions, fluctuating waterline on the struts, and cavitation. Another consideration for the water duct inlet pressure was inlet unwetting which occurs when the water duct breaks the wave surface in large seas. Inlet unwetting is not frequent but large pressure changes are involved.

Near the waterline on the struts wave surface movement causes a large number of pressure load cycles due to cyclic unwetting and rewetting of the flow. This is a symmetric pressure cycle on the strut and causes no net beam loading. Magnitude of these pressure cycles is up to 15 psi and is of primary concern for the panels at midchord and near the trailing edge. Induction effects from the foil and local angle of attack from beam sea orbital wave velocities become important for areas located a few feet below the waterline. These later effects result in antisymmetric pressure loading of the strut and primarily affect the panels near the leading edge. The centerline strut panels are subject to internal pressure changes of the water duct as well as the above external pressure environments.

Another local phenomena is cavitation which results when the water pressure drops below the vapor pressure causing an air cavity. This phenomena is most prevalent on the upper foil and flap surface. During rough water operation the wave and flap dynamics result in rapid changes of pressure which result in "make and break" cavitation areas on the upper foil surface. Test data showed the local panel cavitation loading behaved in a quasi-steady state manner being limited to a certain value when cavitation occurred over the panel. The cavitation environment over major surface areas and flaps was also important to overall loading distributions.

V. Development of Fatigue Load Design Spectrums

Data Analysis

Due to the wide variety of sea conditions and total time duration of the full scale testing activity, it was possible to build a good statistical data base relating foil loads to specific environment conditions. The problem was reducing the large number of loading cycles (on the order of 10,000 for each parameter) obtained from testing down to some manageable parametric description. Figure 6 illustrates the basic procedure used to statistically analyze the data. Data samples typically of three to five minutes duration were digitally analyzed to give the following parameters: mean, standard deviation, average of 1/3 (X 1/3) and 1/10 (X 1/10) highest peaks. Detailed information on the distribution of the entire population of load cycle events could also be obtained in the form of cumulative probability distributions or exceedance plots. The desired objective was to establish a simple parametric statistical distribution which would satisfactorily approximate the distribution of the test data. If this could be done, then the only statistical parameters needed to provide a complete characterization of the load behavior were the standard deviation and the average load cycle frequency. This objective was generally met for all sea conditions where the occurrence of major nonlinear load events was infrequent. The load cycles arising from hull slamming and foil unwetting were much larger in magnitude and distinctly more nonsymmetric in character than the wave loads. Thus, it became necessary to hand count and tabulate the large nonlinear load events individually. A parametric description of these loads was not feasible, thus necessitating the development of empirical tabular data to characterize their frequency and magnitude. Fortunately, the wave loads could usually be characterized by the familiar Rayleigh distribution

$$P(X_1>X)=e^{-1/2(X/\sigma)^2} \quad (1)$$

known to be valid for the distribution of peaks of a random variable from a linear, narrow-banded, Gausian process. In those cases where a Rayleigh assumption was not satisfactory, using a parametric combination of the Rayleigh and exponential distribution

$$P(X_1>X)=e^{-X/\sigma} \quad (2)$$

proved to be useful.

Sea state characterization was obtained by calculating Hsig and Tsig from the wave height instrument data. Calculation of Hsig from the wave height instrument was a straight-forward process, however, determining Tsig was more involved because Tsig is a stationary parameter. Since the JETFOIL provided a nonstationary platform for the wave height sensor, some transformation of the data was required to estimate the generic Tsig description of the wave's periodicity. The wave height sensor data was analyzed to define f_w for the moving craft system. This could be related to Tsig by using standard statistical relationships developed from theoretical wave spectrums (1). Because of the nonstationary measurement condition, a precise mathematical relationship between f_w and Tsig was not possible.

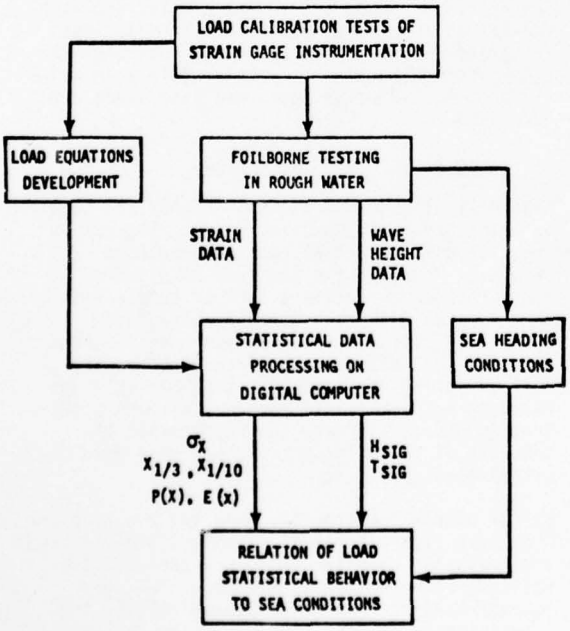

FIGURE 6 LOADS TEST DATA STATISTICAL ANALYSIS

The technique of spectral moments (2) is precise only for stationary conditions. For nonstationary conditions a numerical approach was required to correctly translate the wave spectrum equation into a moving system and provide an accurate correlation between Tsig and f_w.

Reduced statistical load parameters were then cross plotted against Tsig and Hsig. Loads for sea conditions not specifically encountered in testing were defined by utilizing the apparent data trends and incorporating trend data from analytical simulations. Thus, a data base was formulated which could define load spectrums for any design environment.

Design Environment

Selecting a specific design environment had to be done somewhat arbitrarily as no traditional guidelines existed. Tabulations of visually estimated wave characteristics from many areas around the world were available (3), (4). However, the question of what area to select as the representative design condition was a troublesome one. What routes the JETFOIL craft would eventually encounter could cover almost any coastal or inter-island area in the world. The problem was eventually managed by examining the wave data from several "rough sea" areas in the world and then enveloping the wave height and period data. This defined a so called "composite sea state" for structural design. Some of the most severe sea conditions were then truncated out because they were sufficiently rough to prevent sustained foilborne operation of the JETFOIL craft. Commercial operation in extremely high seas was obviously unfeasible. Figure 7 shows the long term wave height distribution for this composite sea model. The complete model included a large number of Tsig and Hsig combinations, each with an allotted time percentage of the total operational design life.

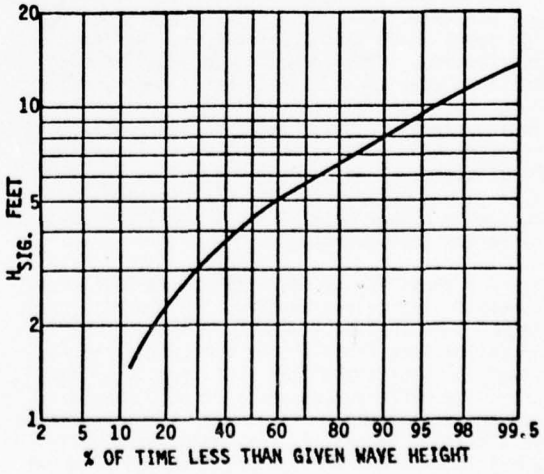

FIGURE 7 COMPOSITE SEA MODEL WAVE HEIGHT DISTRIBUTION

Wave Loading Spectrums

Figure 8 provides front foil wave load exceedance data for several sea conditions. The abscissa is a normalized load magnitude for fully reversible symmetric load cycles. The load value used for normalizing the data is based on the expected maximum rough water load. The three bow sea spectrums for specific wave heights show the dramatic increase of load from a moderate to a rough sea. For example, the exceedance rate of a load value of 0.1 went from 1.5 for Hsig equal 4.0 feet to 350 for a Hsig of 9.0 feet. This is indicative of the sensitivity of fatigue damage to rougher seas which will be more clearly shown in Section VI. Also shown is a design spectrum which is based on the weighting of the composite sea of Figure 7.

An appreciation of the severify of the hydrofoil fatigue environment is gained from a comparison with commercial jet airplane gust loads. For example, Figure 8 shows an exceedance rate of 24 per hour at a load factor of 0.125 for the composite sea environment. A typical design exceedance rate at the same equivalent gust load for a commercial jet liner is on the order of a few per hour. This does not consider the hull slamming and unwetting loads experienced by a hydrofoil which can be more damaging in terms of fatigue than the wave loads.

The change in character of the curves at low exceedance rates is due to the partial use of an exponential distribution for larger seas. In low to moderate seas the Rayleigh distribution was valid, but in higher seas a few of the wave load parameters exhibited a greater frequency of high level loads than predicted by a Rayleigh distribution. This increased activity of high magnitude wave loads is attributed to the major "rough sea" nonlinearities which increase the loading energy (e.g., free surface depth effects and cavitation effects which tend to limit flap effectiveness). Assuming a portion of the load cycle events to be exponentially distributed provided a higher rate of large magnitude loads and better test correlation.

Figure 9 shows the sensitivity of aft foil antisymmetric lift to sea heading. In general, head and bow seas were more severe than beam, quarter and follow seas for all load parameters. Antisymmetric loads showed the most pronounced and surprising differences due to heading changes. From an overall point of view the bow sea is the worst heading because it has the highest antisymmetric lift and strut side loads and also has symmetric lift loads only moderately less than those of a head sea. The antisymmetric load levels indicated for a head and follow sea are of particular interest because theoretically, one would predict an antisymmetric load level of zero, Theoretical wave energy models such as the Bretschneider (1) spectrum are based on one dimensional seas with long crested waves. This condition is never achieved in real seas because some multidirectional characteristics are always present. For example, a typical sea is wind blown waves from one direction (e.g., beam) on top of an underlying swell from another direction (e.g., head). This multidirectional property of real seas is an important factor in the load behavior. However, another suspected factor is the unsymmetric behavior of cavitation patterns which occur on the foils. Cavitation characteristics are very sensitive to the foil contour and because of manufacturing tolerances a truly symmetric foil is never achieved. This results in unsymmetric hydrodynamic loading in head and follow seas. Both of these effects present analytical difficulties for a load simulation approach, the latter being particularly difficult to predict. In any event, the consideration and accurate identification of load effects related to sea heading is very important. A real hydrofoil route must consider a mixture of at least two different headings. For the JETFOIL a 50% bow, 50% quarter was considered to be the most realistic for a design condition.

Figure10 illustrates the sensitivity of foil loads due to the control system mode. In the platform mode, the control system has higher feedback gains which provide more effective "gust alleviation" due to increased flap motions counteracting the orbital wave velocity forces. In the contour mode the feedback gains are much weaker and thus gust load alleviation is less effective causing higher loading. Although the higher feedback gains do provide lift load alleviation, foil torsion loads and flap loads are increased.

Hull/Slamming and Unwetting Loads

Figure 11 illustrates event frequency for hull slamming and foil unwetting loads. The curves are basically empirical but the predicted frequency rates in the low seas have a low confidence level due to a lack of sufficient long term statistics. Using a simplified analytical approach provided some useful trend data for the hull slamming frequency but the foil unwetting event could not be reliably estimated in any analytical manner. Without proper testing and strain gage instrumentation the severity of these loads could not have been established.

As for displacement hulls, head and bow seas are much more severe for hull slamming. Only in the roughest seas does the JETFOIL experience significant slamming rates in a beam, follow or quarter heading. As well as wave height, the slamming rate is also very sensitive to Tsig. For steep waves with a short Tsig the rate of slamming may be high while long swells with a

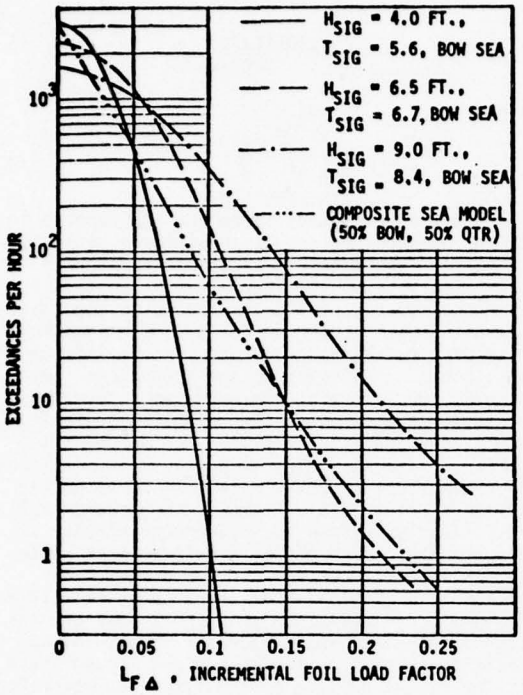

FIGURE 8 FRONT FOIL WAVE LOAD SPECTRUMS

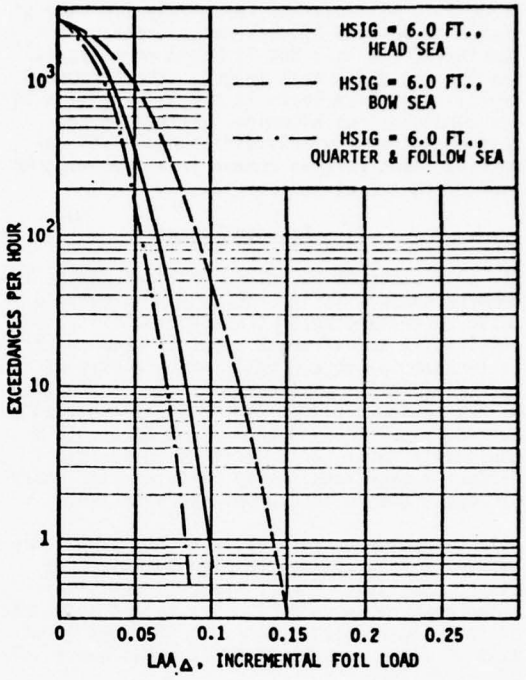

FIGURE 9 AFT FOIL ANTISYMMETRIC LIFT LOAD SENSITIVITY TO SEA HEADING

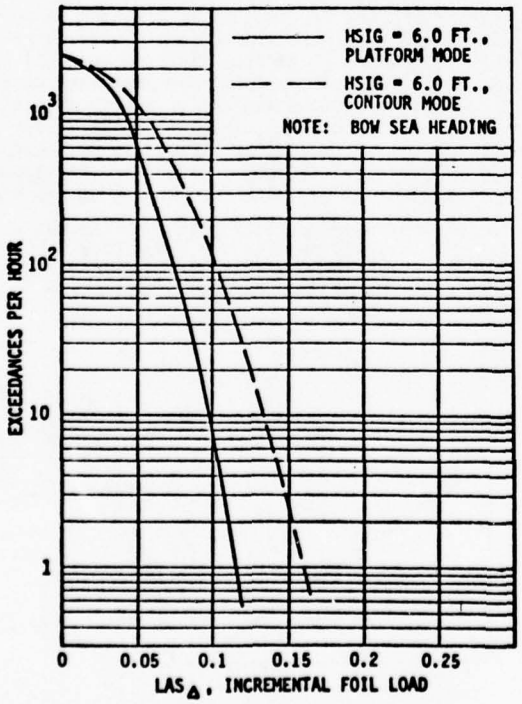

FIGURE 10 AFT FOIL SYMMETRIC LIFT SENSITIVITY TO CONTROL MODE

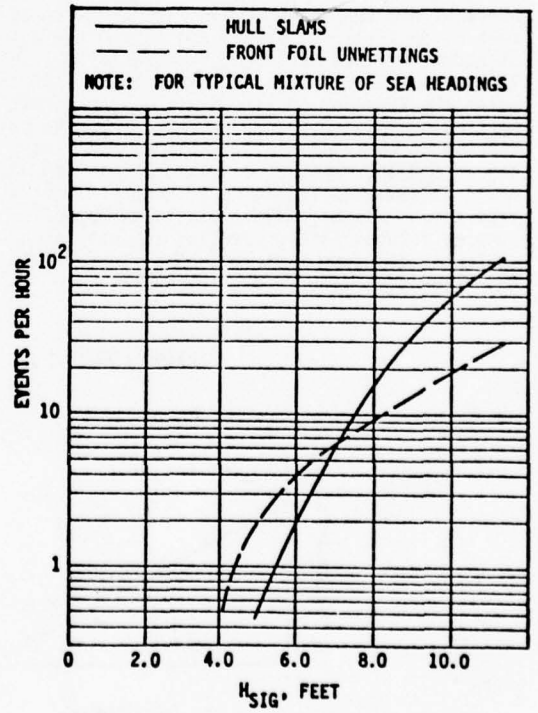

FIGURE 11 FREQUENCY OF HULL SLAMMING AND FOIL UNWETTING LOADS

large Tsig will cause a relatively low rate of slamming. Figure 11 does not illustrate the sensitivity to Tsig but is based on a typical sea for the given wave height. The frequency of foil unwetting loads is not as sensitive to sea conditions as slamming. Effect of sea heading is particularly different. Foil unwetting loads were as common in a following or quartering sea as head or bow.

VI. Fatigue Damage

The prediction of structural fatigue damage is a complex subject in its entirety. However, a basic understanding of the structure's fatigue sensitivity to different types of load spectrums is fundamental to accurate load analysis of the hydrofoil craft. By necessity, simplification of the fatigue loading histories is required to put the total fatigue analysis effort into a manageable form. An understanding of actual fatigue damage sensitivity puts the load analysis requirements into proper perspective.

Fatigue damage or life after a complex loading pattern is generally predicted by using the linear cumulative damage theory, more widely known as Miner's rule[5]. The formal statement of the linear damage theory is that the summation of all fractions of life, or damage equals one at failure.

$$\sum \frac{n_i}{N_i} = \frac{n_1}{N_1} + \frac{n_2}{N_2} + \ldots = 1 \qquad (3)$$

where N_i are the single level fatigue lifes at each given level of loading and n_i are the actual number of load cycles at the specified level. If the damage number is less than one, it indicates the fraction of life "used up" for that particular loading spectrum. The N_i can be calculated in convenient equation form by using linear S-N and constant life plots (Goodman Diagram) illustrated in Figure 12. These linearized curves are approximations to the actual complex fatigue life properties and can be conveniently based on test data at an appropriate characteristic life (e.g., 10^5 cycles).

Thus:
$$N_i = 10^{\frac{(5-\log Y_i)}{\log S}} \qquad (4)$$

where
$$Y_i = \frac{f_{a_i}}{f_{a_o}\left(1-\frac{f_{mi}}{f_{m_o}}\right)} \qquad (5)$$

This technique is used to define the numbers in Table 1 which show the fatigue damage sensitivity to sea conditions of a typical area on the bottom surface of the front foil. The tabulated numbers are arbitrarily normalized to the maximum net damage number which is illustrated for a Hsig of 9.0 feet. The comparisons vividly demonstrate the sensitivity to sea conditions. Operational requirements were based on a commercial route which consisted of a takeoff and landing every hour and a heading mix of 50% bow, 50% quarter. The takeoff/landing cycle was defined by the maximum expected wave load added to the 1g steady lift load. A ground-air-ground cycle is similarly defined for commercial airplanes. For short range routes of airplanes this cycle typically dominates the fatigue damage. For hydrofoil operation Table 1 indicates that it is insignificant unless only moderate seas are encountered. In fact, the comparisons point out that, for a route which encounters "rough" seas a significant portion of the time, the moderate seas are a negligible contributor to the overall fatigue damage. These net damage numbers show a sea of 6.5 feet significant wave height is over 9 times as damaging as a 4.0 feet significant wave height and 9.0 feet is 56 times as damaging! Also evident is the major effect of the infrequent but large loads from slamming and foil unwetting. These large loads are important contributors to fatigue damage for nearly all foil and strut structure but are most dominate for the front foil system. Irrespective of location, all primary foil system structure has the same qualitative fatigue life sensitivity to sea state.

These comparisons vividly point out the basic fatigue analysis problem for hydrofoils operating in the open seas; structural fatigue damage is heavily influenced by those load

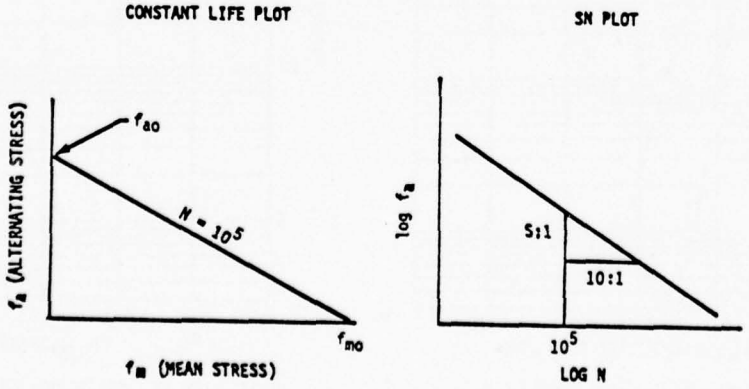

FIGURE 12 LINEARIZED FATIGUE LIFE CHARACTERISTICS

events which are the most infrequent and complicated to predict and those sea environments for which it is the most difficult to obtain accurate statistics. From the hydrofoil design point of view, a great need exists to: (1) obtain better statistics on sea enciron-ments and (2) develop reliable analytical simulation techniques which represent basic load behavior and accurately predict load event frequency for a wide range of environments.

Although the subject of flaw growth will not be discussed in any detail, the author wishes to point out that flaw growth considerations are important to the overall hydrofoil fatigue damage problem as well as classical fatigue. This is particularly true for welded structure. The qualatative fatigue weighting of sea environment discussed above is also applicable to flaw growth. For sizing some structural members flaw growth is the dominant consideration.

LOAD PARAMETER	H_{SIG}, FEET		
	4.0	6.5	9.0
TAKE OFF/LANDING CYCLE (1 PER HOUR)	0.008	0.0143	0.025
WAVE LOADS	0.0099	0.0551	0.162
UNWETTING AND HULL SLAMMING LOADS	0	0.0954	0.813
DAMAGE SUMMATION OF ALL LOAD CYCLES	0.0179	0.165	1.0

TABLE 1 FRONT FOIL NORMALIZED FATIGUE DAMAGE COEFFICIENTS

VII. Analytical Simulations

Although the emphasis on test data to this point suggests that analytical efforts were nil, this was not the case. Two digital computer simulation models were utilized. The primary one which provided a basic statistical analysis tool was a five-degree-of-freedom (heave, sway, pitch, yaw and roll) pertubation model based on the classic spectral response analysis method for linear, gaussian, random processes

$$S_0(\omega)=\left|H(j\omega)\right|^2 S_i(\omega) \qquad (6)$$

where $S_0(\omega)$ is the output spectrum, $S_i(\omega)$ is the input spectrum and $H(j\omega)$ is the complex frequency response function for the chosen output variable. $S_i(\omega)$ is defined from a theoretical sinusoidal wave spectrum model[1], $H(J\omega)$ is computed from the hydrofoil craft model which may include any degree of sophistication in hydrodynamic lift and drag characteristics of the foil surfaces, control system logic and structural properties as long as the model is mathematically linear. It is implicit that the sea model characteristics are also linear. Obviously, this model could not be used to analyze the inherently nonlinear slamming and foil unwetting loads but was potentially valid for foil wave load analysis. Original load magnitudes using this model were seriously low when correlated with test data. By better parameter identification of items like free surface effects, structural flexibility and flap effectiveness the load estimates were increased to provide better correlation with the wave load data for bow and head seas. However, some of the estimates were still deficient, particularly for larger seas. Predicted load behavior for other headings correlated poorly with test data. A particularly divergent comparison is for the antisymmetric foil loads in head and follow seas (Section V).

Further improvements are possible with this approach. For example, multidirectional sea spectras could be employed and piecewise linearization of nonlinear hydrodynamic parameters and wave characteristics is feasible. Many further potential refinements require empirical data for a realistic definition of parameters.

The second model was a complex time domain simulation which included nonlinear hydrodynamic force representations and also a slamming model to predict pressure distributions on the hull due to wave impact. This model was of some help in characterizing foil load behavior during slamming events. However, its complexity and cost was prohibitive for use as a tool to provide comprehensive statistical data. No theoretical representation of the foil unwetting event was available.

VIII. Concluding Remarks

The hydrofoil fatigue load environment from rough water operation is complex, severe and difficult to predict. Primary loading of the foil system structure involves three distinct mechanisms: wave loading from orbital velocities and foil depth changes, hull slamming and foil unwetting. Loading distributions and local panel pressures are complicated by cavitation and constant changes of both waterline location and wetted area of the struts. Major nonlinearities occur for all of the load mechanisms which limits the usefulness of current state-of-the-art theoretical approaches to prediction. Probabilistic descriptions of wave height, wave period and sea heading are required to predict the spectrum of loading events. A lack of accurate statistics on sea environments for a given area is a general problem. This problem is compounded for load spectrum prediction because the most severe and infrequent seas cause the majority of the fatigue damage. These considerations necessitated a strong dependence on test data to obtain a timely definition of loads criteria for the JETFOIL.

A comprehensive amount of test data is required to define the spectrum of hydrofoil load events. The large number of wave load cycles can generally be represented by the familiar Rayleigh distribution and in cases where a Rayleigh distribution is inadequate, a parametric combination of Rayleigh and exponential distributions can be used. The complicated nature and distribution of hull slamming and foil unwetting loads necessitates a completely empirical definition. Because of implementing a large scale test program conducted in several types of sea environments, the JETFOIL fatigue environments were adequately defined. However, the problems and expenses involved with obtaining high confidence fatigue load spectrums from testing points out the critical need for more sophisticated but efficient analytical approaches to predicting the loads. This is especially important for preliminary design.

The state-of-the-art theoretical approaches to analyzing ship responses in a random sea are basically valid for the typical wave loading environment of the hydrofoil where the nonlinear loads of hull slamming and foil unwetting are infrequent. However, further refinements in these linear modeling techniques are needed. Larger waves introduce significant nonlinearities and multidirectional seas can invalidate the typical one dimensional sea representation. From the viewpoint of the hydrofoil structural analyst, there is a need for more direct and statistically accurate measurements of sea environments. Experimental measurements of wave orbital velocity distributions in many types of sea environments is needed for verification and upgrading of the current energy representations of the sea surface. This is particularly important in sea environments which are confused in direction and often common in coastal areas where hydrofoils predominantly operate. Future developments in modeling techniques for hydrofoil loads in a random sea should enhance the ability to concisely define the complicated load environments.

References

(1) "Significant Waves and Wave Spectrum," Dr. Charles L. Bretschneider, Ocean Industry, February 1968.

(2) "Principals and Applications of Random Noise Theory," J. S. Bendat, John Wiley & Sons, 1958.

(3) "Summary of Synoptic Meteorological Observations," U. S. Naval Weather Service Command.

(4) "Ocean Wave Statistics," N. Hogben and T. Lumb, Her Majesty's Stationery Offices, London, 1967.

(5) "Cumulative Damage in Fatigue", M. A. Miner, Journal of Applied Mechanics, Vol. 12, 1945.

EVALUATION OF ROTOR-BEARING

SYSTEM DYNAMIC RESPONSE TO UNBALANCE

Roger E. Thaller and David W. Ozimek
Aeronautical Systems Division
Wright-Patterson Air Force Base, Ohio

A complete investigation of the vibration environment within air conditioner rotating machinery referred to as an Air Cycle Machine (ACM) was needed to effectively increase ACM reliability. To assist in the selection of design changes which would result in improved ACM performance, various design modifications were incorporated into a baseline ACM configuration. For each design change, testing was conducted with the best balance achieveable (baseline) and with various degrees of unbalance. The purpose was to establish relationships between unbalance (within the context of design changes) and the parameters associated with design goals. The results of rotor dynamics tests used to establish these relationships are presented herein.

BACKGROUND

Overview

Air Cycle Machines (ACMs) from Air Force Ground Support Air Cycle Air Conditioner Carts, used for cooling and heating tactical aircraft on the ground, continue to experience an unacceptable rate of failure. At times these failures have reduced the availability, and have seriously jeopardized the mission, of various aircraft. ACMs have been returned for failure investigations and/or maintenance overhaul following rotor seizure or any condition which, by experience, indicated that rotor seizure was imminent. Imminent seizure was determined from such conditions as (1) lubricating oil turning dark, (2) smoke exhausting from the compressor discharge and (3) metallic particles appearing in the oil. Vibration was considered to be a possible cause of failures.

Air Cycle Machine

As shown in Figure 1, the ACM is basically a rotating assembly that consists of a turbine wheel (C) and fan (E) fastened to opposite ends of a common shaft (D). In general, high temperature and pressure air passes through the nozzle (B) and is expanded through the turbine wheel to a lower temperature and pressure air as energy is extracted in the form of work and heat. Work is done on the rotor. Work transformed into heat passes through the angular contact ball bearings (H). The ACM rotor consists of the shaft (D), compressor wheel, turbine wheel, oil slingers (N), and the inner race of each bearing. The remainder of the ACM structure with the exception of the seals and bearing balls, can be considered the stator. The rotor is housed in one section of the stator, the cantilevered cartridge (J). The cartridge is fastened to the turbine end of the main housing (O). The bearings, which provide a dynamic interplay between shaft and cartridge, are preloaded through action of the center spring (P) against each sleeve (Q). The bearings are cooled by action of the oil system which circulates MIL-L-6085 oil. The oil system consists of Dacron wicks (K), capillary tubes (L), the ACME threaded portions of the shaft (M), and oil slingers. Oil is fed to the shaft by capillary action through wicks and tubes and by pumping action generated by the screw threads. Oil is then forced through the bearings by the centrifugal action of the oil slinger.

The ACM is a primary component of the Air Conditioner system. A general schematic of this system is provided as Figure 2. The system input and output air conditions dictate the ACM input and output air conditions which govern the rotor dynamic response. Table 1 provides typical measured values for the governing input and output air conditions. A maximum ACM operating speed of 525 Hz (31,500 rpm) is attained at the 36°C db/30°C wb (97°Fdb/87°F wb) ambient temperature condition.

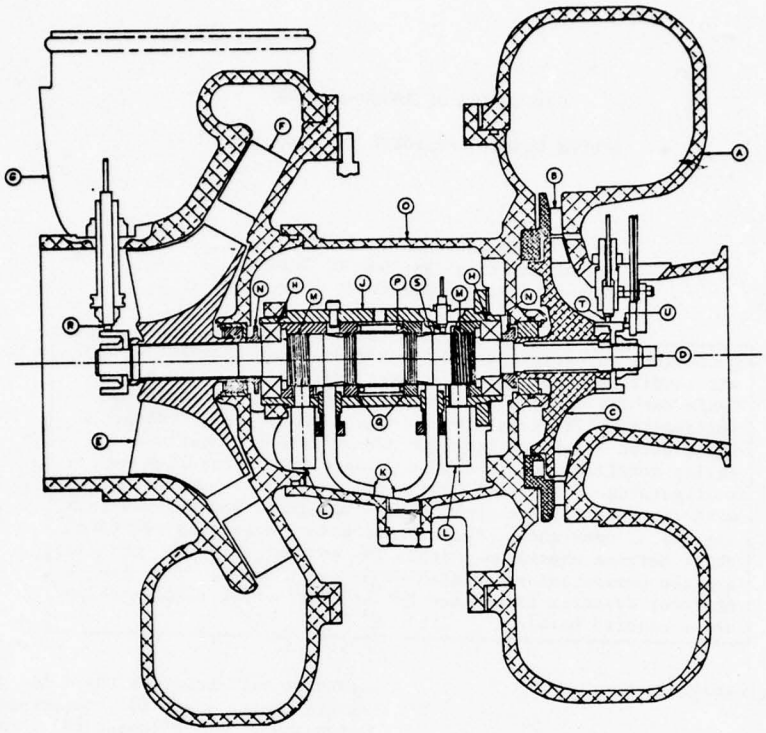

Fig. 1 - Cross Sectional View of Air Cycle Machine

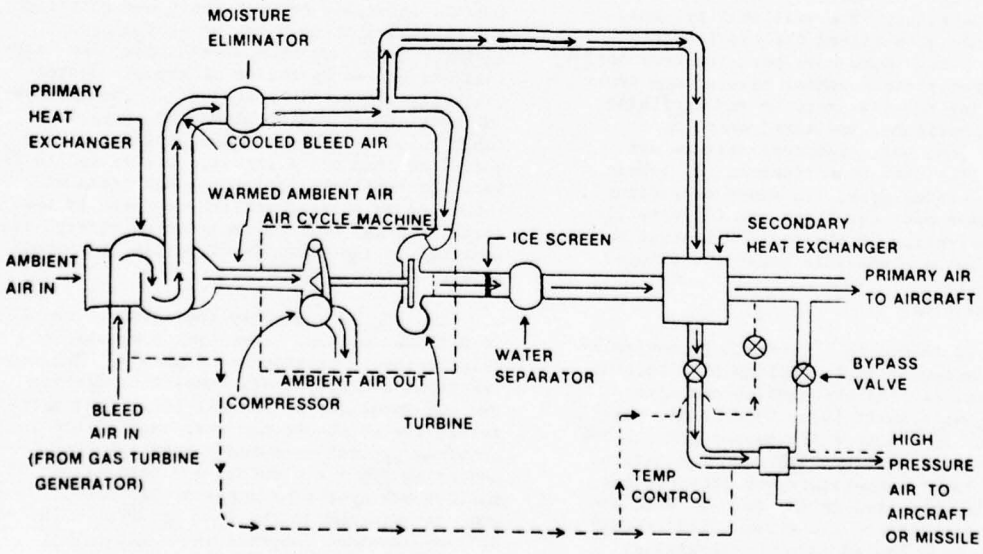

Fig. 2 - Simplified Schematic of Air Cycle Air Conditioner

TABLE 1

AIR CONDITIONER PERFORMANCE DATA*

Ambient Temperature	Bleed Air Into Air Conditioner		ACM Turbine				Air Conditioner Outlet	
			INLET		OUTLET			
db/wb °C/°C	PRES kPa	TEMP °C	PRES kPa	TEMP °C	PRES kPa	TEMP °C	TEMP °C	Relative Humidity %
-3.9/1.7	310	171	276	6.7	165	-10	10	45
10/7.2	307	193	265	14	165	3	11	45
27/18	286	213	238	28	10	1.7	11	55
36/30	262	221	214	38	62	13	14	53
38/29	255	224	207	43	59	14	17	60
54/24	248	232	172	52	48	15	18	60

*All values within this table are normalized for atmospheric pressure of 101 kPa and a delivery pressure of 14 kPa. Delivery airflow is set at 0.53 kg/sec.

Rotor Bearing and Cartridge System Dynamic Performance

The dynamic behavior of the Air Cycle Machine rotor was theorized to be the major cause of ACM deterioration and ultimate failure. Rotating systems tend to whirl or whip at frequencies which are characteristic of the rotor system design. Operation at or around these frequencies could lead to destructive results. These vibration type phenomenon can be either synchronous or non-synchronous in nature. Synchronous whirl is characterized by a slow buildup of transverse vibration with the fundamental frequency equal to a particular running speed of the rotor system. This particular running or synchronous speed is called the critical speed. Synchronous whirl can be primarily attributed to mass unbalance of the rotating system which could result from such factors as unequal load distribution, unsymmetrical stiffness of shaft or bearing(s), oil friction in bearings, and hysteresis damping in the shaft. Non-synchronous whirl is characterized by self-excited vibration induced by various elements in the rotor system. Such elements as seals, aerodynamic pieceparts and fluid film bearings can induce these vibrations thereby causing rotor instabilities which directly result in the non-synchronous whirl condition.

Rotor systems containing rolling element bearings, such as this ACM, are particularly sensitive to system balance when operating at or within a range of one or more system critical speeds. Previous development tests on an earlier generation of this ACM established that at least one first critical speed would be very near the maximum ACM operating speed. The interrelationships between these critical speeds and rotor balance were similarly speculative.

ACM Improvement Project

An extensive ACM Improvement Project was, therefore, undertaken by the PRAM Program Office of the Air Force to thoroughly investigate failures by analytically and experimentally identifying ACM deficiencies and by determining necessary corrective actions. One of many ACM designs currently used in the Air Force was selected for study. The project continues to involve a combined effort between Air Force management, engineering and logistics organizations. Two Air Force contracts were awarded to meet project objectives: Mechanical Technology Inc. (MTI - Latham NY) was required to perform a majority of the analytical efforts and United Aircraft Products Inc. (UAP - Forest OH) was required to simultaneously perform a complete test effort in conjunction with independent analytical studies.

The principle objectives of the ongoing Improvement Project continue to be to provide an ACM which:

1. physically and functionally interface with a given Air Conditioner Cart,

2. meets or exceeds performance and reliability requirements of the governing specification,

3. is compatible with the current high pressure bleed air sources used by the Air Force, and

4. decreases system life cycle cost.

The project was divided into four tasks. A long term study and test effort was determined necessary to identify both ACM failure cause(s) and optimum corrective actions. This effort was divided into three tasks in order to establish a baseline (Task 2), identify optimum design change(s) (Task 3), and demonstrate the acceptability of the optimum design through reliability testing (Task 4). To protect existing operational ACMs from further failure during this long term effort, a short term test effort was required to size an orifice which would reduce the ACM maximum operating speed. This effort (Task 1) is not discussed herein.

In Task 2, baseline performance tests were conducted on two ACMs (S/N 312 and 313) to provide engineering baseline data as well as to define ACM deficiencies. Analytical studies were simultaneously performed to establish correlation between theory and test results. Details of these Task 2 efforts that did not relate to unbalance were presented at the 24th Annual Technical Meeting of the Institute of Environmental Sciencies. The results that relate response to unbalance are presented herein. In Task 3, design changes were analytically assessed and selected for test. The resulting hardware changes were then subjected to a complete testing sequence. After identifying an optimum design approach, the optimum design was further tested in Task 4. A portion of the Task 3 and 4 results are presented herein.

ACM DYNAMIC RESPONSE TESTS

Test Procedures

At the completion of the Task 1 interim fix, the baseline tests were initiated. The same basic test instrumentation was used for all the tests from baseline through reliability testing. A more complete description of the instrumentation and processing technique used throughout these efforts is presented in the following section. Two ACMs (S/N 312 and S/N 313) were tested; each with 13 proximity probes, two accelerometers and a variable quantity of thermocouples and pressure sensing devices. Three of the proximity probe sensors provided the most significant information required for rotor unbalance response analyses. Referring to Figure 1, Y1X (U) provided a measure of shaft rotation; Y1Y (R) and Y5Y (T) provided measures of vertical displacement from the shaft at the compressor end and turbine end respectively. Data was obtained during acceleration of the rotor shaft. For each acceleration run, the data analysis produced plots of Y1Y, Y5Y and the phase angles between the pairs Y1X-Y1Y and Y1X-Y5Y.

During the tests, unbalance was generated by adding calibrated threaded nuts to the compressor end of the shaft for baseline and design change tests. One nut was used for each unbalance condition beyond the baseline unbalance. Calibrated nuts were installed on the turbine end of the shaft during the first part of the reliability test. After this first part, the ACM was returned to a baseline unbalance. The ACM was then allowed to become unbalanced during operation.

During the tests, data were obtained during acceleration and deceleration of the rotor shaft using a preselected range of ACM input/output air conditions. Data were also acquired during ACM operation at a constant speed.

Baseline Tests

In order to provide a starting point or baseline, the existing ACM configuration was chosen for test and analyses. The configuration consisted of an elastomeric O-ring and 120N (27 lb) bearing preload. The O-ring was located between the cartridge and diffuser housing saddle located at the compressor end of the ACM. Preload was provided by a spring located between the shaft and cartridge at the center of the rotor system. The spring provided load to the bearings by transmitting the necessary force through sleeves mounted between the spring and each bearing.

Baseline test results showed unexpected differences in the locations of both the first and second critical speed between the two test ACMs. Differences of at least 50 rps (3000 rpm) were recorded. The resulting analysis indicated that the ACM first critical speed is primarily a function of cartridge stiffness and the second critical speed is primarily a function of bearing rotor stiffness.

Baseline performance tests and analyses also identified deficiencies pertaining to the rotor-bearing and cartridge system of the ACM. Analysis of the baseline data indicated that as a minimum the following three design goals be established:

1. Minimize shaft excursions resulting from synchronous rotor response.

2. Move the machine second critical speed 15% or more above the maximum operating speed (maximum operating speed is approximately 525 rps [31500 rpm]).

3. Minimize shaft excursions resulting from subsynchronous rotor response.

Design Change Tests

The baseline test results led to the development of design changes, each design change was an attempt to achieve at least one of the desired design goals. A 178N (40 lb) bearing preload was determined necessary to sufficiently increase the second critical speed well above the maximum operating speed. Adding either the dual O-ring or the C-ring was to aid in damping

the rotor vibration thereby decreasing rotor excursions over the range of ACM speeds (in particular the first critical speed). An increase in cantilevered cartridge support, accomplished by changing the four bolt circle flange configuration to seven, was to add stiffness to the cartridge, thereby further reducing rotor excursions while increasing the first critical speed.

To achieve the design goals, a variety of ACM configurations was tested. Each configuration was a combination of design changes as identified in Table 2. The first configuration was analytically determined to provide the optimum combination of these design changes. The second configuration was determined to be the optimum design from a stiffness point of view. Neither configuration demonstrated the proper combination of desired response. Therefore, two additional combinations were tested in Phase III. The Phase IIIB configuration demonstrated the type of performance desired. Therefore, this configuration was further tested in another ACM (Phase IVA) to determine if the dynamic performance (in particular the rotor signature) was repeatable. Complete repeatability could not be obtained. However, the Phase IV configuration, tested to determine if the O-ring in the baseline configuration, had served a useful purpose, demonstrated far superior performance over any previous configuration. (Baseline test data indicated that the O-ring had no effect on the performance of one of the baseline ACMs.) The Phase IVB design was therefore selected for the lengthy reliability test.

Reliability Test

To demonstrate that the optimum design was capable of continual and reliable on-off operation in a variable environment, the optimum design was subjected to a sequential reliability test. One ACM was to operate in a cyclic on-off fashion under a variety of ACM input and output conditions until an MTBF of 435 hours was achieved. At least 11 on-off cycles of each combination of input-output conditions identified in Table 3 were to be tested (a total of 528 cycles). The results of this test as well as baseline and design change tests were analyzed to determine dynamic response to unbalance.

TEST INSTRUMENTATION AND DATA PROCESSING

Test Instrumentation

The rotor dynamics investigations were conducted by AFFDL using the instrumentation shown in Figure 3. AFFDL used proximeters with signal conditioning equipment between proximeter output and tape recorder input. The Automatic Gain Ranging Amplifier Units (AGAUs) immediately downstream from the proximeters were used to increase signal voltage levels out of the background ambient noise levels and carry the signals over relatively long cables to the test monitoring station. The second series of AGAUs was used to increase or decrease signal levels to an acceptable range for analog tape input. Time code was recorded on tape along with all data signals for use in data editing and analysis.

Signals from each pair of the shaft end proximity probes were continuously displayed on dual beam oscilloscopes in order to visually check rotor orbits. Signals from each of the remaining probes were also selectively monitored. In addition, for the AFFDL test portion, selective signal activity over the entire frequency (speed) range of the ACM was displayed on the oscilloscopes.

TABLE 2

DESIGN CHANGE TEST CONFIGURATIONS

Test Phase	ACM S/N	Configuration
I	313	178N (40 lb) bearing preload; dual elastomeric O-rings between cartridge and diffuser housing.
II	313	7 bolt flange mounting portion of cartridge; metallic C-ring between cartridge and diffuser housing.
IIIA	312	Increased cantilever support as in Phase II combined with 178N bearing preload.
IIIB	313	178N bearing preload and metallic C-ring between cartridge and diffuser housing.
IVA	312	Same as IIIB.
IVB	313	178N bearing preload and clearance between cartridge and diffuser housing.

TABLE 3

RELIABILITY TEST CONDITIONS

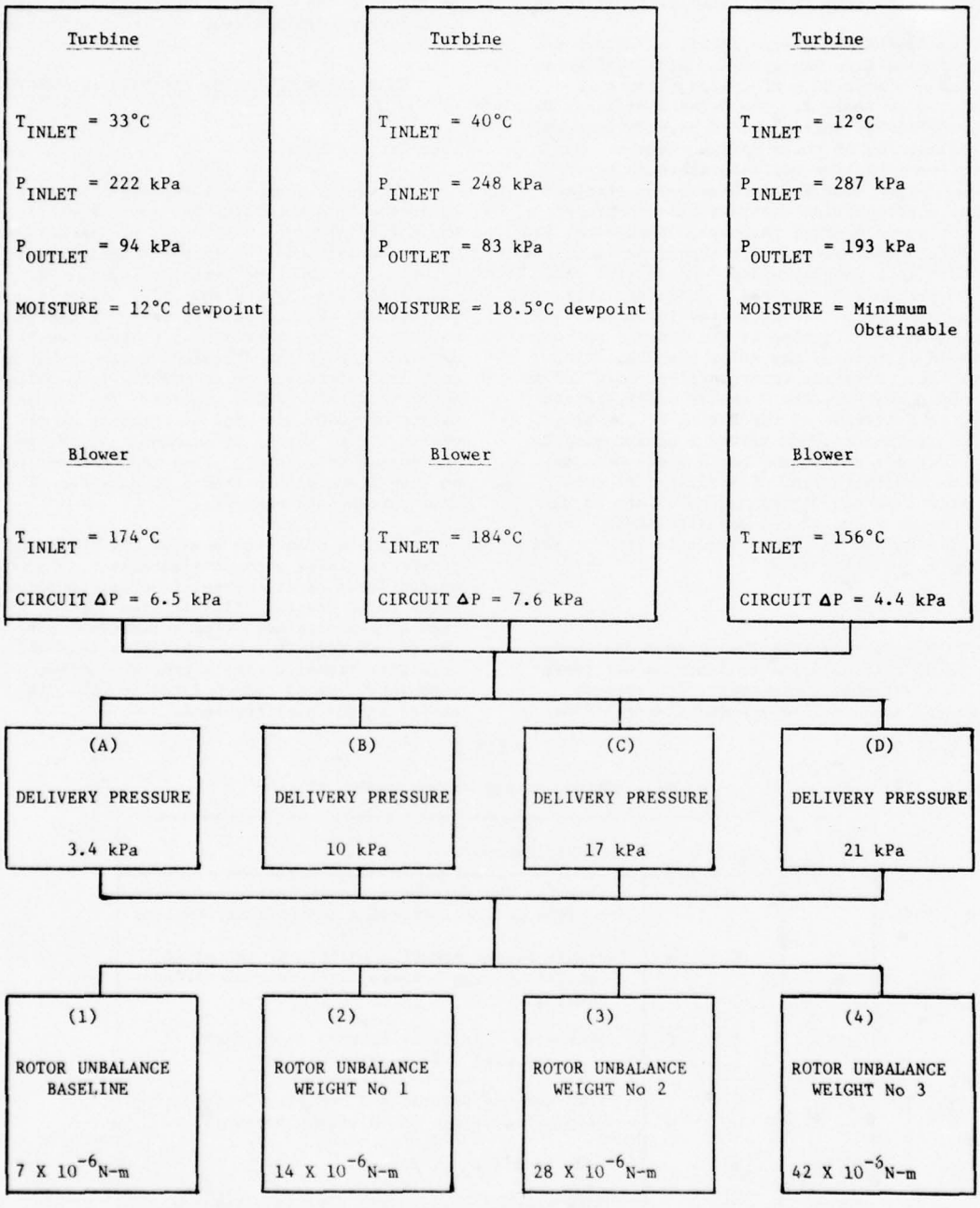

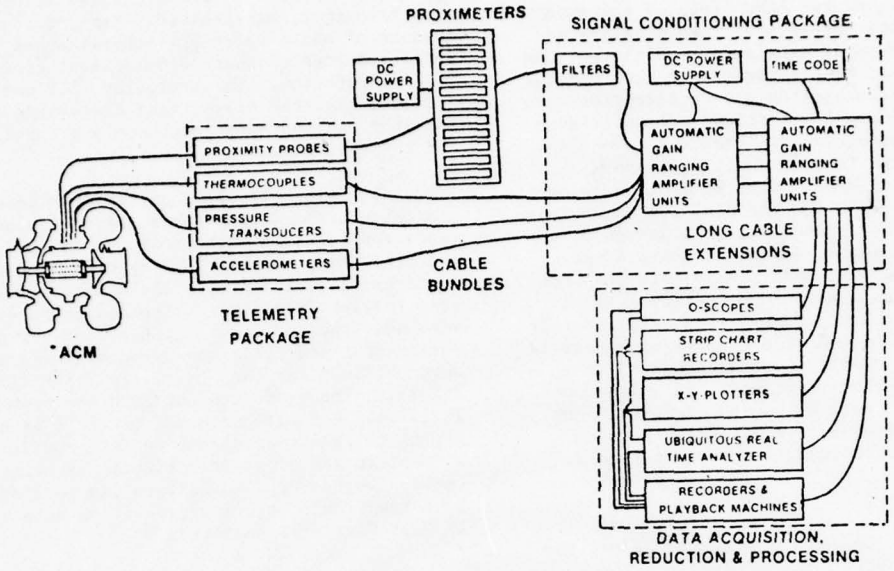

Fig. 3 - Air Cycle Machine Rotor Dynamics Test Instrumentation

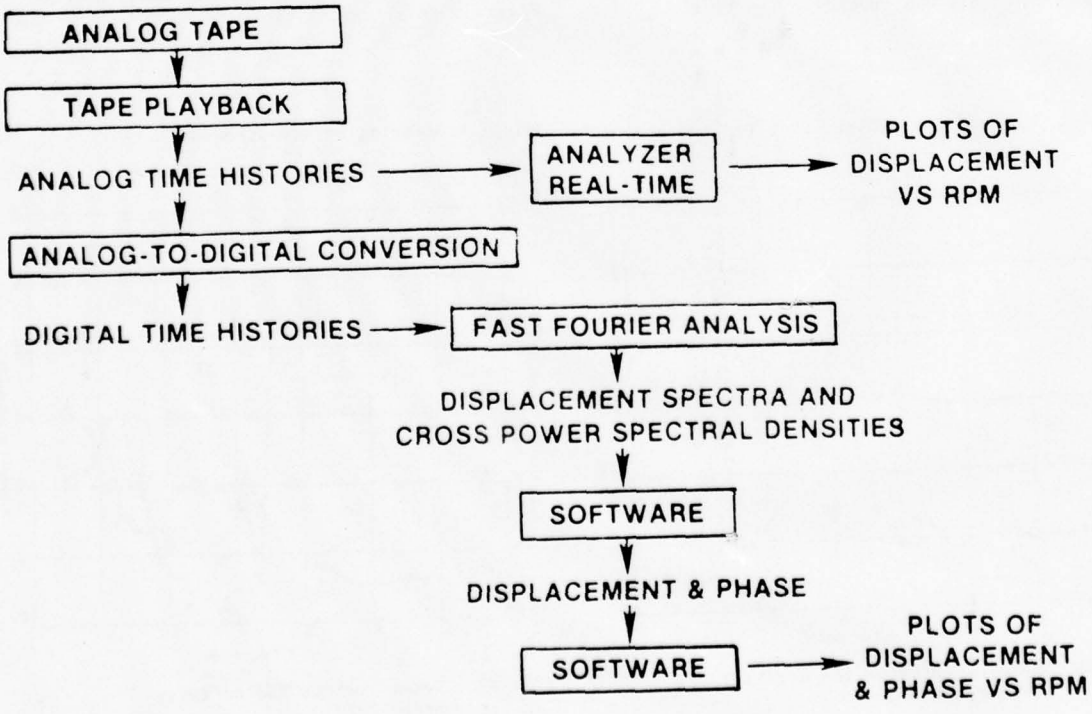

Fig. 4 - Air Cycle Machine Data Processing Methods

For this phase of testing, data were recorded as each of two ACMs (both of the same basic design) was accelerated then decelerated over a range of rotor unbalance conditions. Compressor air inlet temperatures were also varied. Data from the acceleration and deceleration runs were used to locate the critical speeds or synchronous whirl frequencies. Maximum rotational speeds of 583 rps (35,000 rpm), well above maximum operating speed, were monitored during this exercise. Each ACM was also subjected to a series of constant speed runs at a series of unbalance and compressor air inlet temperature conditions. The ACMs were simply held at a constant speed as data were recorded for a short (10 - 15 second) time interval. Speeds for this exercise were selected from a range of speeds in the area of the critical speeds observed from acceleration/deceleration runs. Data from constant speed runs were also used to located any nonsynchronous frequencies which could potentially result in additional rotor excitement.

Data Processing

The bulk of the data processing effort was conducted by AFFDL. Processing of the test data was performed according to the scheme shown in Figure 4. The analog time histories were processed using a real-time spectrum analyzer operated in the peak mode. For each recorded time history, consecutive segments of data were converted to displacement spectra (with a 2 Hz bandwidth) and the maximum value at each frequency was updated. The final spectrum, consisting of the highest values at each frequency, was plotted. Y1X provided a measure of shaft rotation; other sources provided measures of shaft displacement from the axis of rotation. In particular, Y1Y and Y5Y provided measures of vertical displacement of the shaft at the compressor end and turbine end respectively.

The analog signals acquired from each proximity probe during rotor shaft accelerations were also low-pass filtered at 1000 Hz and digitized. Narrow band spectra were produced using a hardware impelemntation of the Fast Fourier Transform. Displacement spectra were acquired for each of the J3 sensors used during test and cross power spectral densities were obtained for each pair, i.e., Y1X-Y1Y and Y1X-Y5Y. The bandwidth for each spectrum was 10.18 Hz. For each interval of .7858 seconds during the shaft acceleration test condition, a complete set of spectra (displacements and cross-power spectral densities was obtained. Each spectrum is the average of the outputs of 16 Fast Fourier Transforms.

The spectra were processed using a Fortran IV program in the following manner. The Y1X spectrum was inspected to determine the shaft rpm during each .7858 second interval. The frequency corresponding to that shaft rpm was stored. For each of the sensors, the software produced a plot of the displacement and the phase with respect to Y1X versus shaft speed. Figure 5 is a typical plot.

Fig. 5 - ACM Rotor Dynamics Data from Analog-to-Digital Processing Methods (Phase IIIA)

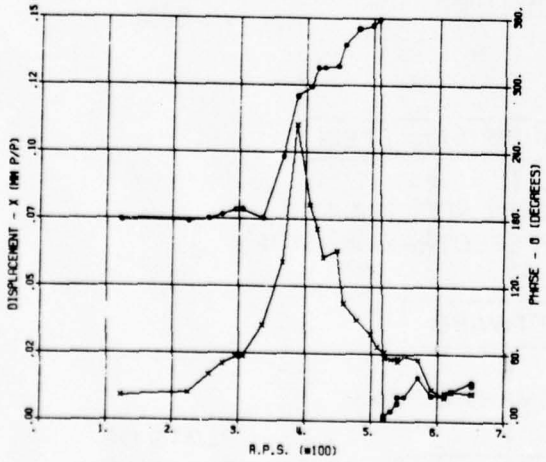

Fig. 5A - Rotor Compressor End Activity (Probe Y1Y)

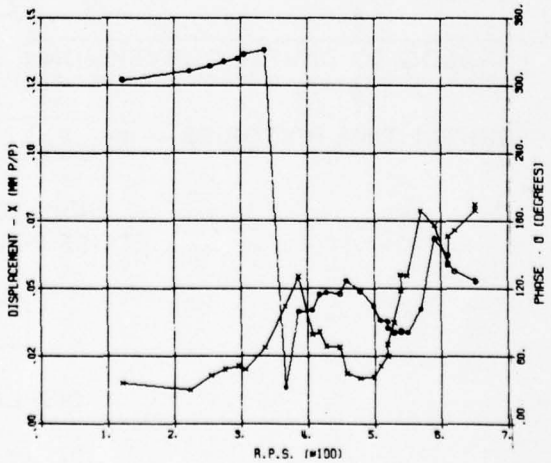

Fig. 5B - Rotor Turbine End Activity Probe Y5Y)

ACM DYNAMIC RESPONSE RESULTS AND ANALYSIS

Analysis of test results involved careful inspection of the curves of displacement and phase versus frequency. Figure 5 is a typical set of curves. Displacement peaks and large phase changes were used as indications of critical speeds. For each test unbalance condition critical speed, the displacement at that speed and the unbalance was then identified and tabulated. Tables 4 through 8 provide these results. For particular unbalance conditions and critical speeds, repeated acceleration runs resulted in different displacement values for the same critical speed. In this case, a range of values is presented. Each table presents the data for a particular configuration. For the baseline test using ACM S/N 312 and for Phase I of the Design Change Test, the data with respect to unbalance is not sufficient for tabulation. For the first critical speed, compressor end displacement is presented; for the second critical speed, turbine end displacement is presented. Information is provided in this manner since both analytical predictions (using the MTI program titled Unbalance Response of a Flexible Rotor) and baseline test data established that the first critical speed is most sensitive to response at the compressor end of the rotor system. Similarly, the second critical speed is most sensitive to turbine end response.

After analyzing baseline data, project design goals became more visible and well-defined. For instance, two of these design goals were to minimize shaft excursions resulting from synchronous rotor response and to move the machine second critical speed 15% or more above the maximum operating speed. Fulfillment of these goals required review of the data to determine the following:

1. The actual relationship between displacement and a range of unbalance for each tested configuration.

2. The actual relationship between critical speeds and a range of unbalance for each tested configuration.

3. An optimum configuration which would provide the minimum displacements over the range of unbalance for the range of rotor speeds.

4. The relationship between displacement, unbalance and operating time for the optimum configuration.

Displacement and unbalance were expected to vary in a direct manner. The manner in which critical speeds varied with unbalance could not be predicted, however. With these goals and expectations in mind, the test results from each task were analyzed and evaluated.

Baseline Test

Table 4 presents baseline test results with respect to changes in unbalance. Changes in unbalance caused the most significant changes in compressor end displacement. The only significant change in turbine end displacement is related to a relatively small change in unbalance. There was no discernible critical speed relationship with unbalance.

TABLE 4

BASELINE DATA
ROTOR DYNAMIC RESPONSE RESULTS
ELASTOMERIC O-RING BETWEEN
CARTRIDGE AND DIFFUSER HOUSING

UNBALANCE	FIRST CRITICAL		SECOND CRITICAL	
COMPRESSOR/TURBINE N-m X 10^6	COMPRESSOR END DISPLACEMENT mm p/p X 10^3	SPEED rps	TURBINE END DISPLACEMENT mm p/p X 10^3	SPEED rps
7/7*	8.4	250	38	467
14/7.8	5.1	267	76	500
42/18	28	250	76	483
56/28	25	267	66	483
150/63	80	283	NO DATA	NO DATA

*BASELINE CONDITION

Design Change Test-Phase II

The results for Phase II are shown in Table 5. With each change in unbalance there is a significant change in compressor end displacement but not in turbine end displacement. First critical speeds for various unbalances do not exhibit a trend. There is an apparent 10 rps (600 rpm) increase in second critical speed for each increase in unbalance. Also, second critical speed is increased by 45 rps (2700 rpm) when ACM unbalance is returned to the baseline condition. No analytical rationale for these trends is available.

Design Change Test - Phase IIIA

Phase IIIA results are shown in Table 6. The compressor end displacement varies with unbalance in the expected direct relationship. Turbine end displacement does not increase with increased unbalance. There are two anomalies in the data. The displacement 0.0026 mm p/p (1.04 mils p/p) for the 7.1×10^{-6}-7.1×10^{-6} N-m (0.001-0.001 oz in.) baseline unbalance is greater than the 0.017 mm p/p (0.69 mils p/p) for the slightly worse $7.1^{+} \times 10^{-6}$-$7.1^{+} \times 10^{-6}$ N-m (0.001^{+}-0.001^{+} oz in.) baseline unbalance. This anomaly consistently appears in the remaining tests. Secondly, the greatest unbalance is related to the smallest turbine end displacement 0.084 mm p/p (3.31 mils p/p). The only significant change in critical speed (a decrease in first critical speed to 377 rps [22,600 rpm]) coincided with the largest increase in displacement.

TABLE 5

DESIGN CHANGE TEST - PHASE II
ROTOR DYNAMIC RESPONSE RESULTS
LARGER MOUNTING FOOTPRINT AND C-RING - S/N 313

UNBALANCE	FIRST CRITICAL		SECOND CRITICAL	
COMPRESSOR/TURBINE N-m x 10^6	COMPRESSOR END DISPLACEMENT mm p/p x 10^3	SPEED rps	TURBINE END DISPLACEMENT mm p/p x 10^3	SPEED rps
3.5/10*	29	347	110	543
56/25	54	382	100	560
150/56	92	363	110	570
3.5+/10+	21	385	130	615

*BASELINE CONDITION

TABLE 6

DESIGN CHANGE TEST - PHASE II
ROTOR DYNAMIC RESPONSE RESULTS
LARGER MOUNTING FOOTPRINT, C-RING
AND INCREASED BEARING PRELOAD - S/N 312

UNBALANCE	FIRST CRITICAL		SECOND CRITICAL	
COMPRESSOR/TURBINE N-m x 10^6	COMPRESSOR END DISPLACEMENT mm p/p x 10^3	SPEED rps	TURBINE END DISPLACEMENT mm p/p x 10^3	SPEED rps
7/7*	26	460	100	568
32/25	32	420	100	583
130/70	110	375	84	373
7+/7+	17	465	100	567

*BASELINE CONDITION

TABLE 7

DESIGN CHANGE TEST - PHASES IIIB AND IVA
ROTOR DYNAMIC RESPONSE RESULTS
C-RING AND INCREASED BEARING PRELOAD

UNBALANCE	FIRST CRITICAL		SECOND CRITICAL	
COMPRESSOR/TURBINE N-m x 10^6	COMPRESSOR END DISPLACEMENT mm p/p x 10^3	SPEED rps	TURBINE END DISPLACEMENT mm p/p x 10^3	SPEED rps
PHASE IIIB - S/N 313				
7/7*	14	342	97	638
42/28	17	305	110	653
140/92	53	300	150	675
7+/7+	9.4	345	110	652
PHASE IVA - S /N 312				
7/7*	58	412	62	575
25/14	41	435	84	595
46/21	75	392	110	602
7+/7+	41	432	56	587

*BASELINE CONDITION

Design Change Test - Phases IIIB and IVA

Two phases of design test, Phases IIIB and IVA, were run with the same configuration. The data for these phases are presented in Table 7. There is an anomalous point in the data for Phase IVA - the compressor end displacement for the $4.6x10^{-5}$-$2.1x10^{-5}$N-m (0.0065-0.003 oz in.) unbalance condition. Except for this point, both compressor end and turbine end displacements are related to unbalance in the typically expected direct manner. The Phase IIIB results showed a high second critical speed (and a relatively low compressor end displacement at the first critical speed). Even though a critical speed - unbalance relationship could not be ascertained, the Phase IIIB configuration was selected as a potentially acceptable solution since a majority of the project goals (and the most of any configuration tested thus far) were met. This acceptability became more questionable when the Phase IVA results did not show complete similarity with the Phase IIIB results.

Design Change Test - Phase IVB

The Phase IVB configuration was tested to determine the effect of the O-ring on the baseline test results obtained from ACM S/N 312 and S/N 313. This configuration demonstrated surprising results with nearly constant low levels of rotor displacement regardless of unbalance. In addition, critical speeds appeared to have no more than a small random variation with unbalance. These findings were sufficient to result in the selection of the Phase IV configuration for the reliability test.

Reliability Test

Data from the last design change test and from the reliability test are summarized in Table 8. For Design Change Test, Phase IVB, there is no significant increase in displacement. Both compressor end and turbine end displacement are not sensitive to unbalance.

The $3.5x10^{-6}$-$1.4x10^{-5}$N-m (0.0005-0.002 oz in.) and $3.5x10^{-6}$-$2.8x10^{-5}$N-m (0.0005-0.004 oz in.) reliability test unbalance were imposed on the machine as all unbalances for previous tests were imposed on ACMs. The machine was then returned to a baseline unbalance. For the series of tests thereafter, the unbalance was not deliberately changed; the ACM rotor was permitted to become unbalanced during operation. Measurements made after the last test showed that the ACM did become significantly unbalanced $2.1x10^{-5}$-$1.5x10^{-4}$N-m (0.003-0.021 oz in.). The $1.4x10^{-5}$-$6.3x10^{-5}$N-m (0.002-0.009 oz in.) unbalance is an estimate.

The imposition of unbalance did not increase displacement at either end of the rotor. When the ACM was returned to a baseline unbalance, the displacement at both ends decreased; the turbine end displacement decreased significantly. When the machine was permitted to become unbalanced, test data showed no increase in displacement at either end of the shaft.

TABLE 8

DESIGN CHANGE TEST - PHASE IVB AND RELIABILITY TEST
ROTOR DYNAMIC RESPONSE RESULTS
INCREASED BEARING PRELOAD AND CLEARANCE
BETWEEN CARTRIDGE AND DIFFUSER HOUSING - S/N 313

UNBALANCE	FIRST CRITICAL		SECOND CRITICAL	
COMPRESSOR/TURBINE N-m x 10^6	COMPRESSOR END DISPLACEMENT mm p/p x 10^3	SPEED rps	TURBINE END DISPLACEMENT mm p/p x 10^3	SPEED** rps
DESIGN CHANGE TEST - PHASE IVB				
7/7*	17	305	47	600
14/11	20	333	45	600
39/21	22	283	47	605
7+/7+	15	335	49	605
RELIABILITY TEST				
7/7*	30-34	283	43	550
3.5/14	34	312	37-39	525
3.5/28	28	337	34-41	517
7/7	18	275	8.7	550
14/63 (EST)	23	257	10-11	550
21/150	19-23	260	6.4	550

*BASELINE CONDITIONS
**Displacement was increasing at upper limit of test run; critical speed was estimated to exist beyond this speed.

There was no discernible trend in first critical speed. Displacement increased at the upper limit of all but one of the acceleration runs. The second critical speed could not be accurately determined. Figures 6 and 7 are plots of the compressor end and turbine end displacements respectively. Each figure includes one curve of displacement versus rotor rps for each unbalance condition.

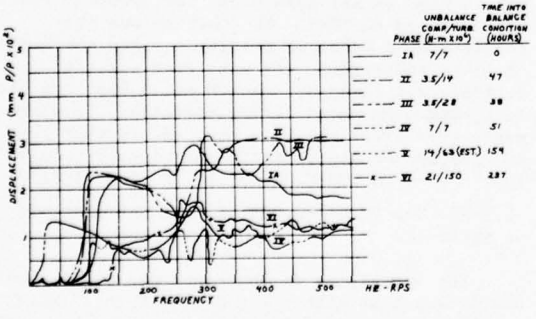

Fig. 6 - Reliability Test Rotor Dynamics Data from Real Time Analyzer Processing Methods. Compressor End Activity (Probe Y1Y)

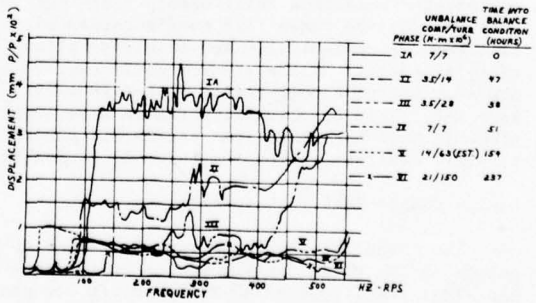

Fig. 7 - Reliability Test Rotor Dynamics Data from Real Time Analyzer Processing Methods. Turbine End Activity (Probe Y5Y)

Review of these figures begins with a comparison of the 335-550 rps (20,000-33,000 rpm) portions of curves IA and II of Figure 6. This comparison shows the only data for which increase in unbalance did not actually decrease displacement. The remaining data of Figures 6 and 7 (curves IA, II and III) showed that increased unbalance reduced displacement at both ends of the shaft. When the machine was allowed to become unbalanced during operation, the data (curves IV, V and VI of Figures 6 and 7) showed no significant increase in displacement at either end of the shaft. These results confirmed the selection of the Design Change Test Phase IVB configuration.

SUMMARY AND CONCLUSIONS

An effort was made to determine the relationship of the rotor dynamic response to unbalance. In each of the tests, the critical speeds (synchronous whirl conditions) varied randomly. Similarly, no specific relationship could be determined between non-synchronous whirl conditions and unbalance. During Phases II and IIIA of the Design Change Test (as in the Baseline Test), there was a direct relationship between unbalance and compressor end displacement due to first critical speed. There was no discernible relationship between unbalance and turbine end displacement due to second critical. During Phases IIIB and IVA, both of the displacements were directly related to unbalance. For the Phase IVB test, there was no discernible relationship between either of the displacements and unbalance. The second critical speed was relatively high and was not significantly altered by changes in unbalance. Although unbalance relationships were difficult to assess, the Phase IVB configuration, by providing the most significant reduction in rotor displacement through a typical range of unbalance, was selected for Reliability Test.

The first part of the Reliability Test involved unbalance imposed on the machine. Concentrating only on the compressor end and turbine end displacement at first and second critical speed respectively, there was no discernible relationship with unbalance. Considering the entire speed range, displacements at both ends of the shaft decreased when unbalance was increased. After the machine was returned to a baseline unbalance condition the rotor operated without any controlled, imposed unbalance. According to the predictions, rotor unbalance increased. However, contrary to expectations, shaft displacements and critical speeds remained nearly unchanged. Further analytical efforts are required in order to determine the rationale for these unusual trends.

BIBLIOGRAPHY

[1]Gary Martin, "Air Cycle Air Conditioners for Aircraft Support," AIAA paper, 76-947.

[2]David W. Ozimek and Roger E. Thaller, "Evaluation of Rotor Bearing System Dynamic Response by Combined Analysis and Test," Aeronautical Systems Division Technical Report, To be Published.

SELECTED TOPICS FROM THE STRUCTURAL ACOUSTICS PROGRAM FOR THE B-1 AIRCRAFT

Peter M. Belcher
Rockwell International Corporation
Los Angeles, California

Three major elements of the structural acoustics program for the B-1 aircraft are considered: (1) acoustic pressures measured at 280 sites on the surface of the vehicle were used to develop pressure models for a resizing of airframe components for aircraft No. 4 (A/C-4), (2) acoustical fatigue design data for two dynamically complex structural configurations were acquired in laboratory programs, the conceptions for and executions of which entailed significant departures from the conventional, and (3) design requirements for mechanical fasteners for configurations other than these two made use of analytical extensions of regrettably limited available information.

Introduction

The Los Angeles Division of Rockwell International Corporation has been engaged since the mid-1960's in development of the manned penetrating attack aircraft, the B-1. A research, development, test, and evaluation program initiated during May 1970 continues. Currently, three of the four test aircraft are on flight status.

Structural acoustics considerations have played major roles, perhaps to an unprecedented extent, in establishment of the design conditions for this aircraft. Because the engines are mounted in nacelles under the wing roots (Figure 1) and are large duct-afterburning turbofans, the majority of aft fuselage and empennage structure was sized for acoustical fatigue prevention. The vehicle has three 15-foot-long, deep weapons bays, required to withstand cavity pressure-oscillations during weapons drops throughout the flight envelope. Outlines of the three sets of weapons bay doors can be seen in Figure 2. The aft structure and the weapons bays house equipment in potentially severe dynamic environments.

Figure 1. The B-1 aircraft in flight.

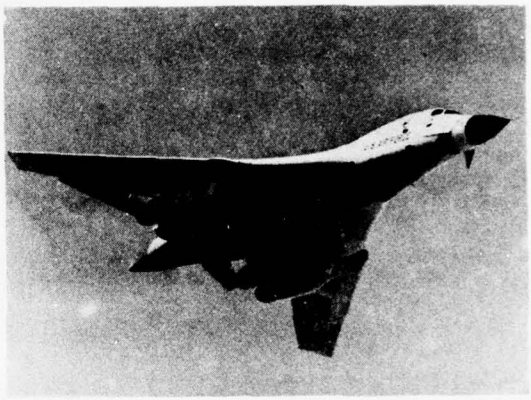

Figure 2. The B-1 aircraft – ventral view. Outlines of three sets of weapons bay doors have been sharpened.

The elaborate and critical dependence of the structural design of the airframe on acoustical fatigue requirements has provided severe tests of the availability of data bases, of laboratory techniques for adding to them, of methods for specifying requirements and combining them with those for other load conditions, and of techniques for their detailed implementation in the design.

This paper considers a selected subset of the structural acoustics work performed in support of the B-1 design, the results of which may have utility for future programs. Specifically, some results of measurements of engine noise on the airframe surface during static ground runs are presented, and the treatment of these results in preparation for a structural redesign is discussed. With regard to design for acoustical fatigue, the somewhat unusual approaches to the acquisition in laboratory tests of design data for two configuration concepts are reveiwed. Some considerations related to mechanical fasteners in acoustical fatigue applications are explored.

Model for Acoustic Loads

Figure 1 shows the aircraft in flight, with the variable-diameter nozzles of the General Electric F101, 30,000-pound-class engines open to the afterburner position. The figure and Figures 2 and 3 suggest the spacial relationship between the aft structure of the airframe and the noise field of the engines. Engine noise ranged from contributory to dominant as a design condition for the fuselage aft of the engine nozzle-plane and for the empennage. Because of the attendant weight and the cost of details appropriate for fatigue resistance, and because an opportunity to fine-tune component thicknesses would exist for much of the structure for A/C-4,

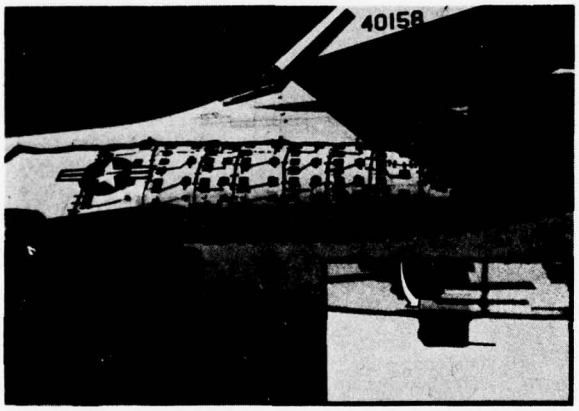

Figure 3. The aft fuselage and part of the empennage of the B-1 airframe, with microphones mounted on the aft fuel bay and aft equipment bay. The blowup shows a mounted microphone, a Bruel and Kjaer 4136.

an elaborate static sound survey for these surfaces was conducted on A/C-1. Measurements were made at 280 locations on the structure for several combinations of number of engines and engine thrust-setting. Figure 3 shows the aft fuselage with the microphones mounted on pads of closed-cell foam. The diaphragms face aft and are about 2 inches from the surface.

The results for four-engine, maximum afterburner operation were used in construction of a model for acoustic pressure on the structure. Some of the steps taken and results produced in that process, as it dealt with the aft fuel bay and aft equipment bay, follow.

Overall Pressure Levels

Overall pressure levels, raised 1 decibel (dB) to correct to sea level from the elevated measurement site, Edwards Air Force Base, and 2 dB for thrust loss related to the ambient temperature, were plotted for eight water and (roughly) buttock lines (Figure 4). The amount of data thins beyond station 1600, as fewer than eight microphones provided coverage on a roughly 20- by 20-inch grid at station planes having smaller cross sections. Some attrition occurred; its effect is particularly evident at station 1640.

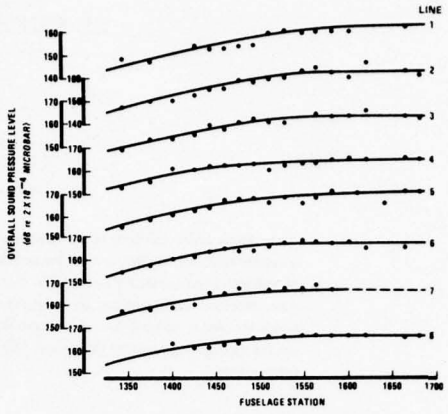

Figure 4. Overall sound pressure levels on the aft fuselage for four-engine, static maximum afterburner thrust, from measurements along eight water and (roughly) buttock lines. The levels are corrected to sea level, standard day conditions. Line 8 is at the bottom centerline.

The resulting smoothed values were cross-plotted for station planes at 50-inch intervals (Figure 5). Interactive smoothing between the two sets of curves provided the results shown here. These levels then were transferred to a fuselage diagram, and smooth contours were drawn. Figure 6 is the result. Figure 7 shows the overall-pressure-level field on the lower surface of the horizontal stabilizer; the contours were developed in a similar process.

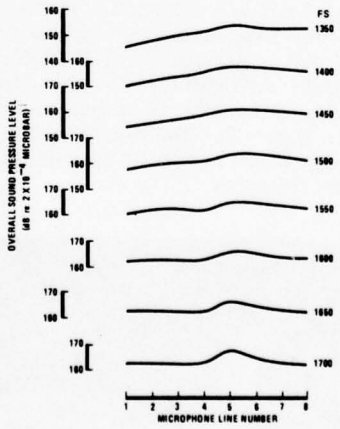

Figure 5. Station-plane crossplots of overall sound pressure levels from Figure 4.

Frequency Distribution

It frequently is assumed for engine-noise predictions that spectra at any station plane have a shape roughly independent of distance above, below, or to the side of the wake, provided those distances are not excessive and that special circumstances, such as surface or ground reflection, do not dominate. (See Reference 1, for example.) Results of work with this large data base support this concept.

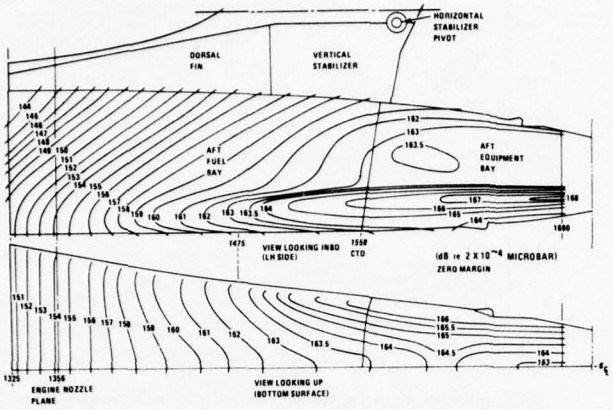

Figure 6. Diagram of the aft fuselage of the B-1 airframe with contours of overall sound pressure level for four-engine, static maximum afterburner thrust. The levels are corrected to sea level, standard day conditions.

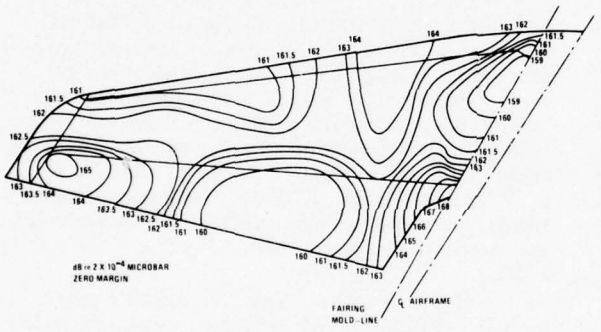

Figure 7. Diagram of the lower surface of the horizontal stabilizer of the B-1 airframe with contours of overall sound pressure level for four-engine, static maximum afterburner thrust. The levels are corrected to sea level, standard day conditions.

Samples from the 15-second records were reduced in one-third octaves from 10 to 8,000 hertz (Hz). Figure 8 presents five (from a total of 17) third-octave plots for roughly equal spaces along the fuselage. Each of the values shown (as dB below the overall level) is the average taken from the signals of all microphones at the indicated fuselage station. The characteristics and suitability of these averages are discussed in the following paragraphs. The distances from the wake to the surface vary from about 10 to more than 100 inches. The closest microphones to the ground (those forward, at the bottom centerline) were 110 inches above it.

These average third-octave-level distributions (involving, of course, logarithms of pressure and frequency) seem remarkable in that they can be approximated tightly in each case by three straight lines (although a gentle S-shaped curve would yield a slightly tighter fit for region III). The lines of Figure 8 are least-square-error fits.

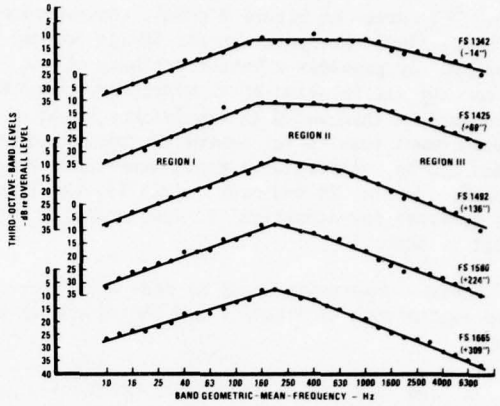

Figure 8. Representative aft fuselage frequency-distributions in one-third-octave bands for four-engine, static maximum afterburner thrust. The plotted points are averages from the signals of all microphones at the indicated fuselage station. The distance each station lies aft of the engine nozzle-plane is indicated.

A model of frequency distribution was constructed for use, with the overall contours of Figure 6, in the A/C-4 design process. For this purpose, each of the 17 station-plane one-third-octave distributions was represented by three least-square-error lines. Figure 9 presents smoothed longitudinal fits to values calculated from the linear representations for several third-octave bands. The curves for the 200 and 630 Hz bands, which define the region II range of the model, approximate the points to within ±1 dB. Those for the 125 and 1,250 Hz bands, which are from the high-pressure portions of regions I and III, respectively, also fit the values from the linear equations tightly. The curves for the 31.5 and 2,500 Hz bands, roughly the middle bands for regions I and III, respectively, manage a close fit at the cost of some distortions in their shapes. This degeneration of shape at frequencies remote from region II continues to the curves for the extreme 10 and 8,000 Hz bands.

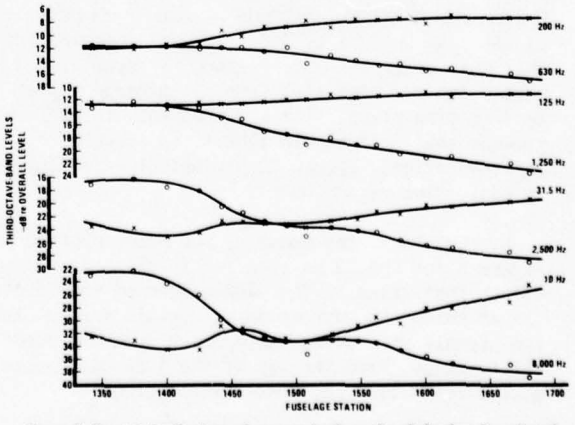

Figure 9. Spacial distributions of pressure levels on the aft fuselage for selected third-octave bands for four-engine, static maximum afterburner thrust. The plotted points were calculated from the linear fits to the station-plane averages.

The curves of Figure 9 permit construction of a three-line representation for design purposes that surely provides a better estimate of the frequency distribution at an arbritrary point on the surface than would interpolations based on measurement results for nearby microphone locations. This can be asserted with particular confidence for frequencies in and near region II, the range of interest for acoustical fatigue analysis, as will be shown.

Several observations can be made about the representations of Figure 8 and the 12 others not shown:

1. The five shown are typical of the 17.

2. The individual band levels "add" to zero dB (to within one-half dB), as is required by the meaning of "overall."

3. The three-line representation is superior in fit to that provided by any single gentle curve.

4. The efficacy of the three-line fit is not a result of the averaging process that leads to the band averages; the same three-segment property is found for the distributions of the single-microphone signals, although, of course, each has more scatter than the average.

5. The trace of the frequencies of intersection between the lines representing regions I and II rises to 200 Hz at about station 1475 and remains roughly constant aft of there. The corresponding trace of intersections between the lines representing regions II and III rises to a peak of about 1,100 Hz in the vicinity of station 1400 and declines smoothly aft of there to about 500 Hz; at station 1680, the region II and III lines effectively have merged.

More needs to be said about the primary ingredient of the frequency-distribution model; i.e., its treatment of the distribution at a station plane as an invariant, and its representation for that purpose by the band-by-band averages of levels (re the overalls) from all microphones at that station plane. It is not obvious on physical grounds that this should lead to an acceptable representation. Figure 10 presents the results of an evaluation of adequacy:

1. Consider, for example, the point plotted in Figure 8 for the 10 Hz band for fuselage station 1342. That value is the simple mean of the levels (in dB below the corresponding overall levels) for the signals from seven microphones spaced around the fuselage, from the top of the fuel bay to its bottom centerline, at that station plane.

2. The standard deviation of those seven levels about the plotted mean was calculated, and from it the confidence interval at the 90-percent level was computed. Similar confidence intervals for the 10 Hz band for the other four stations

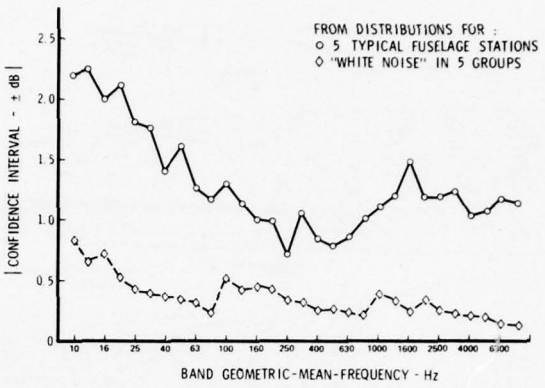

Figure 10. Ninety-percent confidence intervals for the mean third-octave-band levels plotted in Figure 8, treated as if they are means of repeated measurements of a single phenomenon, rather than single measurements of spacially distinct phenomena. The values here are weighted averages of the five intervals corresponding to the five sets of points of Figure 8. Ninety-percent intervals for "white noise" signals identically processed and grouped are shown for comparison.

represented in Figure 8 were computed, and the average for the five was formed. Figure 10 presents that average and those for the other 29 bands. Here, the averages are weighted for the number of contributing signals at each station (i.e., seven or eight). The figure shows a series of averaged intervals of roughly ±1 dB from 63 to 1,250 Hz; this range includes the frequencies of importance for acoustical fatigue performance of the fuel and equipment bays.

3. Also plotted in Figure 10 are the confidence intervals at the 90-percent level resulting from an exactly parallel weighted-average treatment for five groups of seven or eight third-octave frequency distributions for a "white noise" (produced by a signal generator) processed by the same data-reduction program. The comparison demonstrates that the uncertainties shown for the pressure model are attributable to the treatment of the frequency distributions as invariant at a station plane, not to the data sampling and reduction processes.

Acoustical Fatigue Design

The high intensities of pressure sources, large areas of involvement, and multiplicity of incorporated structural concepts make the B-1 a candidate for history's most complex aircraft design with respect to acoustical fatigue. Nonetheless, the practice of this discipline had achieved sufficient maturity that, with very few exceptions, concepts, thicknesses, and detail requirements could be established on the basis of analytical modifications to existing, largely published information.

Some of the concepts in this category of requirements specification by analysis incorporated into the design are skin and frame (or skin and rib), flat and curved; honeycomb, full-depth and panels, flat and curved (aluminum, titanium, fiberglass and graphite/epoxy); beaded or corru-

gated inner-skin panels (aluminum and diffusion-bonded/superplastic-formed titanium); quartz fiberglass panels of various constructions; ported plates on beam supports; large access panels supported by trusses; cantilevered access panels; and integrally stiffened skins (aluminum and titanium).

Two important exceptions to design based on analysis arose. The two configurations were to be used over large areas of the airframe subjected to high acoustic load and, thus, had potential for costly and disruptive maintenance requirements. While these considerations entered into, they did not govern the decision to require tests. What did prove determinant was that each represented a significant and not readily analyzable departure, in ways important to dynamic behavior, from structural concepts for which performance data existed. These exceptions are considered in the following paragraphs. The test programs for them exhibit some unusual approaches to design support and validation.

Aft Fuel Bay

One of the configurations for which test results were required is used for the aft fuel bay. (See Figure 6 for its location.) This 20-foot-long section is constructed of skins supported by lightweight, built-up frames on 8.3-inch centers. The structure forms the tank surface and carries the structural loads in this area. The bay is essentially empty of fuel during ground roll and takeoff, the time during which it experiences significant acoustic load; it is filled to rebalance the aircraft as the wing is swept aft. The configuration differs from conventional skin and frame structure in that it has longitudinal frame-to-frame straps that react fuel-slosh loads and radial frame-web stiffeners that divide the webs into small shear panels. Figure 11 is a sketch of one of the frames, that used for the test specimens. Locations of the slosh straps and web stiffeners are indicated.

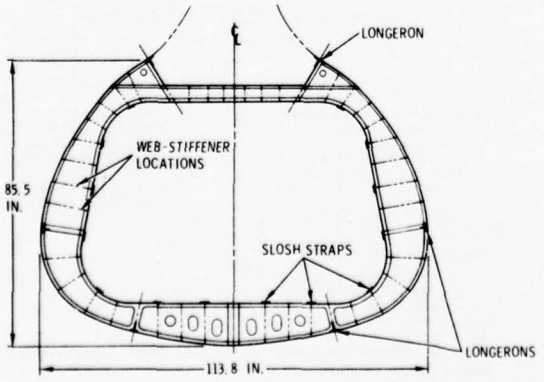

Figure 11. Sketch of the fuel-bay frame at fuselage station 1475. (See Figure 6 for its position in the bay.) It indicates the locations of the fuel-slosh straps and web stiffeners.

The effect of the straps is to replace, in part, the inertial reaction to the rocking motion of the frames by tensile forces in the straps. This reduces skin deflections and stresses through the partial restraint of frame motion, but at the cost of increased web load and of concentrated loads at the strap-to-inner-cap intersections and in the web stiffeners adjacent to those intersections. The sketches of Figure 12 suggest these consequences. Figure 13 shows six straps (horizontal in the photograph) riveted to the inner caps.

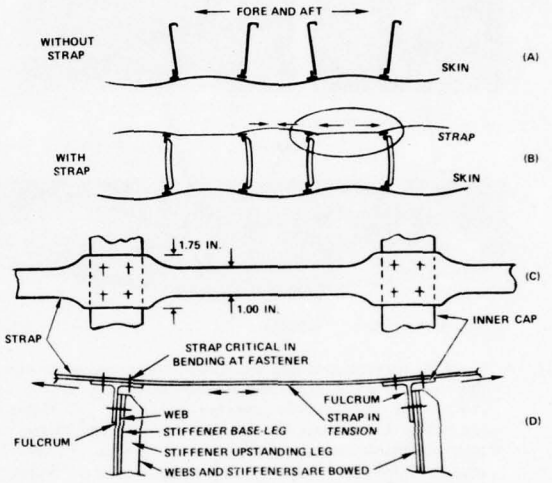

Figure 12. Sketches that indicate the effects of the fuel-slosh straps. In the absence of straps, the rolling motion of outboard caps, induced by unsymmetrical skin motion, is reacted by frame inertia (A). With the strap introduced, the rolling motion is reacted in part by tensile force in the strap (B). The area circled in B is enlarged in D; C is a view looking down on D. Distortions introduced in the components are suggested in D.

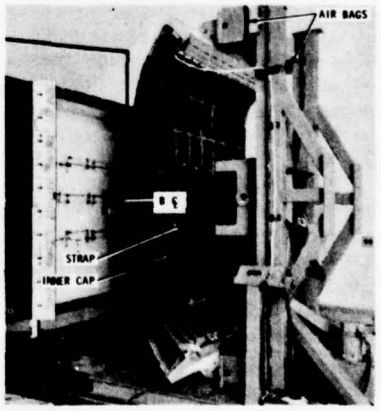

Figure 13. Bottom specimen for the aft fuel bay. The test section, at the left, has a 1- by 6-foot cross section. An overall level of 167 db (re 2 x 10^{-4} microbar), with a frequency distribution that includes a portion flat in one-third octaves at 157 db from 200 to 800 Hz, could be generated for the slightly intrusive specimens shown here and in Figure 17. The propagation direction was parallel to the skin and normal to the frames.

The effect of the stiffeners is to compel reaction to the rolling motion of the outboard frame caps, induced by skin deflections that are unsymmetric about the frame, to occur primarily

at the web stiffeners rather than continuously along the web. The result is locally concentrated load in the outboard frame cap, in the stiffener at its intersection with the cap, and in the fasteners that tie them together. Figure 14 shows a frame segment with some of its stiffeners installed.

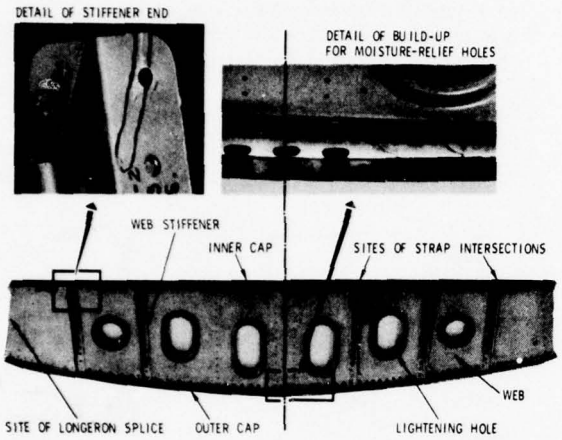

Figure 14. Frame segment from the bottom test-specimen for the aft fuel bay. (See Figures 13 and 18.) The blowup at the left shows the bulbed cap and sharp profile of the original stiffener; these two characteristics were eliminated in a later version. It also shows a crack through a rivet hole, in one of seven modes of failure exhibited by this inadequate stiffener. A local increase in thickness in two steps for all three legs of the outer cap was used to restore its fatigue integrity near moisture-relief holes. (See blowup at right, taken from the opposite side of the frame.)

The Structural Model. The fuel-bay design for the first three test aircraft was based on requirements generated by a structural model; i.e., a series of equations that accounts for its wide variety of curvatures, temperatures, and sound pressures. The coefficients of the model, which determined component thicknesses and fastener requirements, were based on considered estimates, and the details were executed with the informed judgment used for configurations not subject to test. (That judgment included the conviction that the stiffener details shown in Figure 14, initially strongly desired for static strength purposes, could not prove successful.) Requirements generated by the model made clear that acoustical fatigue would dominate the design of the fuel bay. In view of the uncertainty about the effects of the slosh straps and web stiffeners on the performance of the configuration, an absence of test results for use in airworthiness evaluations of the three test aircraft and in the design revisions for A/C-4 would have compelled use of coefficients that were substantially more conservative than those chosen. An unnecessarily heavy and not assuredly reliable structure would have resulted. Optimization through and element sizing by test was essential.

The laboratory tests performed for this purpose were unusual in concept in three respects:

1. The tests evaluated the structural model, used for design of the airframe and the specimens, rather than the fuel bay itself.

2. Optimization was sought through an evolutionary technique of developmental testing, in which deliberately understrength substructure components and mechanical fasteners were installed initially and upgraded as the test revealed relative fatigue strengths. In this process, evaluation and refinement of design details also took place.

3. As a necessary concomitant to the evolutionary method, "step testing," the technique in which testing proceeds in steps of time at progressively higher sound levels, was employed. The method was developed for use with sinusoidal sources; in this instance, a random-in-time source was used.

It is the purpose of this discussion about the fuel bay to exhibit the reasoning that led to these approaches and the techniques of their execution. The equations of the model (with the exception of that shown in Figure 27, which illustrates the genre) are not presented; without sketches of the components and details, presentation of which is beyond the scope of this paper, they would not be useful.

The experimental design for the fuel-bay tests evolved concurrently with development of the structural model. Because of the broad ranges of acoustic load, curvature, and surface temperature in the airframe application and the need for evolution of a configuration optimized for minimum weight, it was clear that a developmental test of the model (with specimens that incorporated all pertinent details), rather than a proof test of the bay itself or a portion of it, would be appropriate. Figure 15 indicates the relationships among the experimental design, the structural model, and the design of the airframe.

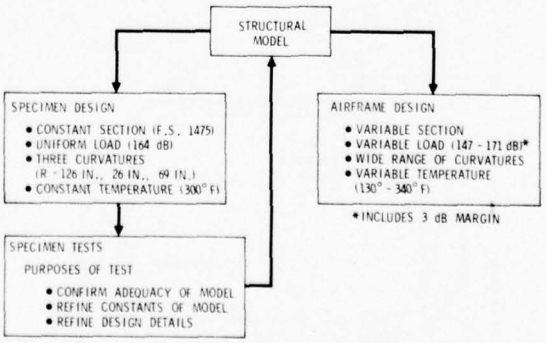

Figure 15. Relationships among the structural model, test specimens, and airframe design for the aft fuel bay.

Evaluation of the Structural Model. The evaluation of the model concerned two assumptions about how the configuration functions; once these

were confirmed, attention could shift to the refinement of constants for thickness requirements and to the performance of details. One of the assumptions is that an existing but not firmly established correction for curvature to skin thickness and, in turn, to the thicknesses for substructure elements (all of which are sized in proportion to the skin) is valid over the wide range of curvatures of the fuel bay. This meant that the specimens had to provide independent tests for a variety of curvatures. The other assumption is that all substructure elements other than fasteners are critical in bending rather than in tension or transverse shear. A description of the specimens and a statement of the criterion for demonstration of the validity of the model follow.

The cross section at fuselage station 1475 was selected for the test specimens because of its wide range of curvatures. (See Figure 16.) The specimen of Figure 13 is from the bottom of this section; it is symmetrical about the bottom centerline of the fuselage. It has a radius of curvature of 126 inches. Figure 17 shows the side specimen mounted in the test window; it represents half of the fuselage, from upper to lower centerline. In that orientation, a region having a 69-inch radius of curvature was exposed to acoustic load. A second orientation exposed the portion between this and the bottom region; it has a 26-inch radius of curvature. A longeron divides the two regions. Parts of a heating system used to maintain the skin at 300° F during the test are evident in Figure 17. The specimens comprise six duplicate frames (those to be tested) and two stronger ones at each end to terminate the specimen and to provide shear-panel terminations for the slosh straps. (See Figure 18.)

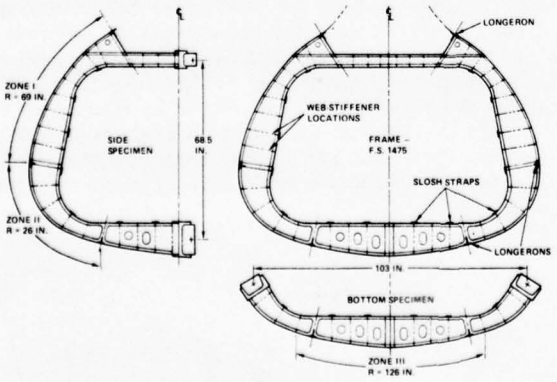

Figure 16. Selection of bottom and side test specimens. The cross section and properties of the frame at fuselage station 1475 are incorporated. Performance for each of three radii of curvature was evaluated independently with the two specimens. (See Figures 13 and 17.)

Demonstration of the validity of the model required that any element type of the skin or substructure that failed in any region would begin to

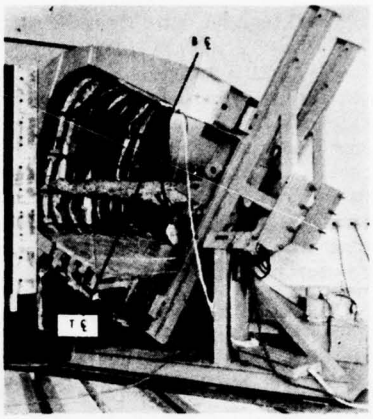

Figure 17. Side specimen for the aft fuel bay, mounted in the test section. The specimen provided essentially independent tests for two regions, i.e., two radii of curvature.

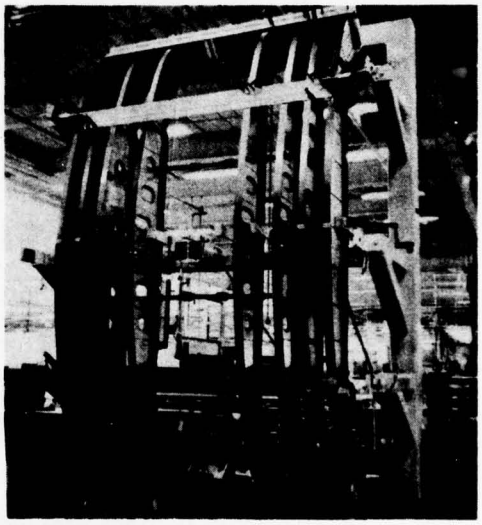

Figure 18. The bottom specimen of Figure 13 in construction. The portions from longeron to longeron of six frames (the third and fourth from either side and two not yet installed), the skin over these frames, and four fuel-slosh straps form the specimen proper. The two frames at each side and the extensions of the six central frames beyond the longerons provide structural continuity and terminate the specimen. A redesigned and redetailed substructure was introduced through replacement of the central portions of the six test frames and the straps. (See Figure 14.)

experience essentially identical failures at roughly the same load/time combination in all regions, i.e., independent of the curvature of the skin. The test results did show uniformity among the regions in load level for, and reasonable comparability in time to, failure for each element type.

Optimization through Evolution. The web stiffeners and slosh straps create redundant load paths, thus rendering analysis of thickness interrelationships for the structural model decidedly approximate. The refinement of these relationships through developmental testing followed this sequence:

1. The skins and outer frame caps, made of a titanium alloy in the original design, were sized by an analytical estimate. The acceptance of a fixed thickness relationship between these two (as a function of frame spacing) was a concession to the long lead times for material acquisition and fabrication for the specimens, a characteristic of parts made from this material. The choice was hedged by simultaneous procurement of additional specimens that differed from the first only in having outer caps of increased thickness.

2. The remaining substructure components, all of which are of aluminum alloy, were sized to be as balanced as analytical limitations would permit, but were hedged to be inferior to the skin.

3. A similar inferiority of fasteners was sought. This was achieved through substitutions for the airframe fasteners by selection among size, material, spacing, and type.

4. The test for each region was initiated at an acoustic level substantially below the design objective for the specimen; this load was imposed for a major portion of the design lifetime. The process was repeated for pressures increased in 3-dB increments.

5. Repairs or replacements were made as components and fasteners exhibited damage.

6. Once patterns of damage occurrence had been established for each component and fastener application in each of the three regions defined by curvature, a resized and redetailed substructure that incorporated the rough optimization implied by the damage interrelationships was substituted for the six test frames and the straps in both the bottom and side specimens. (See Figures 14 and 18.)

7. Testing was continued, supported by additional repairs, until a full lifetime of exposure at the maximum level capability of the facility had been imposed for each of the three regions.

The near-optimum relationships, absolute thickness requirements, and refinements of details established from the results of this procedure were used in a revision of the structural model that governed the A/C-4 redesign. The redesign, of course, made use of the measurement-based loads of Figures 6 and 9.

In an unanticipated result, surface-temperature tests on A/C-1 established that aluminum (rather than titanium) alloy skins and outer caps could be used for the fuel bay. The A/C-4 design incorporates this change at a substantial cost saving and slight weight penalty. The substitution was sized for acoustical fatigue by a routine analytical adjustment of the test results for allowable fatigue stress. Because of the certainty that some loss of optimization resulted from the inability to establish a permissible stress level in the aluminum skins and caps without allowing increases in their stiffnesses over those of the titanium components they replaced, it was decided that proof tests of the revised design would be conducted. The bottom specimen has been tested at design load plus a 3-dB margin. After about 10 hours of the 26-hour objective, a slosh strap failed. The test has not resumed, and the side specimen has not been tested.

Step Testing. The step-test method works well with sinusoidal sources. A full lifetime of exposure to stresses at levels that do damage in a random-load application can be applied for a single mode in a sinusoidal-load test in about 15 minutes. Seldom are more than four modes recognized as potential contributors to significant damage. Thus, loads in a series of several steps, with interruptions for periodic inspections, can be applied in a few days. (See Reference 2, for example.) However, with random-in-time sources, the use of which constitutes a major improvement in testing realism, the accumulation of damage takes place in real time. A lifetime of exposure to the loads of ground runs at high thrust and takeoffs for the B-1, for example, is 26 hours. Only an imperative that transcends time and cost, in this situation the revelation of balance among regions with different curvatures and the quest for optimization, can justify multiple load steps of this duration in a large, costly to use facility.

Stabilizer Structural Boxes

The other configuration for which evaluation in laboratory tests was required is that used for the main structural boxes of the horizontal and vertical stabilizers. This structure has thick aluminum skins to provide stiffness for flutter resistance, multiple lightweight spars of welded titanium sine-wave-web and cap construction, and lightweight aluminum sheet-metal ribs. Figure 19 is a structures diagram for the horizontal stabilizer, and Figure 20 displays the details of the sine wave spar. Minimum thickness on the airframe for manufacturing operations and handling is 0.020 inch for the cap and web; the latter is thinned in two steps by chemical milling to a minimum of 0.012 inch. With few exceptions, these minimum thicknesses are adequate for static strength requirements.

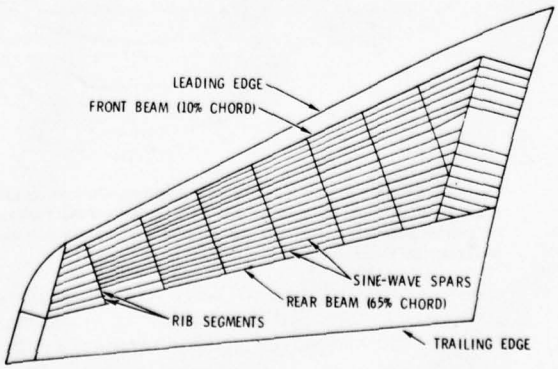

Figure 19. Horizontal stabilizer structures diagram. The 15 sine wave spars and 10 ribs of the substructure are indicated. The ribs are segmented, interrupted by the spars.

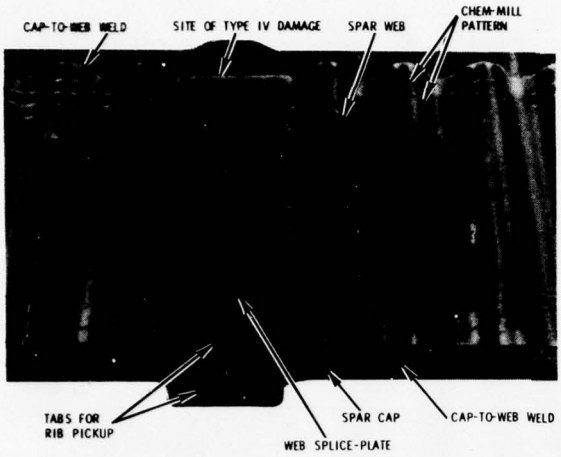

Figure 20. Details of the welded titanium sine wave spar. The material is annealed 6A1–4V alloy.

In acoustical fatigue, the significant motion for this configuration is that in which adjacent skin panels move out of phase with one another, attempting to roll the spar cap and bow the web. (See Figure 21.) The sine wave web provides stiff, broad-based support to the cap; in spite of the thin gauges, the rolling motion is resisted effectively. Nonetheless, because attempts at static stress analysis of the spar for this motion were not rewarding, no strong preconception of acoustical fatigue adequacy could be sustained; it was necessary that tests be performed (1) to provide an evaluation of the airworthiness of the stabilizers of the first three test aircraft and (2) to supply quantitative requirements for the A/C-4 redesign or, alternatively, to establish what additional tests would be necessary for the latter purpose.

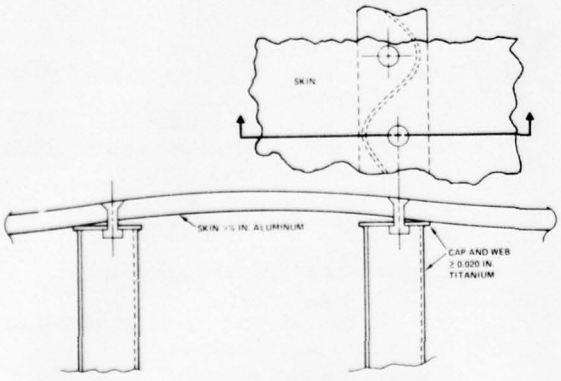

Figure 21. Sketch suggests, by exaggeration, the effects of loading of sine wave spars by a thick skin undergoing unsymmetrical deflection. The skin attempts to roll the caps and bow the webs, but the spar geometry is stiff enough to resist effectively. The result is fatigue damage to the cap and web adjacent to the weld that joins them and to the skin-to-spar fastener.

The test plan developed for this purpose is noteworthy in three respects:

1. The program involved a decidedly unusual example of simultaneous tests of several boxes in a large facility. These were made the elements of two larger specimens, so that the ribs that formed interfaces between the boxes could be evaluated along with the spars. The virtue of economy was complemented, in fact overtaken, by necessity.

2. Each specimen included individual boxes of widely varying strengths. Therefore, as for the fuel bay tests, stepped loading was used. Mechanical neutralization of damaged boxes permitted continuation of the test.

3. This program of limited and not obviously adequate scope provided all the information necessary to support quantative design requirements for the airframe.

Experimental Design. Figure 22 illustrates the scheme from which the component combinations were selected. Results from tests whose component sizes are governed by a fully-filled cube of 27 combinations (to account for three values each of three independent variables) would be required in principle to establish the functional relationships among allowable acoustic load (for one lifetime, for example) and the spar-related independent variables: spar spacing, and cap and web thicknesses. Limitation to even this large number (1) assumes scatter sufficiently small that the relationships are not obscured, (2) does not provide for the required information regarding rib and fastener damage, and (3) requires that damage not related to the spars does not intervene. In these tests exogenous variables, unshimmed gaps between the rigid skins and other components, assured wide scatter. Spar damage traceable to prior rib failures, a combination referred to below as the rib/type-IV syndrome, occurred; it proved to be of primary importance for airworthiness evaluations of the stabilizers.

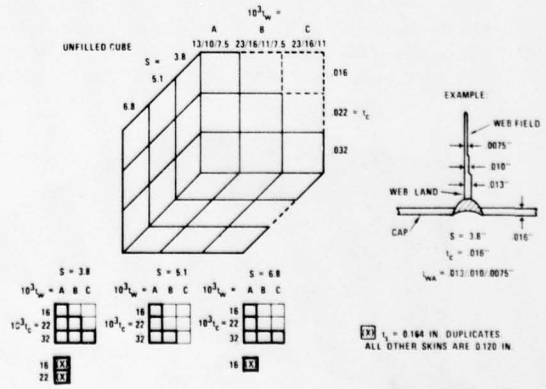

Figure 22. Component-size combinations for test of the stabilizer configuration. Some components having thicknesses below the manufacturing minimums for the airframe were included to increase the likelihood that failures would occur for a range of values of the variables.

In recognition of the uncertainties about performance, of part and test costs, and of time limitations, it was decided that a preliminary series of tests would be conducted to evaluate the 18 combinations of Figure 22. A limited objective of the establishment of minimum capabilities for the spar components and of functional relationships for rib thicknesses and fasteners was inherent in this choice.

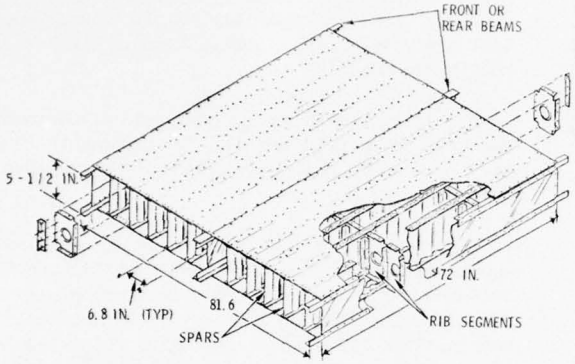

Figure 23. Sketch of stabilizer specimen HS-1. The specimen was mounted so that one skin formed the closing wall of the test chamber. The propagation direction was normal to the spar and beam planes.

Test Specimens. Figure 23 is a sketch of one of the two specimens. This specimen comprises three major beams (simulations of the front and rear beams of the airframe), the six boxes of Figure 22 that have 6.8-inch spar spacing, and eight sets of ribs. Because the rib elements at the open ends of the specimen could be replaced easily and those inside only with great difficulty, the former were sized initially at 0.025 inch at one end and 0.032 inch at the other. One line of inner ribs was set at 0.040 inch, and the other at 0.050 inch. The other specimen contains 12 boxes, four with 5.0- and eight with 3.8-inch spar spacings; it has four major beams, five lines of ribs, and similar rib-thickness arrangements (Figure 24). The maximum aspect ratio for individual skin panels for each of the two specimens is 3.5 (i.e., effectively infinite).

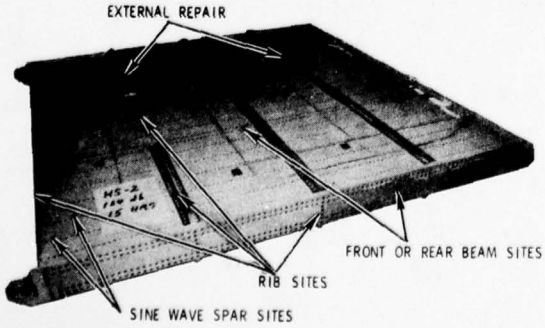

Figure 24. Stabilizer specimen HS-2. External stiffeners are fastened to the skins over failed ribs.

Test Procedure. Table 1 lists the levels and durations for the step-test procedure. Figure 24 shows the second specimen after substantial damage had occurred. Eight of the nine internal ribs had failed; external supports had been applied over them on the upper and lower skins. The end ribs had been upgraded. Some spar damage had been detected at the time the photograph was taken; for that reason, stiffeners were to be applied over the damaged boxes themselves.

Table 1. Test levels and durations – stabilizer specimens

Overall level*	Test duration (hours)	
	HS-1	HS-2
152	15	-
155	15	-
158	15	15
161	15	15
164	15	15
167	15	40

*In dB re 2×10^{-4} microbar; the frequency distribution included a portion flat in one-third octaves from 200 to 800 Hz, 10 dB below the overall level.

Test Results. The results from the tests of these two specimens provided all information necessary for the redesign for A/C-4. Table 2 summarizes the types of damage. It can be interpreted more readily with the help of Figures 20 and 25:

Table 2. Types of damage – stabilizer specimens

Skins - no damage

Front and rear beams - no damage

Spars - damage in four modes:

- Type I - scalloped cracks of caps
- Type II - web-land cracks adjacent to cap welds
- Type III - web-field cracks*
- Type IV - web splice-plate cracks adjacent to cap welds

Ribs - cracks in rib segments and clips

Fasteners - losses in five applications:

- 2219-T81 regular head rivets through lower skin into spars and ribs
- 2219-T42 (Inconel 600 stem) Cherry bulbs through upper skin into spars and ribs
- 2219-T81 protruding head rivets in substructure

*The chem-mill lines of the web fields were not sites of damage.

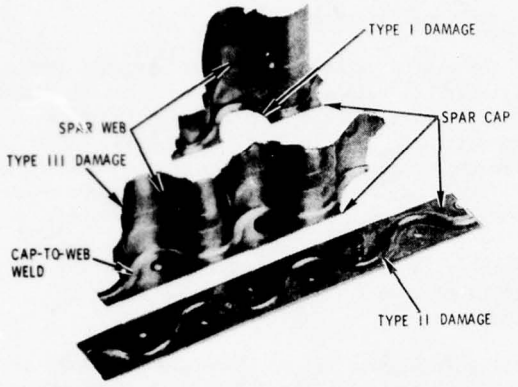

Figure 25. Illustrations of damage types for the sine wave spars.

1. Type I spar damage is a primary failure. Prevention of its occurrence on the airframe requires caps of more than minimum thickness in only a few areas of combined high acoustic load and wide spar spacing. A number of incidents of type I damage occurred in the tests as a consequence of unshimmed gaps between the caps and the skins; fastener-induced preload in the cap results. A shim requirement that limits the mismatch to 0.010 inch for the airframe precludes damage attributable to this condition.

2. Type IV damage is derived, or secondary. Only when the rib segments at both sides of a web splice-plate have failed is the plate free to move enough to fail. The failure is on the plate at the plate-to-cap weld; thus, it is similar to the type II failure on the web proper. Type IV failures in the test soon were followed by secondary failures of the adjacent webs in either the type II or III mode.

3. A few cases of primary types II and III web damage (i.e., damage not incident to the rib/type-IV syndrome) occurred. These were used to set minimum thicknesses for the webs. A slight increase beyond the minimum thickness for fabrication over a small area of the horizontal stabilizer resulted.

4. Fortunately, both on their own account and in view of their role in the type IV spar-damage syndrome, a great deal of information about thicknesses for the rib segments was obtained. Figure 26 presents these results. Here, "primary" refers to the first failure of any segment in one of the six-segment ribs. "First secondary" refers to the first occurrence of failures of an adjacent pair of segments, the damage mode essential to the type IV syndrome. The first secondary failures collapse reasonably well to the function noted in the figure; the primary failures do not. The dashed line and "design line" have the slope of that function. Note the weak dependence of allowable pressure on spar spacing. For the A/C-4 design, the acoustical fatigue requirement exceeds that for strength for approximately half of the rib segments of the horizontal stabilizer and for a few of the vertical stabilizer.

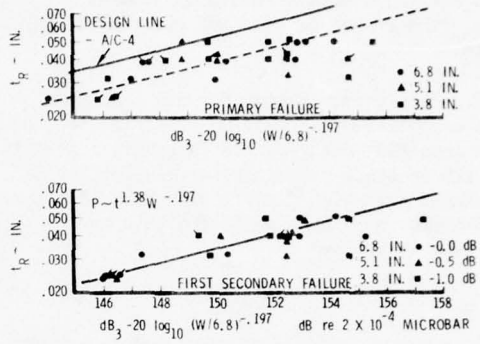

Figure 26. Damage data for the rib segments of the stabilizer specimens adjusted to one lifetime. A "primary" failure is the first in any segment of a six-segment rib; a "first secondary" failure is the first occurrence of back-to-back failures of two segments in a six-segment rib. Here, P is allowable pressure, t is rib thickness, and W is spar spacing.

5. A substantial number of fastener failures, in all five classes of application noted in Table 2, yielded adequate information for design. For A/C-4, roughly half of the fasteners in the horizontal stabilizer and some in the vertical stabilizer are governed by the results of these tests.

The wide variety of modes of failure, primary and derived, assured that only limited information for requirements could be obtained for the caps, web lands, and web fields. The design values for these components were established from a combination of primary failures and undamaged parts. They are, therefore, somewhat conservative over the range of spar spacings represented in the test. That these conservative requirements led to only a small weight penalty for A/C-4 meant that further tests were unnecessary.

Design Requirements. The design values for A/C-4 established on the basis of these test results form a structural model for the configuration, equally applicable to the horizontal and vertical stabilizers. It is a series of 15 equations, the subjects of which are the components and fasteners listed in Table 2. Two examples from that description are considered here:

1. The thicknesses of bent-flange sheet-metal rib segments, in inches, are controlled by:

$$\log_{10} t_R = dB_3/27.6 + 0.143 \log_{10} W - 6.839, \quad (1)$$

$$3.0 \leq W \leq 8.0$$

where W is the spar spacing in inches. This equation corresponds to the "design line" of Figure 26. The safe range of applicability is

limited to small extrapolations beyond the 3.8- and 6.8-inch extremes of spar spacing represented in the specimens. The design pressure is stated as a one-third-octave level; as Figures 7 and 19 show, it need not be constant over the length of a rib.

2. Once a requirement for rib thickness has been established, it must be satisfied for the equations that describe the fasteners that attach the rib to other components. The limiting rib thickness for which a particular blind fastener of diameter d is applicable for joining the skin and ribs is set by:

$$t_R \leq (3.35 \times 10^{-1} \times F_F/F_R \times 1/s)^{1/2} \times d \qquad (2)$$

where s is the rivet spacing and l is the lever arm defined in Figure 29. Any consistent set of units is acceptable. The factor F/F is a dimensionless ratio of figures of merit in fatigue for the fastener and the rib. The ratio is near unity if the fastener and component are of alloys of the same material, e.g., aluminum or titanium. If these two are mixed, the ratio is approximately four (or one-quarter).

Other Tests

It should be clear from the foregoing that the test methods used in the B-1 acoustical fatigue development program place emphasis on the production of damage. There is no more definitive evidence of convergence toward optimum design than failures for each component and fastener application.

In contrast to this dependence on step-by-step destruction, two proof tests were performed without recourse to stepped loads. One of the subjects was a large two-box specimen that represented the two limiting load-to-strength conditions in a graphite/epoxy-composite version of the horizontal stabilizer. The load was taken immediately to the design level (including required margin) for the design life. No detectable damage occurred. This configuration, selected for A/C-5 and beyond, would have provided a substantial reduction of weight from that of its metallic predecessor at similar cost. The other proof test was of a diffusion-bonded/superplastic-formed titanium access panel in the form of a corrugated sandwich. It demonstrated that the local details characteristic of this fabrication process do not degrade the acoustical fatigue advantages for which sandwich panels and annealed 6Al-4V titanium alloy are known.

Mechanical Fasteners

Currently, only very limited information is available regarding design requirements for mechanical fasteners for acoustical fatigue prevention.

Tested Configurations

The test programs for the fuel bay and stabilizer structural boxes provided definitive requirements for fasteners appropriate for those configurations. Equation 2 is an example of this information for the stabilizer configuration. For the fuel bay, seven application situations exist for each of the individual frame assemblies; several other applications occur in the bay assembly, along longerons and intercostals, at longeron/frame intersections, and for skin splices.

Figure 27 provides an example of a design requirement for A/C-4 established through the extension by analysis of information from the fuel bay tests. It is for the web-to-inner-cap rivets, except for those that also pass through the stiffener ends. (See Figure 14.) The inboard cap is restrained in translation and rotation by the slosh straps; unsymmetrical skin motion bows the web. This induces tensile load in the web-to-cap fasteners that is experienced principally by the fasteners at the ends of those stiffeners that tie to the inner cap immediately adjacent to the intersections of the cap and straps. Thus, the spacing of web stiffeners is significant because it controls the allocation of reaction to roll of the frame between the stiffeners and the web. Note the similarity of form of this equation to that of Equation 2, even though the situations described are substantially different. This constant is larger principally because the fasteners at the stiffener ends carry most of the load.

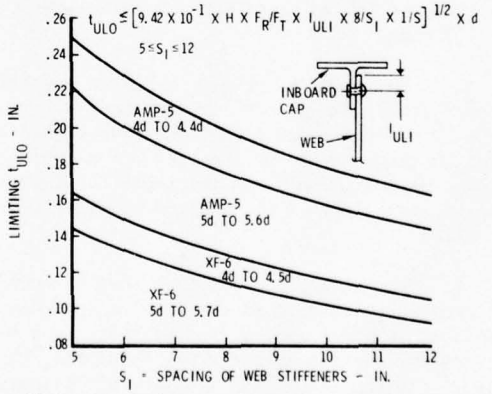

Figure 27. Example of a fastener requirement for the aft fuel bay, that for the web to inner cap. The fastener/spacing combinations are recommended for the labeled zones but are, of course, acceptable for lower zones. The web-stiffener spacing S_i is compared to 8 inches, a standard. H is a "head factor" for the rivet, unity for the XF-6, and 0.8 for the AMP-5. The lever arm l usually is about two fastener diameters, but not less than three-eighths inch, in length.

The equation specifies the requirement in terms of a limiting allowable thickness of the upstanding leg of the outboard cap; all substructure components and fasteners are controlled from this quantity; it incorporates the effects of applied load, frame spacing, curvature, surface temperature, and material properties. Two fastener types,

both having protruding heads, are permitted. The XF-6 is a 3/16-inch-diameter 2219-T81 aluminum rivet, and the AMP-5 is a 0.164-inch-diameter Cherry bimetal titanium rivet. The allowable range of upstanding leg thickness for each type of fastener depends on the rivet spacing, stated in the equation in inches and in the diagram as multiples of the fastener diameter.

Other Configurations

Somewhat surprisingly, almost no information about fasteners existed to support the design by analysis for the many concepts for which tests were not conducted. This necessitated formulation of analytical criteria, for a variety of fastener types and materials, applicable to the fastening of the skin and substructure of each of several configurations. Functional relationships similar to that of Figure 27 resulted that probably are valid, but the lack of data to provide constants of proportionality dictated a conservative bias in their use.

Some information on skin fasteners for extended skin and rib structure (Figure 28) was included in Reference 3, an indispensable source of data for acoustical fatigue analyses. However, the stated functional relationship, derived in the reference, is not that plotted. The information is useful only if the example superimposed on the nomograph reflects measurement results; if it does, it supplies a valid constant for the proportionality. That uncertainty aside, the information of the figure is inherently limited in utility:

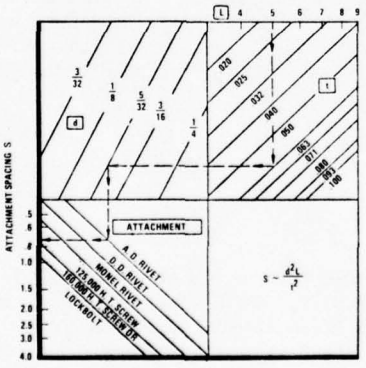

Figure 28. Published design criterion for fasteners in skin and rib extended structure, reproduced from Reference 3. Note that the function and the plot do not match. The notation is that of Figure 29.

1. It is applicable only to skin and rib or skin and frame structure.

2. It has no substructure information except that which can be produced by analytical extension.

3. It apparently applies to in-phase motions of adjacent skin panels.

Figure 29 presents a derivation, parallel to that which produced the proportionality in Figure 28, for a skin-fastener relationship for out-of-phase adjacent skin panels, a motion probably substantially more significant than in-phase motion for acoustical fatigue damage.

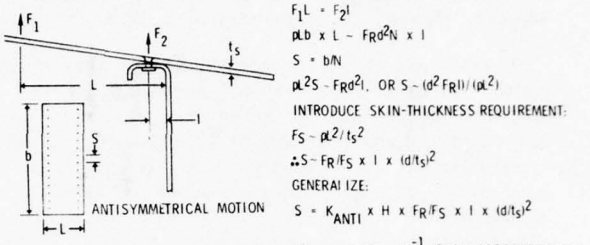

Figure 29. Derivation of fastener-strength relationship for antisymmetrical skin motion. F_R and F_S are fatigue strengths of the fastener and skin, respectively, p is the applied pressure, d is the fastener diameter, and N is the number of fasteners in the length b. The functional relationship for skin thickness is from Reference 3.

Concept for Laboratory Investigation

Figure 30 suggests in an idealized form a laboratory procedure that would be useful in filling this void in essential design information by confirming the validity of, or supporting revision to, the functional relationships exemplified by that of Figure 29 and by providing the constants of proportionality. This discussion is intended to emphasize the principles involved and the variables that require consideration. The procedure is cast in terms of skin and rib extended structure to provide a concrete example. Its key objective is to produce failures of fastener and skin (or fastener and rib, if desired) in sufficiently close load/time coincidence that, with small adjustments through use of a fatigue curve and use of stress versus pressure data from the test, they will reveal the re-

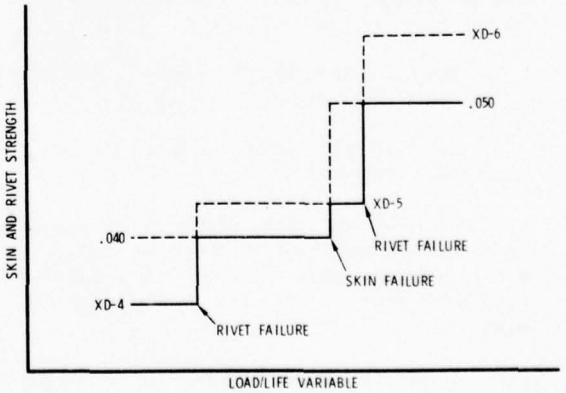

Figure 30. Idealized scheme for experimental support for fastener analyses. The objective is to produce fastener and component failures in sufficiently close load/life proximity that compatibility is established. In the example, 0.040 and 0.050 are standard aluminum sheet thicknesses in inches and XD-4, -5, and -6 are 2219-T81 aluminum alloy rivets of 4/32-, 5/32-, and 6/32-inch diameters.

quired conditions of compatibility between skin thickness and fastener strength. Thus, for a particular structural concept, the requirement for the fastener would depend only on its own properties, the geometry of the application, and the thickness of the skin, because that thickness is presumed to carry all necessary information about support spacing, load, curvature, and temperature.

Significant variables for the investigation could include support spacing, angle versus tee supports (and, thus, one versus two rows of fasteners), compatible versus rigid supports, skins chemically milled between supports or not, shear head versus tension head fasteners, and blind versus driven installations. Cost could be minimized through the use of specimens designed to be remanufacturable and through simultaneous loading of several specimens in a random-load facility. As suggested in Figure 30, the test might begin with rivets installed that were thought to be understrength (here symbolized by XD-4). Load would be applied in a series of increasing levels for perhaps 3 hours each until the rivets begin to fail. They then would be replaced by rivets of the next larger size (or greater strength). Loading in steps would proceed until the skin or the replacement fastener fails. That then would be replaced by the next size of skin or fastener. In this way, a combination of failures of rivets of two sizes (or strengths) and a skin, or vice versa, would provide information about the functional dependence and for the constant of proportionality.

The following list suggests, beyond the foregoing particularized example, those more general objectives that could influence and, unfortunately, sharply expand the test plan:

1. Determine the character of the rivet failure (e.g., shaft tension, head shear, head prying); a difference in functional dependence of fastener strength on diameter, between the square and the cube, is involved.

2. Determine the contributions of symmetrical and unsymmetrical motion.

3. Learn to what extent the K values are "universal" constants.

4. Find the equivalent strengths of important fasteners: aluminum rivets (shear and regular heads), bimetals, Huck bolts, Hi-Loks, and the blind fasteners: Jo-Bolts and Cherry locks and bulbs.

5. Determine the appropriate "1" values for tees and angles.

6. Evaluate the effects of skin splices and end bays.

7. Establish the utility of "progressive remanufacture" of specimens as a cost-control technique.

8. Repeat for or include substructure applications.

9. Repeat, in part, for other than skin and rib structure.

That there is a speculative tone to much of this discussion regarding fasteners reflects the state of knowledge in this aspect of design for acoustical fatigue prevention.

Concluding Observations

The primary objective of this paper is to exhibit some of the major characteristics of the design-support program for structural acoustics for the B-1. Emphasis has been placed on the approaches and techniques and on the points of view that led to them, with the anticipation that they may be found suggestive of methods applicable to future programs. To the extent that these techniques deviate from conventional practice, discussion may ensue that could prove useful.

As the contents of the paper suggest, there has existed a narrow focus in use of the results of analyses and tests toward airworthiness evaluations, the update of design requirements, and the support of weight- and cost-reduction efforts. Substantial quantities of information from analyses and measurements were generated in the program that have yet to be exploited; the engine-noise data for nonafterburner operations and for a single engine are examples. Had the production program continued, it would have provided the opportunity and funding for these investigations of less immediate applicability.

References

1. "Sonic Fatigue Design Guide for Military Aircraft," AFFDL-TR-74-112, Section 4.2.2, Air Force Flight Dynamics Laboratory, Wright-Patterson Air Force Base, Ohio, May 1975.

2. Belcher, P.M., et al., "Development of Aircraft Structure to Withstand Acoustic Loads," Aero/Space Engineering, Vol 18, No. 6, June 1959.

3. "Structural Design for Acoustic Fatigue," ASD-TDR-63-820, Air Force Flight Dynamics Laboratory, Wright-Patterson Air Force Base, Ohio, October 1963.

EXPERIMENTAL INVESTIGATION OF DYNAMIC CHARACTERISTICS OF TURBINE GENERATORS AND LOW-TUNED FOUNDATIONS

S. P. Ying and M. E. Forman
Gilbert/Commonwealth
Jackson, Michigan 49201

R. R. Drumm
Pennsylvania Power and Light Company
Allentown, Pennsylvania 18101

Two 820 MW turbine-generator (T-G) units with low-tuned concrete foundations were investigated experimentally during both startup and normal operating conditions. The dynamic response of the turbine generators and their foundation systems was characterized by resonance curves obtained during the startup transient and by vibration mode shapes at the normal operating condition. No severe resonance at the fundamental frequencies of the system was observed. The deflection or displacement of the foundation pedestal does not lead to unacceptable T-G vibration. The experimental results are compared and discussed with some previous theoretical studies.

INTRODUCTION

The definitions of the so-called "high-tuned" and "low-tuned" foundations for turbine-generators (T-G) are based on the fundamental frequency of the natural resonance of the system. This resonance is either higher or lower than the normal operating speed of the turbine generator. In particular, these resonant modes themselves refer to the elastic vibration of the turbine-generator and its foundation pedestal. They do not include the mode that relates to the vibration of the turbine-generator and its supporting structure as a body resulting from the softness of the foundation subsoil.

The traditional high-tuned foundations are constructed of large solid concrete blocks. The low-tuned foundations possess either steel [1,2] or concrete pedestal columns [3]. This paper discusses measured dynamic responses for two low-tuned concrete foundations designed and constructed for twin 820 MW turbine-generators.

Theoretically, the advantage of a low-tuned foundation lies in the reduction in bearing loads and forces which are transmitted to the sub-foundation and the supporting soil. A practical advantage is the additional free available space under and around the low-tuned foundation pedestal. The larger free available volume under the turbine-generator permits a more generous layout of piping and auxiliary equipment. Moreover, the cost of low-tuned foundations is less than that of high-tuned foundations [4].

Because of these technical, practical and economical advantages, low-tuned foundations are quite popular in Europe and have recently been introduced in several U.S. power plants. The T-G foundations in this investigation are the first two built in this country.

The foundations are part of Pennsylvania Power and Light Company's Martins Creek Station, Units 3 and 4. The two 820 MW oil-fired units are designed to operate at 1,000°F and 2,400 psi steam conditions. Unit 3 has been in commercial operation since October, 1975 with Unit 4 operating commercially since March, 1977. The plant is located along the Delaware River approximately 75 miles north of Philadelphia.

STEADY STATE OPERATION

The concrete foundation pedestals shown in Figure 1 were designed and built with large amounts of reinforcing steel. A program for the experimental investigation of the dynamic characteristics of the two 820 MW units was divided into two phases. The first phase consisted of dynamic measurement of the entire turbine generator and foundation pedestal during steady state operation for both units. Acceleration data provided the necessary information for vibration characterization.

The accelerations in orthogonal directions at each location were measured by accelerometers and recorded on individual channels of an FM tape recorder through charge amplifiers. This data acquisition system was calibrated in the field using a General Radio Model 1557-A vibration acceleration calibrator. The simultaneous use of multiple accelero-meters permitted inspection of several adjacent or distant points with equal ease. The data of a selected point, was recorded twice and each record contained at least two new data points. The repeated data point was used as a phase reference in time domain. Approximately 500 data points were collected during the two unit survey. Acceleration frequency spectra were obtained from the data stored on magnetic tape by utilizing a Fast Fourier Transform (FFT) analyzer (Nicolet Scientific Corporation, Model 660).

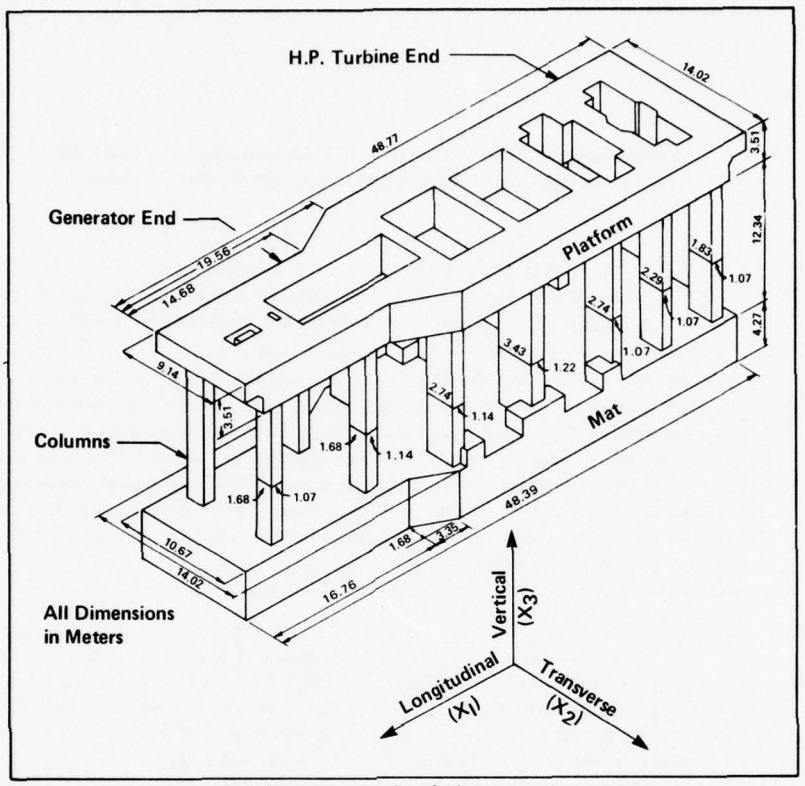

Figure 1. Low-tuned T-G foundation/pedestal (dimensions in meters).

Figure 2. Typical foundation pedestal acceleration during steady state, 800 MW (column 3 from high pressure turbine, height 7.2 m, direction X_2).

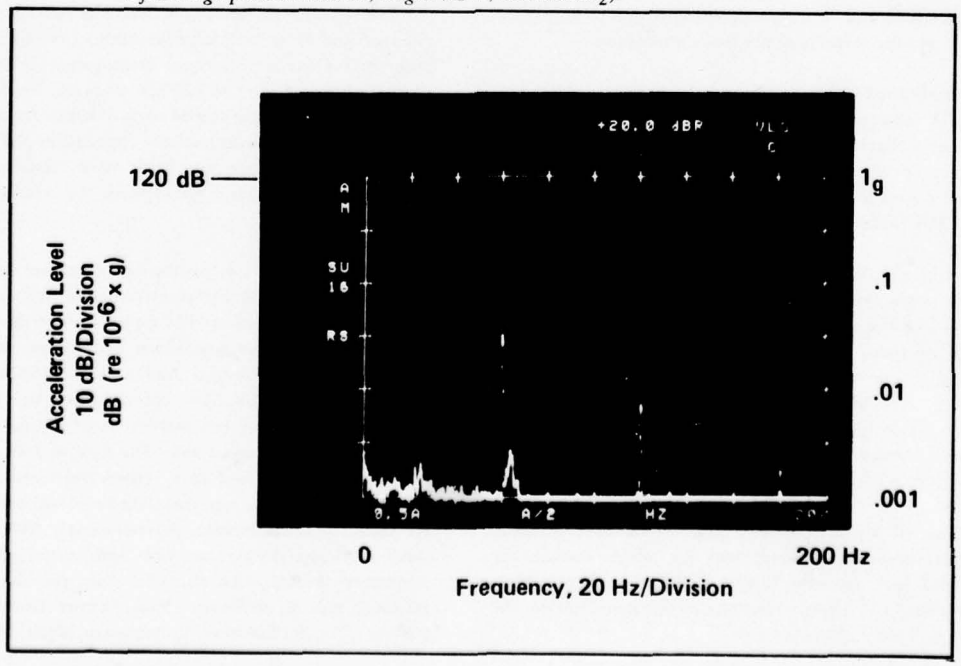

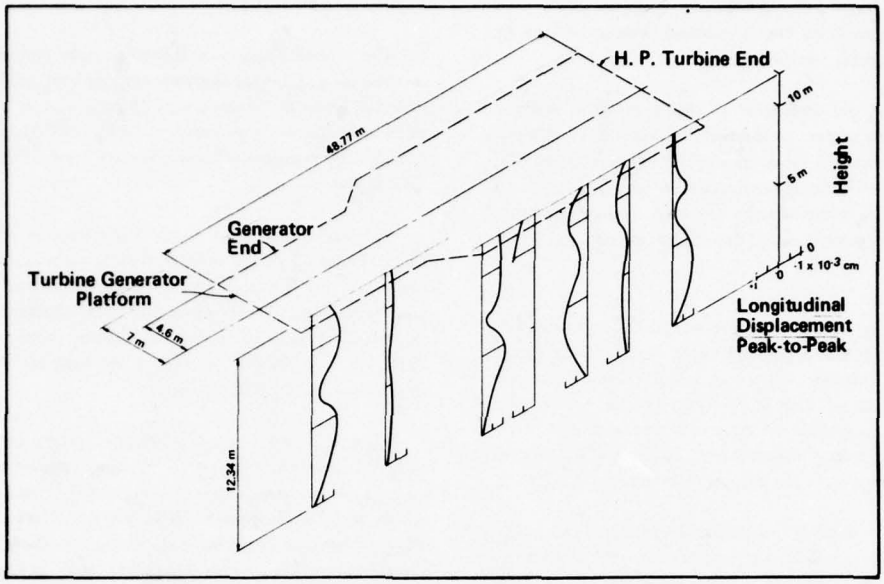

Figure 3A. Mode shapes for the steady state operation of a low tuned foundation pedestal at 60 Hz in the longitudinal (X_1) direction.

Acceleration data of the foundation pedestals for both units were investigated in the frequency domain. Figure 2 shows a typical spectrum of acceleration in decibels (dB) with a reference acceleration of 10^{-6} x gravitational acceleration (g). The dominant vibration frequency is 60 Hz, which was detected at most measurement positions. Oscillation phase relations in the time domain were studied by using two band-pass filters and a dual channel oscilloscope to determine the oscillation modes at the dominant frequency of 60 Hz, corresponding to the T-G speed of 3,600 rpm. The oscillation displacements were calculated by using the double integration in Nicolet 660 from the recorded accelerations on each pedestal column and the platform in each direction. Then, the displacements were plotted as a function of distance.

Figure 3B. Mode shapes for the steady state operation of a low tuned foundation pedestal at 60 Hz in the transverse (X_2) and vertical (X_3) directions (X_3 magnitude only).

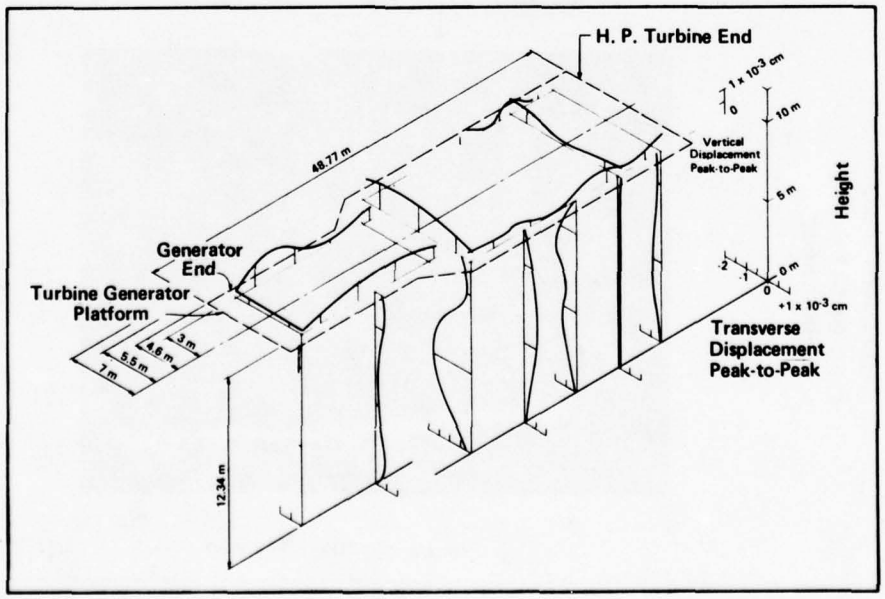

These standing waveforms represent a mode of the forced oscillation resulting from the centrifugal force generated by the rotor of the turbine-generator.

Theoretically, the oscillation of the foundation pedestal is symmetric with respect to the turbine axis. Figures 3A and 3B depict the vibration mode in orthogonal directions, X_1, X_2, and X_3 (see Figure 1), at one side of the T-G axis of a unit. The standing waves on the other side and on the other unit are similar; nevertheless, the magnitudes may vary as much as 6 dB.

Most of the spectra obtained from the T-G bearings also show a peak at 60 Hz. A primary cause of the 60 Hz forced vibration is the imbalance of the rotating system. Figure 4 is a typical spectrum of such a vibration. The data were compared with the acceptable criterion for general machinery – commercial [5]. Most of the measured dynamic displacements of the T-G bearings meet the maximum criterion.

On the other hand, a mis-aligned coupling, which might result from the foundation, can generate harmonics at 120 Hz (see Figure 5). However, most 120 Hz components in the frequency spectra were found to be negligible, and all vibrations possibly caused by the misalignment satisfied the maximum acceptable limit. Finally, observed frequency components at 30 Hz, a subharmonic frequency of the T-G running speed, resulted from self-excited vibrations because of boundary conditions at the bearing or its related steel elements.

STARTUP TRANSIENT

The second phase of this investigation included the continuous monitoring of the turbine-generator and foundation-pedestal at selected locations during a cold startup of a turbine-generator from zero to 3,600 rpm. These data were used for the transient vibration investigation of the low-tuned foundation.

The accelerations on a turbine-generator and its foundation-pedestal during cold startup were measured at seven locations, which were selected based on the steady state data, and continuously recorded on individual channels of FM tape recorders. Frequency spectra of dynamic accelerations were obtained from the data stored on magnetic tapes by utilizing the narrow band FFT analyzer.

Figures 6 and 7 are acceleration spectra measured at a pedestal column and a T-G bearing, respectively, during startup. As shown in the spectra, the first mode oscillation frequency of each spectrum is the T-G speed below 3,600 rpm. In contrast, the first mode oscillation in those spectra obtained during steady state operation (such as those shown in Figures 2, 4, and 5) is 60 Hz, its harmonics or its sub-harmonics.

Dynamic displacements of the first mode oscillations at the monitoring positions were calculated from their accelerations. The first mode displacements are plotted vs. frequency (T-G speed) for each position (except the front bearing of the high pressure (HP) turbine) during startup in Figures 8 and 9.

Figure 4. Typical bearing acceleration during steady state, 800 MW (generator rear bearing, direction X_2).

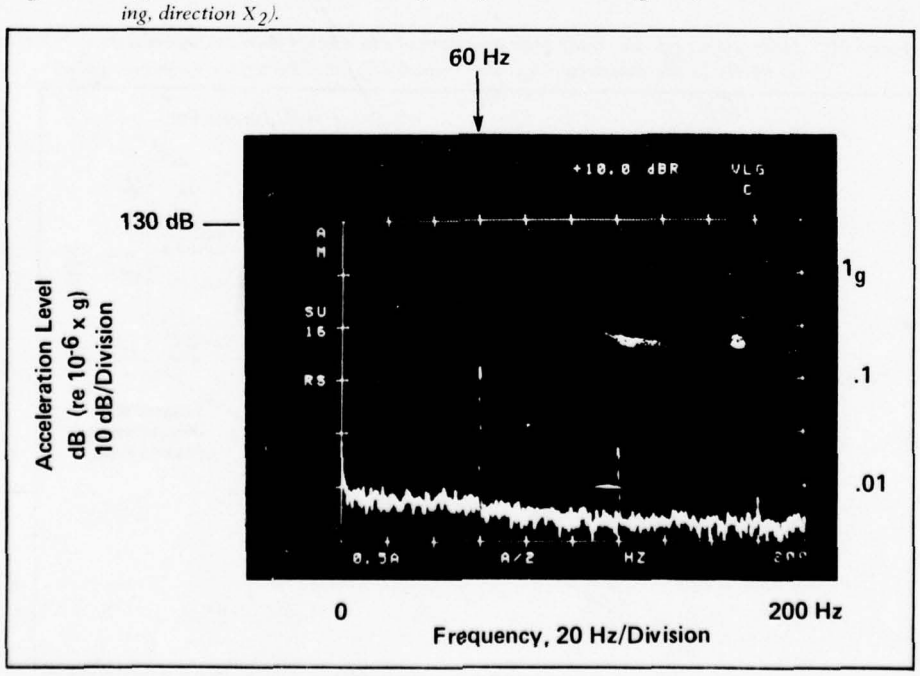

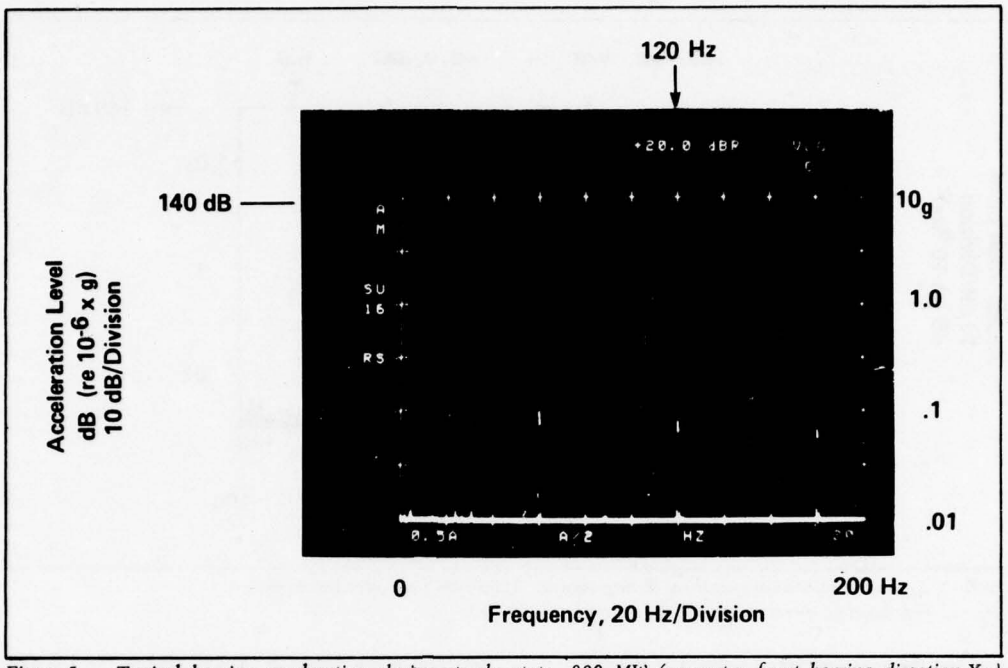

Figure 5. Typical bearing acceleration during steady state, 800 MW (generator front bearing, direction X_2).

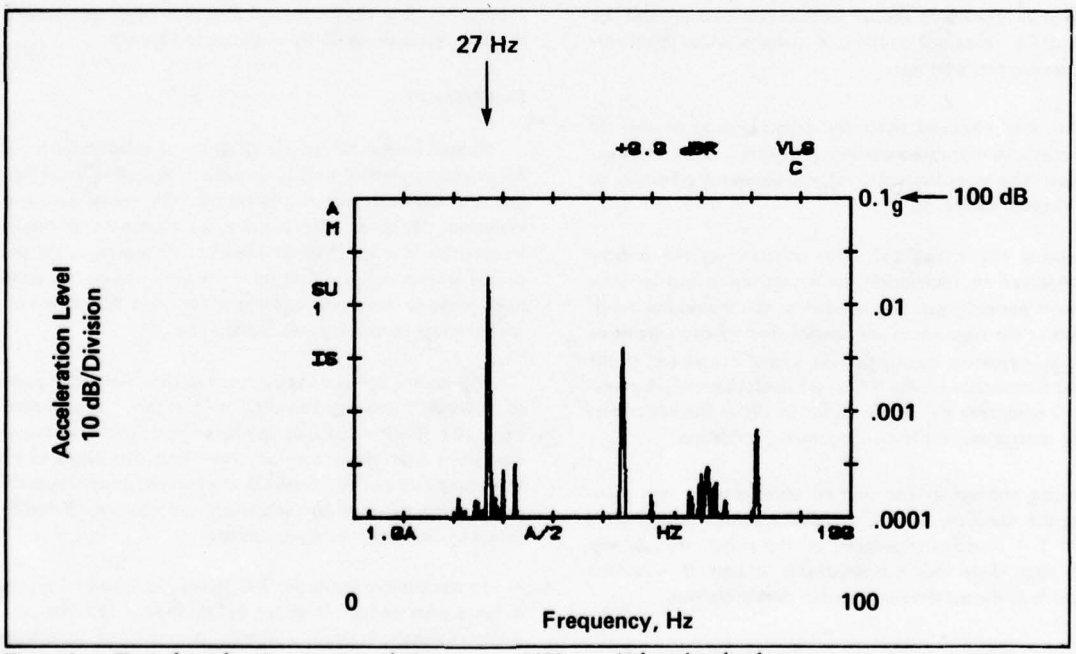

Figure 6. Typical acceleration spectrum during startup, 1620 rpm (6th pedestal column 9.6 m high, direction X_1, first peak frequency 27 Hz).

These graphs represent resonant curves at five locations. The three curves in Figure 8 are the resonant curves detected at the rear bearing of the low pressure (LP) turbine, and the front and rear bearings of the generator.

The data in Figure 9 were obtained from the fifth and sixth columns counted from the HP turbine end, approximately 9.6 m (31.5 ft) above the mat. The LP turbine rear bearing and the generator front bearing are at the top of the

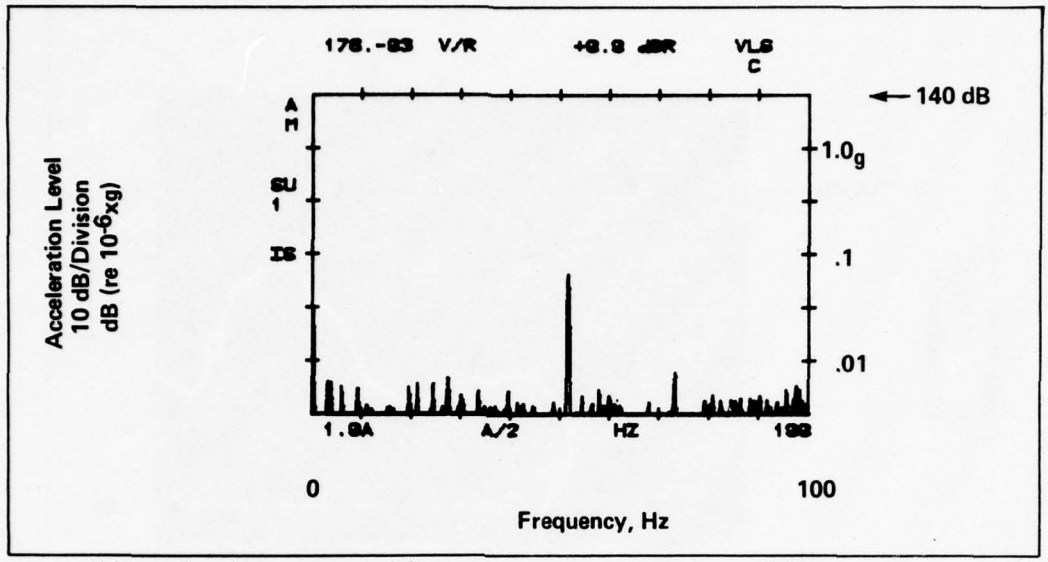

Figure 7. Typical acceleration spectrum during startup, 3105 rpm (low pressure turbine rear bearing, direction X_2, peak frequency 51.75 Hz).

fifth column, and the generator rear bearing is at the top of the sixth column. The peak near 40 Hz detected on the fifth column also appears on the LP turbine rear bearing, and the peak at 27 Hz obtained on the sixth column is also shown on the generator rear bearing.

The data obtained from the front bearing of the HP turbine in a vertical direction do not explicitly show resonant behavior. The vibration accelerations increased gradually as the T-G speed increased.

Because the centrifugal force exerted on the turbine generator and its foundation during startup is smaller than that at a normal operating condition, the maximum accelerations at the resonances are smaller than or comparable to those at operating condition. No severe resonance at the natural frequencies of the T-G and foundation was observed. Table I compares the accelerations in dB at the resonances during startup and at a normal operating condition.

During startup of the unit an accelerometer was monitoring the vibration at the fifth column, same height (9.6m), of the T-G foundation-pedestal of the other unit. It was found that there was no noticeable change in vibration amplitude at the monitoring location during startup.

A more detailed study was conducted for a monitoring position on the sixth column (from the HP turbine end) of the startup unit. In addition to the first mode data, the second and third mode data were also analyzed and plotted in Figure 10. As shown in the figure, the resonance frequencies of the first three modes are 27 Hz, 51 Hz and 70 Hz. There is no resonance at or near 60 Hz. All these modes were detected in the direction (X_1) parallel to the T-G axis. The resonance frequency of another vibration mode detected on column No. 5 in the horizontal direction (X_2), transverse to the T-G axis is about 40 Hz as shown in Figure 9.

DISCUSSION

Natural frequencies of a large structure calculated from an Eigenvalue equation usually involve frequencies from very low to very high values, associated with many modes of vibration. However, the number of dominant resonance frequencies is quite limited. The data presented in the preceding section indicate that there are only one or two dominant peaks in each resonant curve for these 820 MW units with the low-tuned concrete foundations.

Wilson and Brebbia have estimated the dynamic response of 500 MW turbine-generators with low-tuned steel foundations [2]. Their calculated results of vertical displacements also show that there are only two dominant peaks in the frequency domain. Although the experiment described in this paper is not the same as their work, the resonance behaviors found by the two groups are similar.

In considering the entire T-G foundation-pedestal system, a reasonable model is proposed in Figure 11. The rotor pedestal, which includes a bearing pedestal and foundation column, and foundation are viewed as a series of masses connected by either viscous or elastic sections. The damping effects should be taken into account. Crook and Grantham used a similar model to predict the dynamic response of a 375 MW T-G with a steel low-tuned foundation by the Prohl-Myklestad method [1]. They found that the resonance

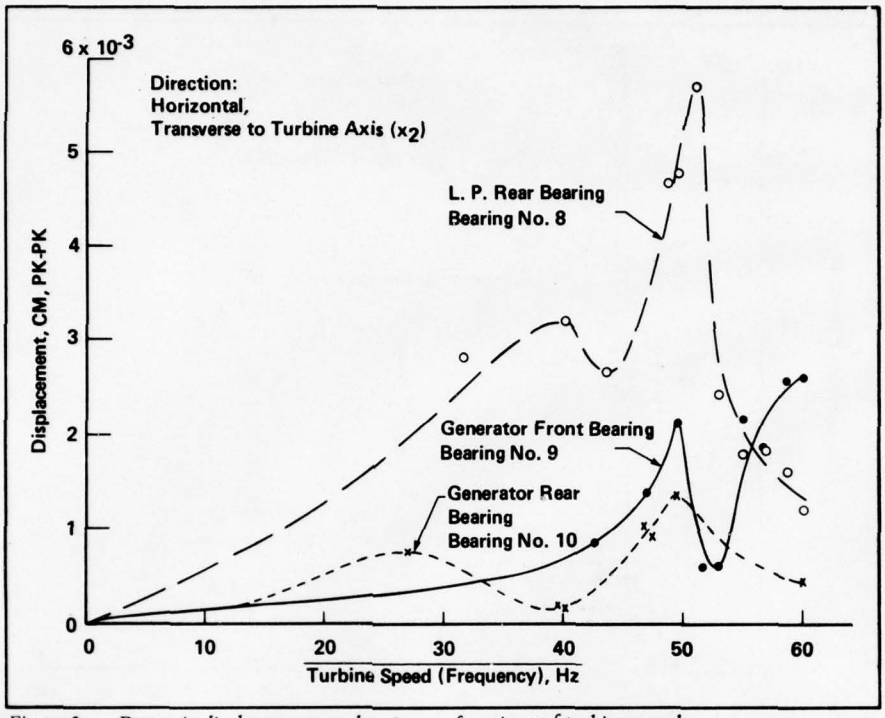

Figure 8. Dynamic displacements on bearings as functions of turbine speeds.

Figure 9. Dynamic displacements on columns as functions of turbine speeds.

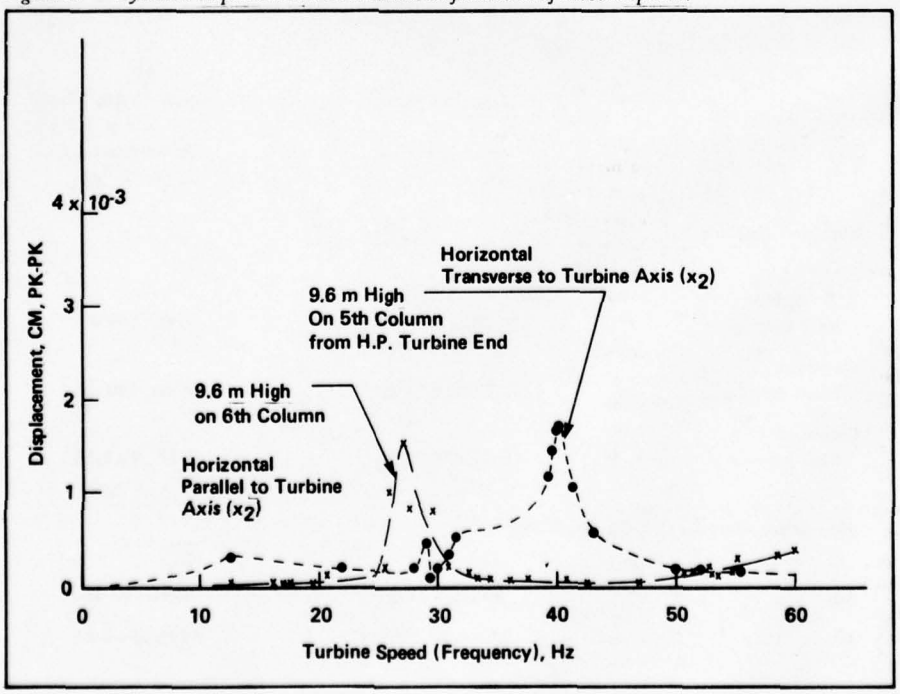

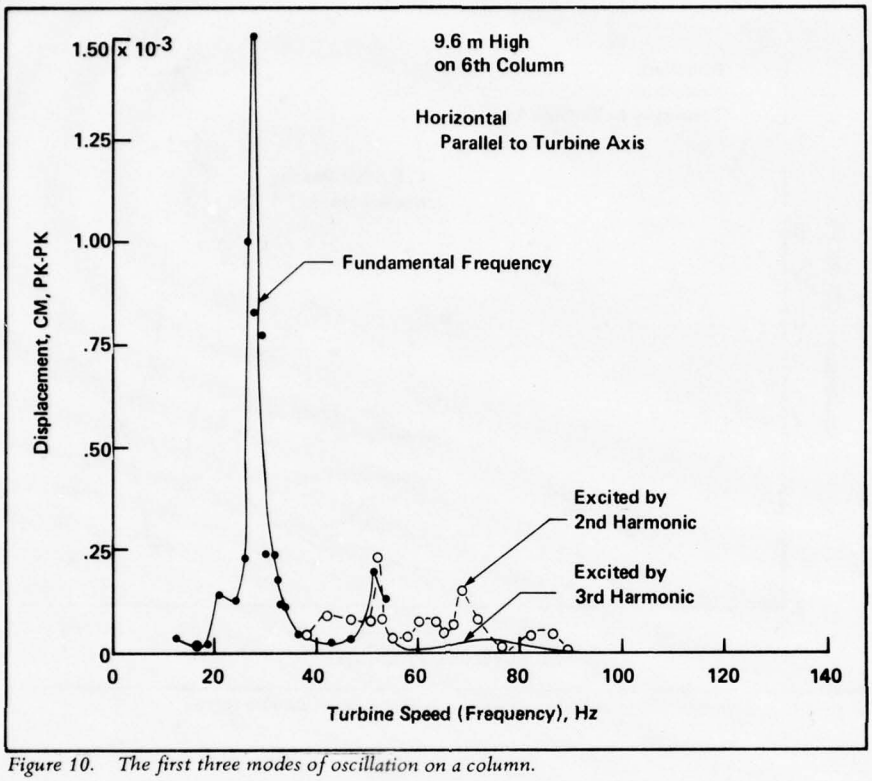

Figure 10. The first three modes of oscillation on a column.

TABLE I

	Acceleration at Peak Startup Test dB (re 10^{-6}g)	Steady State Test Acceleration dB (re 10^{-6}g)
Turbine-Generator		
L. P. Turbine Rear Bearing	51 Hz, 106.6 dB	60 Hz, 107 dB
Generator Front Bearing	49.5 Hz, 97.3 dB	60 Hz, 100 dB
Generator Rear Bearing	49.5 Hz, 95.2 dB	60 Hz, 97.2 dB
Foundation-Pedestal Column, 9.6 M High		
5th	40 Hz, 92 dB	60 Hz, 92 dB
6th	27 Hz, 84.2 dB	60 Hz, 84.5 dB

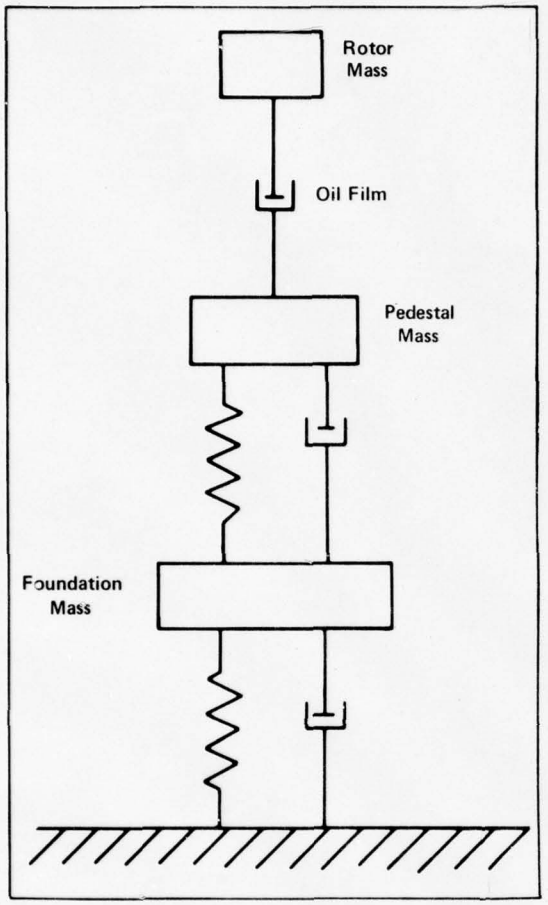

Figure 11. Theoretical model of T-G and its low-tuned foundation.

at the journals is slightly less than 3,000 rpm.

The experimental results obtained in this investigation are similar. However, Crook and Grantham's calculated vibration amplitudes are much higher than those in this paper because they neglected the damping within the pedestals. The numerical values for the various parameters contained in the proposed model in Figure 11, except the damping coefficient of the pedestal, can be found from Reference 1.

Wilson and Brebbia also calculated the mode shape for the case of free vibration by the finite element method. The calculated mode shapes are consistent with the experimental results shown in Figure 3 of this paper.

CONCLUSIONS

At steady state, only the T-G bearing vibration at the harmonics of 120 Hz, resulting from a misaligned coupling, might relate to the deflection or displacement of the foundation pedestal. However, most 120 Hz components in the frequency spectra detected at the T-G bearings are negligible. The deflection or displacement of the foundation pedestal does not lead to unacceptable T-G vibration.

No severe resonance at the natural frequencies of the T-G and its foundation system was observed during startup. The maximum accelerations at the resonances are smaller than or comparable to those at a normal operating condition. The resonance peaks detected at the different locations occur at 27 Hz, 40 Hz, 51 Hz and 70 Hz. There is no peak at or near 60 Hz (3,600 rpm).

Furthermore, there was no noticeable change in vibration amplitudes at a normally operating unit during the startup of the other unit.

Based on the above observed results, it can be concluded that the low-tuned concrete foundations for these large turbine-generators provide fully satisfactory performance.

The vibration mode shapes of the foundation pedestals during a steady state, and the resonance frequencies of the T-G and its supporting structure system obtained in this experiment, are consistent with the previous theoretical studies.

ACKNOWLEDGEMENT

The authors wish to express their appreciation to Dr. H. G. Pfeiffer of Pennsylvania Power and Light Company for making this program possible. They also thank R. F. Visbisky and E. E. Dennison of Gilbert/Commonwealth for their comments and R. A. Putnam and R. D. Beatty for their assistance with data collection.

REFERENCES

1. A. W. Crook and F. Granlham, "An Approach to the Prediction of the Vibrations of Turbine Generators on Undertuned Foundations", Paper No. 67-VIBR-46, the ASME Vibration Conference, Boston, Mass., March 29-31, 1967.
2. R. R. Wilson and C. A. Brebbia, "Dynamic Behavior of Steel Foundations for Turbo-Alternators", J. Sound & Vibration, 18(3), 405 (1971).
3. D. K. Croneberger and K. R. Broome, "Low-Tuned Foundations for Large Turbine-Generators", Power Engineering, June 1973, pp. 34-37.
4. H. Lorenz and H. Dietz, "Steel Pedestals Compared to Concrete Foundations For Large Steam Turbine Generators", Proceeding of the 32nd Annual Meeting of the American Power Conference, Chicago, Illinois, April 21-23, 1970.
5. ISO Standard 2372, "Mechanical Vibration of Machines with Operating Speeds from 10 to 200 Rev./Sec. – Basis for Specifying Evaluation Standards", 1974.

COMBINED VIBRATION/TEMPERATURE/SIDELOAD ENVIRONMENTAL TESTING OF UHF BLADE ANTENNAS

Ronald Volker
McDonnell Douglas Corporation
McDonnell Aircraft Company

Service problems encountered on the F-4 aircraft showed that the environmental qualification requirements for the UHF blade antenna were not adequate. Although the individual environmental levels were stringent enough, only combined environmental testing could duplicate the conditions in which service problems occurred. Techniques for applying static side load simultaneously with vibration and temperature were developed. The combined environment testing was instrumental in the rapid assessment of antenna modifications and resulted in a final configuration which proved satisfactory in service. A need to include combined environmental testing for qualification of blade antennas was established.

INTRODUCTION

The UHF communication blade antenna on the F-4 and other high performance aircraft has encountered periodic environmental problems over the years. The antenna is cantilevered from the aircraft moldline into the airstream.

Difficulties on the F-4 were uncovered during vibration testing in 1964 and 1969. Again in 1974, an antenna incorporating electrical and producibility improvements failed during vibration qualification. Flight vibration and airload (i.e. sideload) measurements were made. These verified the test levels. Supplemental high frequency vibration levels were also established. By early 1975, an antenna redesign with a tungsten powder damper passed all requirements and was incorporated on the F-4.

However, in late 1979, complaints were received from the service that the antenna was developing cracks and some users considered it unsatisfactory for flight usage.

The structure of the antenna is shown in Figure 1. It consists of two pieces of aluminum separated by a dielectric insert at approximately mid-span. Structural integrity is provided by a steel pin with a tension preload, and the outer surface is covered with a polyurethane rain erosion coating. The cantilevered assembly is mounted through the base to the aircraft moldline.

The service failures consisted of cracks in the rain erosion coating at the lower dielectric-aluminum interface (Figure 1, Item 11). Disassembly of a returned antenna showed the dielectric insert to be disbonded and cracked completely across the interface.

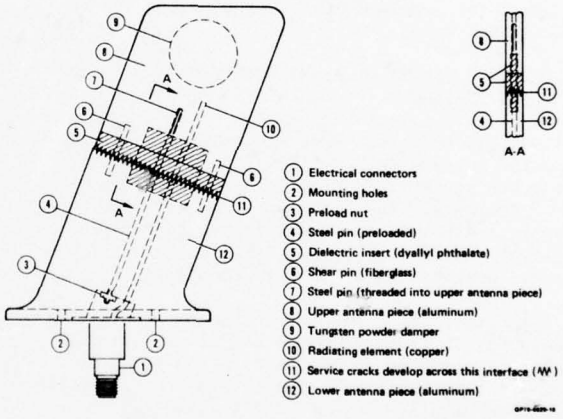

Fig. 1 Sketch of UHF Antenna

The service complaints resulted in a new investigation. Tests on production antennas showed them capable of meeting all individual qualification requirements. Since the individual environments had been previously verified by flight data, it was concluded that the service problems had to be caused by combined environments.

Examination of the antenna construction shows that a loss of preload, or sufficient moment to overcome the preload, would result in gapping, because of the insert-aluminum interface has little or no tensile continuity. Since dielectric materials are relatively weak in bending, gapping would also account for the cracks in the dielectric insert and the erosion coating.

The primary environments causing moment at the insert are vibration and static side load. The combination of the two could result in loads which exceed the preload along the face of the insert. Since the preload and mechanical properties of the dielectric are also affected by temperature all three environments were considered important for combined testing.

Test techniques were developed for simultaneous application of side load with vibration and temperature. These combined environmental tests were successful in reproducing the type of cracks reported in service.

Subsequently, a modified antenna was developed which passed all individual and combined environmental tests. The modified antenna was approved for production and retrofit and has provided satisfactory service to date.

The dynamic and combined environment portions of the antenna test program including the development of an improved side load method for combined environment testing, are presented below.

REVIEW OF FLIGHT DATA AND QUALIFICATION VERIFICATION TESTING

Flight test data were obtained on an instrumented antenna in late 1974 to aid in evaluating the vibration and airload qualification requirements. Data were obtained at representative F-4 flight conditions and maneuvers. Flight side loads were well below the specified test levels as were the vibration data.

A composite of the reduced accelerometer data for the lateral direction at the antenna base is compared in Figure 2 to the qualification test spectrum. The flight data were reduced with 1/3 octave band techniques. Probability density analyses were performed on each 1/3 octave filtered time history to obtain a crest factor which was used to convert the rms acceleration level to a sinusoid at the center frequency of each 1/3 octave band. The flight data are well below the qualification test spectrum at all frequencies. The flight data show peaks at 12 and 125 Hz and several above 500 Hz. These were easily predictable. The 12 Hz peak is due to fuselage lateral bending. The 125 Hz peak is the first lateral bending mode of the antenna, which has a somewhat lower frequency than the cantilevered bending mode due to the root flexibility provided by the aircraft structure. The higher frequency peaks are associated with higher modes of the antenna.

Similar flight vibration data obtained at the antenna mid-span and tip were also well below the comparable laboratory responses.

Due to the in-service problems, however, it was decided to verify that production antennas would still meet qualification test requirements. An antenna was taken from stores and subjected to all individual environments including vibration at ambient and elevated (127°C) temperatures, shock (15g, 11 millisecond, half-sine) and static side loading to 5.512×10^4 newtons per square meter (8 psi). The antenna successfully completed all testing with no structural or electrical failures. It was evident therefore that the individual flight environments did not produce the flight problems.

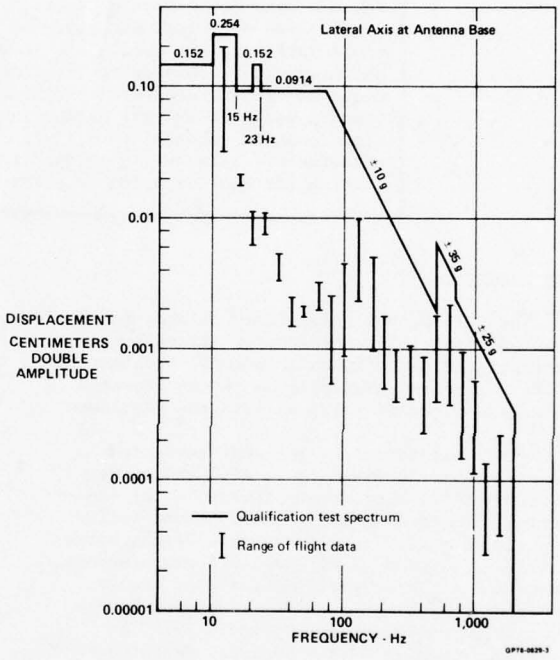

Fig. 2 Comparison of Flight Data and Qualification Test Spectrum

ANTENNA VIBRATION CHARACTERISTICS

Tests were performed on antennas to obtain response characteristics and mode shapes to aid in determining the vibration modes relevant to the flight failures. A typical cantilevered antenna frequency response plot of tip transmissibility is shown in Figure 3 for the lateral axis.

The associated lateral vibration modes are presented in Figure 4. The first mode is easily identified as cantilevered bending, whereas the remaining three are primarily associated with tip motion. From the response and mode shape data, it appeared that the predominant mode involving high moments in the area of flight failures was the first lateral bending mode.

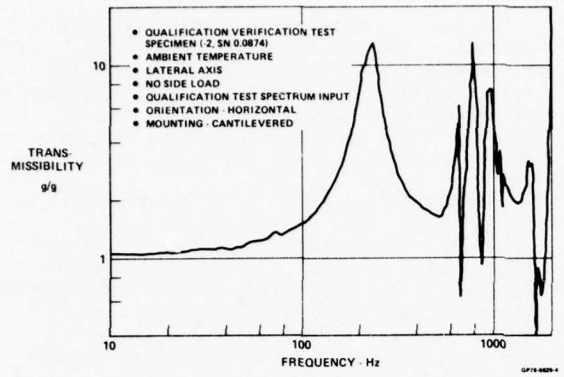

Fig. 3 Antenna Tip Transmissibility vs Frequency

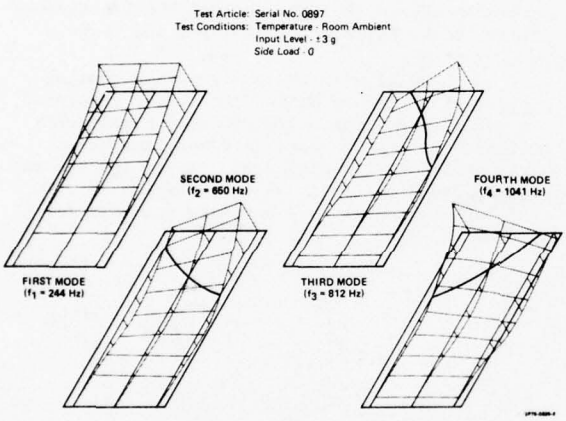

Fig. 4 Antenna Mode Shapes

In order to further assess which modes were important, vibration responses of a cracked antenna returned from service were compared with those of an undamaged antenna, using side loads of 0, 44.5 and 89 newtons. The results at the qualification vibration levels are presented in Table 1.

The data showed no significant difference without the side load. However, the addition of side load had a dramatic effect on the first bending mode frequency of the cracked antenna, dropping it from 235 to 80 Hz, while the new antenna frequencies dropped only slightly. The higher mode resonances were changed only slightly by side load.

An examination of the first bending mode shapes showed evidence of gapping in the cracked antenna under combined load as shown in Figure 5. For the no load case, the mode shapes and frequencies are quite similar while for the sideload case, there is a distinct break in curvature in the region of the dielectric insert for the cracked antenna. This indicates gapping and a loss of stiffness across the joint, resulting in a reduced frequency.

These data tended to confirm a failure mechanism associated with a combination of the fundamental lateral bending mode and side loading.

Table 1 Comparison of Lateral Resonant Frequencies of New and Cracked Antennas

TIP SIDE LOAD (N)	INPUT VIBRATION (±g)	RESONANT FREQUENCIES (Hz)	
		NEW ANTENNA	FAILED ANTENNA
0	10	250	235
	35	650	630
	25	830	790
	25	1040	1010
	25	1800-1950	1700-1800
44.5 (10 LB)	10	260	116
	35	–	630
	25	800-820	730
	25	1000-1050	920
	25	1700-1950	1590
89 (20 LB)	10	240	80-90
	35	–	630
	25	810	710
	25	1020	870
	25	1750	1580

GP78-0829-10

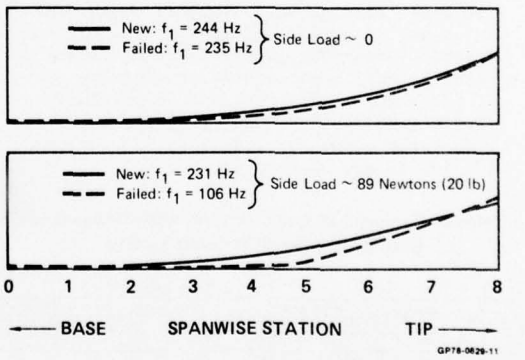

GP78-0829-11

Fig. 5 First Mode Comparison of New and Cracked Antennas with and without Side Load

COMBINED ENVIRONMENT TESTING

In order to duplicate the flight failures, a new antenna was subjected to combined vibration, side load, and temperature environments. A soft spring system was used to apply side loading.

A schematic of the test setup is shown in Figure 6. The uniform pressure was correlated with tip loading by equating moments at the lower center of the dielectric insert.

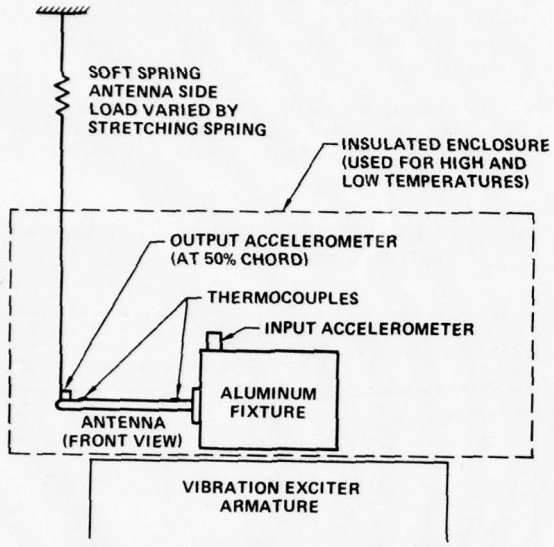

Note: Sideload applied at 50% chord and approximately 0.41 cm (0.16 in.) inboard from tip.

GP78-0829-8

Fig. 6 Schematic of Combined Environment Test Setup Using a Soft Spring for Tip Side Loading

The test parameters were based on the maximum ranges anticipated during flight for the F-4. Testing was performed on several antennas, as summarized in Table 2. It consisted of resonant dwells for the critical first lateral bending mode at vibration levels of ±3, 5 and 10 g's; at room temperature, 93.3°C (200°F), and -40°C (-40°F); with tip side loads of 0, 44.5, 89, and 133 newtons (0, 10, 20 and 30 pounds).

Table 2 Summary of Combined Vibration/Temperature/Side Load Supplemental Antenna Testing

TEMP (°C)	TIP SIDE LOAD (N)	INPUT VIB LEVEL (±g)	TEST TIME (MIN)	SERIAL NO. 0897 FUNDAMENTAL MODAL FREQ (Hz)	SERIAL NO. 0897 TIP TRANSMISSIBILITY (g/g)	SERIAL NO. 1111 FUNDAMENTAL MODAL FREQ (Hz)	SERIAL NO. 1111 TIP TRANSMISSIBILITY (g/g)	SERIAL NO. 1247 FUNDAMENTAL MODAL FREQ (Hz)	SERIAL NO. 1247 TIP TRANSMISSIBILITY (g/g)
ROOM	0	3	2.5	NOT DONE	NOT DONE	234	5.0	201	6.1
		5	↓	NOT DONE	NOT DONE	257-253	8.0-10.0	199	4.8
		10		231	6.3	258	7.1	241	5.5
	44.5 (10 LB)	3		NOT DONE	NOT DONE	150	5.8	157	4.0
		5		NOT DONE	NOT DONE	148	5.0	152	4.1
		10		158	4.4	134	4.3	128	4.4
	89 (20 LB)	3		NOT DONE	NOT DONE	155	6.5	139	5.4
		5		NOT DONE	NOT DONE	156	6.7	137	4.0
		10		125	4.6	114	4.8	102	4.5
93.3 (200°F)	0	3		195	5.4	194	4.2	200	3.8
		5		229	10.0	190	7.5	204	8.6
		10		237	8.4	189	5.2	217	5.6
	44.5	3		122	7.5	90 ⚠	4.4	87-63 ⚠	3.2
		5		120	3.8	82	5.2	57	3.2
		10		140	4.2	74	5.5	53	2.7
	89	3		130	4.0	85	4.3	82-61	4.2
		5		129	4.3	79	6.0	77	4.8
		10	↓	108-97 ⚠	3.3	86-62 ⚠	8.4 ⚠	75	5.3 ⚠
-40 (-40°F)	0	3	3.0	204	4.2				
		5		209	8.0				
		10		238	5.7				
	44.5	3		148	3.8				
		5		156	5.2				
		10		150	3.4				
	89	3		153	5.2				
		5		152-150	5.0				
		10		137-135	3.4-6.2				
	133 (30 LB)	3	↑	101	2.2				
		5	3.0	102	2.0				
		10	10.0	96-59 ⚠	3.0-7.5 ⚠				

Notes: ⚠ Resonant frequency decreased during dwell.
⚠ Rain erosion coating cracked.
⚠ Resonant frequency lower than expected based on S/N 0897 results. May indicate some structural change just prior to this time.
⚠ Bolt broke, dielectric insert cracked, and antenna separated into two pieces.

In general, there was a significant drop in frequency with increasing side load at all temperatures. (Apparent inconsistencies in this trend were attributed to coupling between the soft spring side load setup and the antenna.) These frequency reductions are indicative of gapping at the dielectric insert.

During the final test point for the first antenna, there was a significant drop in resonant frequency during the dwell, indicating probable failure. Post test examination revealed cracks in the polyurethane coating and the dielectric insert similar to those found in the returned service antenna. The second and third antennas both failed during the last portion of the high temperature testing, and in both cases the steel preload pin broke.

Tests were also conducted to evaluate the effects of increasing the pin preload. The results showed that this helped but the dielectric insert still cracked during the tests.

In parallel with the analysis and testing being conducted by MCAIR, the vendor developed a modified antenna which provided significant structural improvement. A fiberglass strap was bonded to the dielectric insert and the antenna base and tip as shown in Figure 7. Two of these antennas were provided to MCAIR for test.

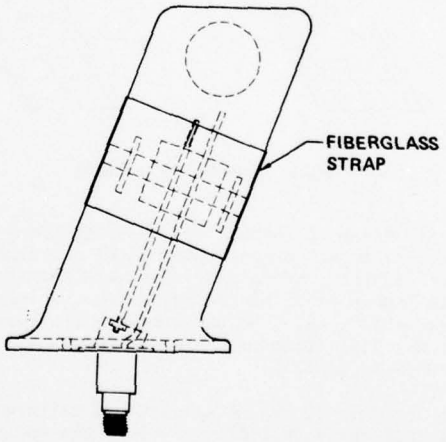

GP78-0829-6

Fig. 7 Sketch of Modified Antenna Showing Fiberglass Strap

The first antenna was subjected to the vibration qualification test spectrum and to supplemental high frequency testing in the lateral axis. The fundamental lateral bending mode was found to be approximately 240 Hz. Shock and static side load tests were also performed. The antenna passed these tests without any structural or electrical degradation.

The second antenna was subjected to combined vibration/temperature/sideload testing similar to that applied to the unmodified Serial No. 0897 antenna in Table 2. It exhibited stable fundamental mode frequency characteristics with side load at all temperatures, although mechanical coupling with the side load spring system continued to be a problem.

Additional combined testing was performed at high temperature (93.3°C) with tip side loads of 133 newtons in an attempt to test the antenna to failure. The vibration exciter system being used was nearing its maximum capability of 35 g's (at 244 Hz) when the test setup was damaged and testing was discontinued. There was still no structural or electrical damage to the antenna.

The structural integrity of the modified antenna was verified by the tests performed including combined environmental levels which equal or exceed those anticipated on the aircraft and which caused catastrophic failure of the unmodified version of the antenna. This modified version has been in use on the F-4 without field problems for more than two years.

DEVELOPMENT OF AN IMPROVED SIDE LOADING SETUP FOR COMBINED ENVIRONMENT TESTING

As mentioned above, numerous problems were encountered with the soft spring loading system in the test setup. Mechanical coupling and damping response effects made it difficult to interpret test response changes. Also, desired bending moments and shears could only be approximately matched, and test efficiency was poor due to the need for frequent loading system adjustments, especially when the access was required to the thermal enclosure which then had to be restabilized.

Several different types of springs and attachments were tried. Although improvements were made, the coupling effects and damping problems persisted. Therefore, another means was needed for applying side load.

The system decided upon was compressed air. A sealed air cavity was constructed beneath the antenna, with a small air gap around the edges of the blade. Compressed air was introduced into the cavity at a rate faster than it could leak out around the gap between the blade and the fixture. By regulating the flow rate, it was possible to hold a uniform overpressure on one side of the antenna. Static pressures up to 5.512×10^4 newtons per square meter (8 psi) were easily obtained and even higher pressures could be obtained if desired. It was also found that high or low temperatures can be obtained rather quickly by preheating or precooling the inlet air supply.

This system is shown in Figure 8. The template on the top of the cavity can be cut to fit various antenna shapes and to control the air gap, which was approximately 0.025 to 0.050 centimeters (0.010 to 0.020 in.) for the UHF antenna configurations tested.

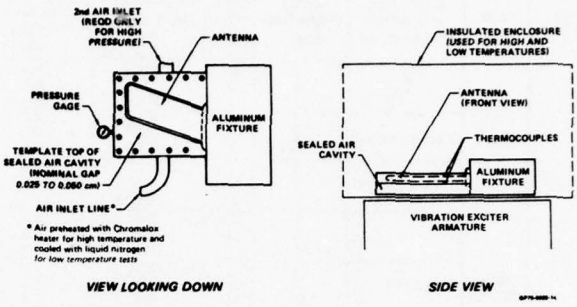

Fig. 8 Combined Environment Test Setup Using Compressed Air for Side Loading

Frequency response data were obtained on an antenna to evaluate the test setup. The side loading was conducted in the same test setup at room temperature, both with the soft spring tip side load mechanism and the compressed air system.

The no load baseline, and representative equivalent tip, and uniform pressure side loading responses are presented in Figure 9. As shown, the fundamental mode responses using the air loading are cleaner and have less damping (i.e. higher amplitude response). The higher mode responses are similar with either loading system.

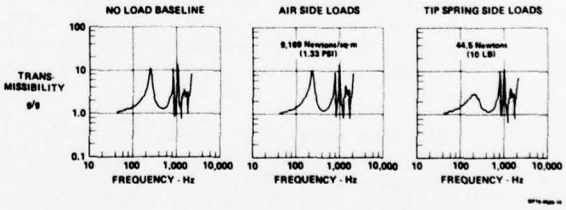

Fig. 9 Frequency Response Comparison with Spring and Air Side Load

In order to fully check out the setup, a new unmodified antenna was tested in the combined environment compressed air fixture. Results are summarized in Table 3. The antenna lasted somewhat longer than previously tested unmodified antennas; however, the pin broke and the dielectric insert was completely severed at the 2.756×10^4 newtons per square meter (4.0 psi) side load, 93.3°C (200°F) test point while peaking for the 10g resonance dwell.

Table 3 Summary of Combined Testing on Original Antenna with Compressed Air

TEMP (°C)	SIDE LOAD PRESSURE (Newton/sq-m)	INPUT VIBRATION (±g)	TEST TIME (MIN)	FUNDAMENTAL MODE DWELLS	
				FREQUENCY (Hz)	TIP TRANSMISSIBILITY (g/g)
ROOM	0	3	2.5	216	9.3
		5		217	9.0
		10		216	9.3
	9,169 (1.33 PSI)	3		216	8.7
		5		218	8.5
		10		218	9.1
	18,407 (2.67 PSI)	3		212	8.5
		5		212	8.7
		10	2.5	212	8.6
93.3 (200°F)	0	3	2.5	197	8.3
		5		194	8.2
		10		197	8.0
	9,169	3		191	7.6
		5		194	7.6
		10		191	7.1
	18,407	3		154	7.3
		5		153	6.9
		10	2.5	149	6.6
−40 (−40°F)	0	3	3.0	218	8.6
		5		220	9.1
		10		213	9.5
	9,169	3		215	10.0
		5		210	8.5
		10		205	8.2
	18,407	3		203	8.0
		5		208	8.0
		10		209	7.8
	27,576 (4.00 PSI)	3		208	6.0
		5		211	6.5
		10	3.0	203	8.0
ROOM	27,576	3	2.5	170	8.5
		5	2.5	172	8.0
		10	2.5	165	7.5
93.3 (200°F)	27,576	3	2.5	126	12
		5	2.5	121-126	10-11
		10	*	-	-

*Antenna failed while peaking at 10 g; pin broke, dielectric severed at lower interface with aluminum and antenna separated into two pieces.

GP78-0829-16

The trend of decreasing resonant frequency with increasing side load, typical of this type of antenna, is evident in the data, although the percentage drop isn't quite as large as for antennas tested with the spring system. The maximum antenna stiffness reduction, again typically, occurred at high temperature.

The test setup checked out very well and the high and low temperature conditions were easily obtained. The change of side load was much easier to accomplish at temperature and the test setup was found to be satisfactory in all respects.

There are several advantages of compressed air for combined loading. The uniform pressure produces correct shear and moment distributions. There is no mechanical coupling, so that damping and response effects due to the loading system itself are minimized, making test responses easier to interpret. The side load can be changed rapidly and accurately with temperature effects induced in the air supply, which optimizes test time. Additionally, the loading system can be used to perform individual static side load tests.

CONCLUSIONS

The following conclusions were made on the basis of the analysis and testing program for the F-4 UHF antenna:

- Blade antennas can be located so that significant steady air loads result. These may combine with vibration over a broad temperature range. Thus, separate tests may be inadequate.
- Combined vibration/temperature/sideload tests can be developed which duplicate actual service conditions sufficiently well to duplicate service failures and evaluate design modifications. The antenna so modified in this paper has performed satisfactorily on the F-4 in service to date.
- The best method developed for applying side loading with vibration and temperature is a compressed air chamber with a non contact seal. This is recommended for future combined environment testing of blade antennas. This method is also applicable for standard individual static side load tests.
- Test requirements for externally mounted blade antennas should include combined vibration, temperature and side load testing, either as an option dependent on antenna design, or as a mandatory test.

SHOCK ISOLATION PLATFORM FOR SEASPARROW LAUNCHER

Paul V. Roberts
Raytheon Company
Missile Systems Division
Bedford, Mass.

A unique low frequency shock isolation platform is used to mount the NATO SEASPARROW Launcher aboard U. S. shock-hardened ships. The platform attenuates shock response to less than structural design loads which were used to minimize weight on smaller NATO ships and for compatibility with airborne missiles.

The platform also isolates shipboard vibration in the most critical range of launch cell and missile resonances between 14 and 30 Hz, and furnishes a lightweight convenient means of installing the launcher aboard ship.

INTRODUCTION

The NATO SEASPARROW Launcher, mounted on the platform, is shown in Figure 1, on the aft main deck of the DD963. The Launcher carries eight (8) SEASPARROW missiles and operates through 360° train and -10° to 90° elevation.

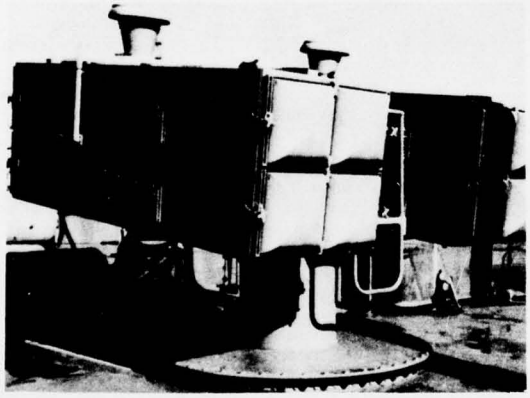

Figure 1 - Platform and Launcher on DD 963

The launcher and missile supports were designed to specified underwater shock static equivalent loads of 15 g vertical, 9 g transverse and 6 g longitudinal to the ship. These loads were taken as simultaneous combined limit loads for structural analysis purposes. The Sparrow missile is designed for flight loads and the missile attachments to the launcher are designed for aircraft carry loads which are compatible with the launcher combined limit loads.

Use of low frequency 6 to 10 Hz mounting was recommended at the beginning of the NATO SEASPARROW program as the best means of not exceeding structural design loads due to underwater shock. Analyses during program development using the DDAM method of Nav Ships 250-423-30 confirmed the desirability of a low frequency platform as indicated by the shock spectrum curves of Figure 2.

The capability of the launcher to withstand underwater shock on the recommended platform was demonstrated by successfully withstanding full Mil-S-901C underwater shock

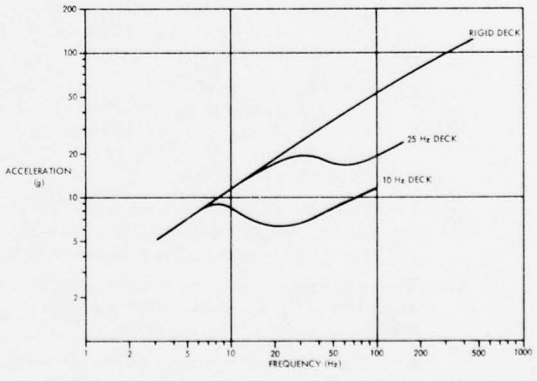

Figure 2 - Shock Spectrum versus Deck Frequency

barge tests on an engineering design model (EDM) platform. These tests were conducted at the Hi Test Lab Facility in Arvonia, VA.

The plate shock isolation platform, covered in this paper, was verified as satisfactory from a Mil-S-901C underwater shock standpoint, by DDAM analyses showing that it was superior to the EDM platform.

In addition to underwater shock verification, the paper covers platform design, development, ease of ship installation, shipboard vibration isolation, weight reduction and platform structural analyses.

PLATFORM RATIONALE

Principal engineering philosophies upon which the platform design was based are outlined as follows:

1) Provide low vertical and transverse/rocking natural frequencies between about 4 and 8 Hz to attenuate underwater shock.
   a) The platform basically protects the launcher, and missile supports to less than structural design loads, when subjected to Mil-S-901C shock.
2) Isolate Mil-Std-167 shipboard vibration at principal launch cell and missile resonances above 14 Hz.
   a) The 4 Hz to 8 Hz natural frequency range isolates vibration above 14 Hz and avoids most severe blade passage excitation, which is above 8 Hz on most ships.
3) Incorporate damping to limit response at 4 Hz to 8 Hz platform frequencies due to Mil-Std-167 inputs.
   a) Although excitation at shaft speed occurs in the 4 Hz to 8 Hz range on many ships, acceleration inputs are only ±0.05 g to ±0.2 g at these frequencies.
   b) Hydraulic dampers with C/C_c = 0.25, limit response in the 4 Hz to 8 Hz range to less than ±1/2 g.
4) The platform must be convenient to install directly to ships decks without auxiliary support structure.
   a) The platform ring, bolts or welds to a mating ring which is welded to the ships deck. Secondary supports are necessary to attach the dampers to the ship.
5) The platform must be within the launcher swing envelope for minimum deck space and be light weight for use aboard smaller NATO ships.
6) The launcher must meet all operational performance criteria when mounted on the platform, such as response times to position commands, servo stability and pointing accuracy.

PLATFORM DESIGN

The principal element of the platform consists of a 2.64 meter diameter 6061-T6 aluminum plate. The plate tapers from 7.62 centimeter thickness at the inner launcher attachment interface to 2.54 centimeter at the outer ship attachment ring. The plate and other principal platform elements are shown schematically on Figure 3.

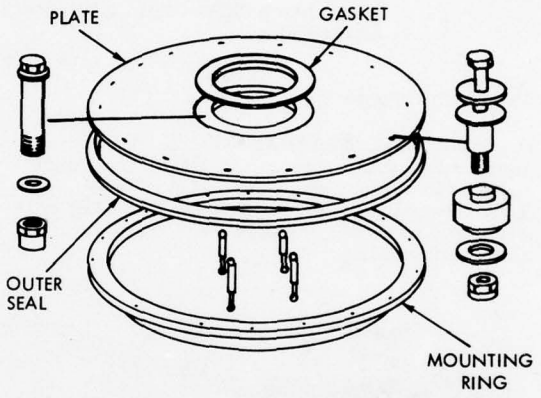

Figure 3 - NSSMS Launcher Platform

The plate is tapered for more uniform stress distribution, weight reduction wherein the thinner outer portion comprises most of the area, and for shedding sea and rain water off the upper surface. Stresses are still highest at the thicker launcher attachment interface, but the plate thickness was limited to 7.62 cm to reduce machining waste and material cost.

Parametric studies using the ASSAS finite structural element computer model described under structural analyses in Figure 14, showed that the inner to outer taper was efficient from the standpoint of maintaining high rocking moment stiffness for servo stability and pointing accuracy along with low vertical stiffness for shock isolation. The inner to outer taper was found superior to flat plates and reverse tapers from these stiffness standpoints, within allowable plate stresses.

In addition to the plate, the other major metallic element in the platform is a 1.27 cm thick steel angle ring used to support the outer plate circumference. The mounting ring is welded and bolted to a mating ring welded to the ship's deck. The deck attachment is described in more detail under shipboard installation.

A 3.18 cm thick neoprene seal is used between the lower surface of the outer plate and the mounting ring. In addition to water sealing, the neoprene seal furnishes additional down flexibility and provides a softer pinned as compared to clamped structural joint at the outer plate support. In the up direction, flexibility as well as sealing is provided by 48 neoprene bushings located below the mounting ring as shown on Figure 3.

In addition to the lower neoprene bushings, 48 silicone bushings are inserted in the plate from the upper surface to provide overall sealing as well as flexibility around the outer plate attachment bolts. The silicone material was used in the upper bushings to resist heat due to occasional rocket motor blast inpingment on the upper surface of the plate, during missile firings at high elevation angles.

From a dynamic standpoint, the neoprene seal and bushings primarily furnish flexibility in the plane of the plate for isolation of transverse and longitudinal underwater shock. The elastomeric flexibility allows about 2.2 cm of relatively soft transverse plate motion and protects elements close to the launcher base such as the slip ring assembly, which would be more directly subjected to deck plane shock.

In the principal vertical shock direction, the plate is much more flexible than the elastomeric elements and undergoes about 88 percent of the overall vertical deflection.

Forty-eight shoulder bolts are used to maintain compression on the outer neoprene seal to prevent leakage during sea state conditions. Short period seal separation would occur at response motion peaks resulting from underwater shock. The launcher base ring is attached to the platform on a 0.81 meter bolt circle by means of 2.54 cm diameter bolts. A 0.32 cm thick 70 durometer neoprene gasket is used between the launcher base and platform for sealing and to relieve stresses in the launcher base due to radial moment loading resulting from plate deflections.

The four hydraulic dampers shown in Figure 3 primarily furnish vibration damping in the vertical direction since Mil-Std-167 input accelerations are much greater at the higher vertical frequency. Little damping is needed at the lower 4.1 Hz transverse frequency since the Mil-Std-167 input is only ±0.052 g, compared to ± 0.18 g at the vertical frequency. Damping measured experimentally during dynamic tests averaged about $C/C_c = 0.25$ at the 7.6 Hz vertical frequency, compared to $C/C_c = 0.036$ at the first 4.1 Hz transverse frequency. The dampers incorporate force limiting at high underwater shock imput velocities such that the damper attachments were designed for a 2000 lb. (8896N) peak force.

DEVELOPMENT ANALYSES AND TESTS

The following principal analyses were conducted during platform development. Results of these analyses are discussed in separate sections as appropriate.

ASSAS computer parametric stress and deflection analyses

DDAM shock response analyses described in later paragraphs

NASTRAN vibration response analyses

Elastromeric element load and stiffness analyses

Structural analyses of principal elements

Static, dynamic and servo tests were conducted during development as follows.

Static Tests

1) Vertical down to 63 percent load
2) Vertical up to 49 percent load
3) Transverse/rocking to 37 percent load

Dynamic Twang Tests

1) Vertical
2) Rocking

Servo Tests

1) Response times to step commands and pointing accuracy
2) Stability gain margin
3) Response to sinusoidal frequency sweeps

Results of the static stress measurements were used to extrapolate stresses up to full underwater shock design loads. Experimental stresses varied locally from stresses predicted analytically primarily due to bolt hole cut outs. Deflections measured in the static tests were used to verify stiffness analyses and for final DDAM and vibration analyses.

Dynamic twang tests were conducted in the vertical and transverse directions to verify natural frequency and damping ch racteristics. Step release loads were suddenly applied at predicted levels by means of shear bolts.

The servo performance tests were conducted with 8, 4 and 0 missile loads on the platform, and with the launcher base rigidly attached to a concrete deck. Results of these tests showed that response times to required elevation and train angles were almost identical on and off the platform, and that transient motions were well within pointing accuracy requirements. In addition, both rate and position loop gain margins were fully satisfactory on the platform.

The elevation rocking frequency resulting from the sinusoidal frequency sweeps, reduced from 6.1 Hz hard mounted to 4.1 Hz on the platform with an eight missile load. This reduction was anticipated due to inherent platform flexibility provided for shock and vibration isolation. Train frequencies remained essentially the same both on the platform and hard mounted.

Basic dynamic information resulting from tests and analyses are summarized below for the most severe eight missile load condition.

Vertical natural frequency 7.2 Hz (shock)

Vertical natural frequency 7.6 Hz (vibration)

Vertical damping $C/C_c = 0.25$

Vertical operational travel ±4.3 cm

Maximum down vertical travel -10.2 cm

Transverse/rocking natural frequency -4.1 Hz

Transverse/rocking damping $C/C_c = 0.036$

Transverse operational travel at plate ±1.6 cm

Maximum transverse travel at plate ±2.2 cm

Predicted operational travel at cg ±3.8 cm

Elevation and train frequencies with various missile loads found during the servo test frequency sweeps are listed as follows:

No. Missiles	Elevation	Train
0	4.9 Hz	6.5 Hz
4	4.3 Hz	5.9 Hz
8	4.1 Hz	5.2 Hz

SHIPBOARD INSTALLATION

In addition to reducing equipment weight due to permitting lower shock design loads, the platform comprises a convenient lightweight method of mounting the launcher aboard ship.

Figure 4 illustrates basic advantages in installing the large 2.64 meter diameter platform on the deck compared to attaching the 0.89 meter diameter launcher base directly to the deck. The rocking stiffness R, in elevation directions normal to the deck, must be maintained for pointing accuracy and servo stability. For a given rocking stiffness R the vertical stiffness K, given by $K = 8R/D^2$, is inversely proportional to the diameter squared. With the smaller launcher diameter therefore, the deck stiffness K, for the same R, is 8.8 times higher than with the platform.

Due to the high vertical to moment stiffness without the platform, it is difficult to provide sufficient rocking stiffness for satisfactory pointing accuracy and servo stability and at the same time be sufficiently flexible in the vertical direction to protect the launcher and missiles from underwater shock.

Ship installations without the platform use additional deck structure for satisfactory operational moment stiffness but end up being too stiff vertically for Mil-S-901C underwater shock protection. A possible approach, which is inherently much heavier than the 681 kg platform, is to attach the launcher to a trunnion extending from the launcher deck to next lower deck. The trunnion provides high moment stiffness and is soft mounted in the vertical direction only, at both docks by means of leaf springs or other suitable flexures. In addition to being heavy, the trunnion takes up considerable below deck space and makes access to the launcher base difficult.

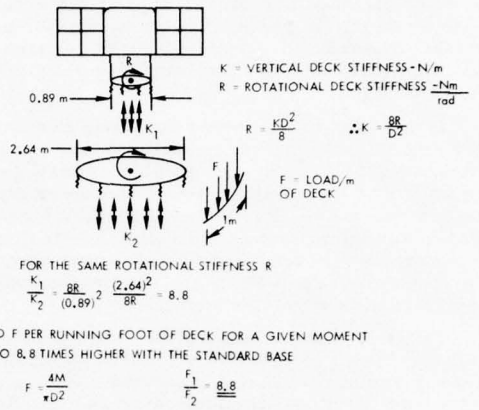

Figure 4 - Deck Loads with 0.89 m Launcher Base versus 2.64 m Dia Platform

Figure 4 also illustrates basic advantages with the larger 2.64 meter platform from the standpoint of much lower deck loads at the platform mounting ring. For a given overturning moment M the peak load F per running unit of deck length is approximated by $F = 4M/D^2$. The force F is therefore also inversely proportional to the diameter squared such that with the smaller 0.89 meter launcher stand the peak load is again 8.8 times higher than with the 2.64 meter platform.

With the lower deck loads and amount of deck structure swept by the 8.29 meter platform circumference, additional deck support structure has been found unnecessary. The ship attachment ring has therefore been welded directly to the deck and the matching platform ring has been tack welded and bolted to the deck ring. Secondary structure is needed for attachment of the four hydraulic shock absorbers.

SHIPBOARD VIBRATION

Although primarily designed for underwater shock isolation, the low 4 Hz to 8 Hz platform natural frequencies also isolate shipboard vibration in the most critical range of launcher and missile resonances between about 14 Hz and 30 Hz.

Principal advantages of the platform from a shipboard vibration standpoint are illustrated on Figure 5. Launcher rigid body vertical response to the shipboard vibration inputs of Mil-Std-167 are shown on Figure 5 both on the platform and with rigid mounting.

As indicated by the lower platform response curve, vibration isolation occurs above about 11 Hz with the 7.6 Hz platform vertical frequency and progressively improves at higher

frequencies. The upper curve for rigid mounting consists of required Mil-Std-167 input accelerations, since inputs would be applied directly to the launcher base with rigid mounting.

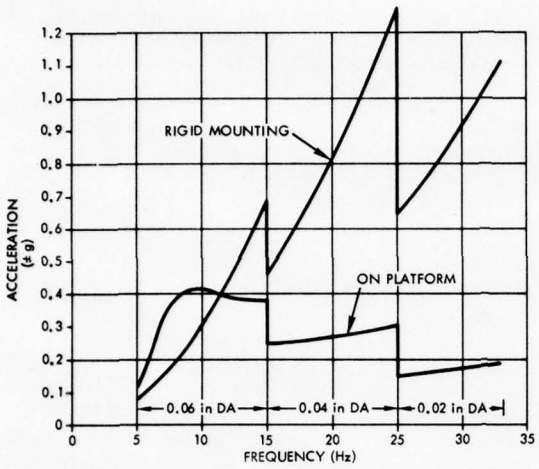

Figure 5 - Base Acceleration with Rigid Mounting and on Platform-Mil-Std-167 Input

Reference to Figure 5 shows that peak Mil-Std-167 inputs occur at 25 Hz, 33 Hz and 15 Hz. These peaks correppond to missile cantilever resonances between 20 Hz and 25 Hz, free missile resonances between 28 Hz and 33 Hz and the launch cell vertical cantilever resonance at 14 Hz to 18 Hz. When mounted on the platform, inputs to the launcher are basically attenuated about 50 percent to over 80 percent from the low to high range of these resonances.

Beefing up the launcher cell structure to raise the 14 Hz vertical frequency above 33 Hz, is questionable from a technical standpoint without prohibitive weight increase. Various methods of restraining missile body bending resonances in the launch cells also invariably lead to additional weight, complexity and interference with missile launch.

Vibration response analyses were made using the NASTRAN computer program and the launcher/missile dynamic models used for DDAM underwater shock response. These analyses were made on the plate platform discussed herein, the EDM platform and with the launcher rigidly mounted.

Results of the NASTRAN vibration analyses are illustrated on Figure 6, which shows response of lump mass upper outboard missile 1 to Mil-Std-167 inputs. It is seen that response on the plate and EDM platforms is much more favorable than rigid mounting and that response on the plate platform is most favorable. The effect of the higher damping used with the plate platform in reducing response at the 7.6 Hz vertical resonance is also evident on Figure 6.

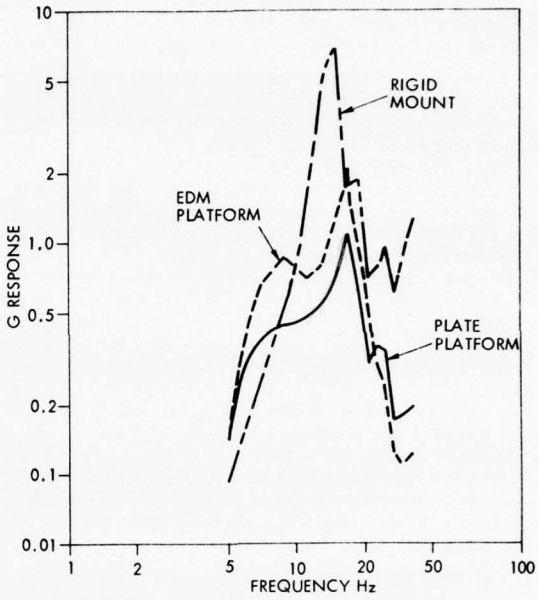

Figure 6 - Missile 1 Response Mil-Std-167 Input

The ability of the launcher and missiles to withstand Mil-Std-167 vibration on the EDM platform was verified during tests at Ogden Technology Labs using a large hydraulic shaker. Since the NASTRAN analyses indicate more favorable vibration characteristics on the plate than on the EDM platform the launcher and missiles should satisfactorily withstand Mil-Std-167 conditions on the plate platform.

Inasmuch as the plate platform is highly damped in the vertical direction with C/C_C = 0.25, calculated response at the 7.6 Hz vertical frequency with the ±0.18g Mil-Std-167 input would be approximately ±0.4g. Since no internal resonances occur in the region of 7.6 Hz, response of the overall launcher missile assembly should not exceed ±1/2g at the platform vertical resonance.

The transverse/rocking resonance on the platform of 4.1 Hz with eight missiles, is not nearly as well damped as the vertical 7.6 Hz resonance. Since the Mil-Std-167 input at this lower frequency is only ±0.052g however, response accelerations would still be on the order of ±1/2g with damping measured during dynamic tests.

Vibration on most ships is well below Mil-Std-167 levels, especially during normal cruise conditions. On ships with shaft rotation speeds in the region of 4 Hz, low level transverse vibration could occur on upper launcher extremeties up to about 0.25 cm double amplitude. The peak ±1/2g Mil-Std-167 response level, corresponding to about 1.5 cm double amplitude

would only be anticipated during severe maneuvers such as high speed turns and backing down. Similar levels could also occur due to ship damage, especially to the shafting and blades.

Hard mounted vibration tests conducted at the Raytheon Sudbury Facility, wherein Mil-Std-167 levels were applied at the launcher base, verified the launcher and missiles to withstand Mil-Std-167 levels rigidly mounted. Two series of tests were conducted. The first up to 9 Hz verified the launcher and missiles for installation on AOR and AE type ships having blade passage frequencies below 7 Hz. The second series of tests used auxiliary missile snubbing devices for overall Mil-Std-167 verification.

UNDERWATER SHOCK VERIFICATION

Verification of the shock isolation platform to protect the launcher and missiles from Mil-S-901C shock, was based on DDAM analyses showing that the platform would furnish better shock protection than an engineering design model, EDM, platform on which the launcher passed full underwater shock tests.

The EDM platform is shown in the photograph of Figure 7, as set up for underwater shock barge tests at the Hi Test Lab Facility in Arvonia, VA. The platform structure consisted of two longitudinal and two lateral, 27.6 cm depth by 3.66 meter length, wide flange steel I-beams about 0.91 meters apart. The launcher was bolted to a 3.18 cm thick steel plate welded over the I-beam center section. The four ends of the structure were boxed in by means of 30.5 cm depth channels welded to the I-beams.

Twenty Nichols Engineering sandwich mounts were installed between the four ends of the platform and deck by means of 0.91 meter length steel angle fittings. The five mounts at each of the four ends of the beam structure were oriented at 45 deg in order to reduce vertical compared to lateral and longitudinal stiffness and to partially decouple translational and rotational modes.

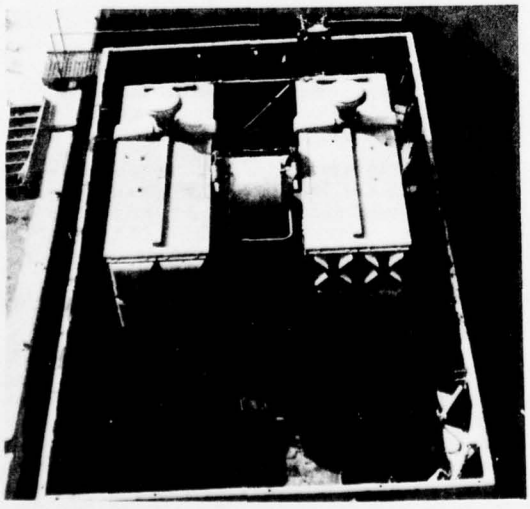

Figure 7 - EDM Launcher Set-Up On Barge

A comparison of characteristics of the production plate and EDM platform, which principally effect underwater shock isolation, is tabulated below. The vertical and transverse/rocking frequencies are lower on the plate than on the EDM platform and the plate platform is more highly damped. All of these factors are more favorable from a shock isolation standpoint.

	DISC	EDM
VERTICAL FREQUENCY	7.2 Hz	7.8 Hz
VERTICAL C/C_C	0.25	0.1
ROCKING FREQUENCY	4.1 Hz	7.4 Hz
VERTICAL K	13.8 (10) ^{6}N/m (79 000 lbs/in)	25.7 (10) ^{6}N/m (147,000 lbs/in.)
TRANSVERSE K	7.2 (10)^{6}N/m	16.5 (10) ^{6}N/m
ROCKING R	10.6 (10) ^{6}Nm/rad	45.2 (10) ^{6}Nm/rad
WEIGHT	7037 kg (15,500 lb)	8989 kg (19,800 lb)

The 1500 lb. (681 kg) plate platform is much lighter than the 5800 lb. (2633 kg) EDM platform as indicated above. Stiffnesses in principal directions, also listed above, show the same trend as natural frequencies, but cannot be compared directly, especially in transverse/rocking modes, since they are effective at different locations.

Results of shock isolation analyses described in the next section under DDAM Analyses, verify lower shock transmission with the plate compared to EDM platform at all locations, particularly on the missiles and launcher extremities. Since Mil-S-901C shock tests were successfully passed on the EDM platform, the plate platform was therefore shown to be acceptable from an underwater shock standpoint.

DDAM ANALYSES

The Dynamic Design Analysis Method (DDAM) is specified by the Navy in Nav Ships 250-423-30 for analytical verification of underwater shock integrity of shipboard equipment. The DDAM analytical procedure was therefore used for both shock and vibration response analyses during development of the NSSMS launcher as well as for the shock isolation platform.

The method was initially programmed on a UNIVAC 1108 computer for launcher natural frequency and mode shape analyses and for shock response using a separate program format. Both of these programs were converted to a CDC 6700 computer for analyses of the shock isolation platform.

The dynamic models used in the DDAM analyses consisted of a sixteen degree-of-freedom vertical model, and a 25 element transverse/rocking model. The vertical model is shown in Figure 8 as an example. The 25 elements in the transverse model include 9 transverse, 9 rotational and 7 missile/cell vertical elements. The eight missiles were separate elements in the vertical model but similar port and starboard missiles were combined into four elements in the transverse/rocking model.

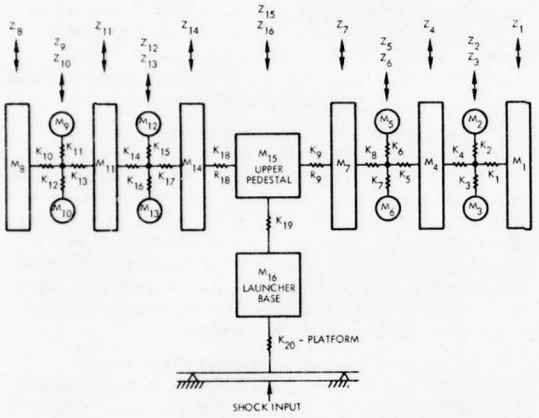

Figure 8 - Vertical Shock Model

Primary concentration in the DDAM analyses was in the vertical direction. Since the plate platform is much softer in transverse/rocking directions than the EDM platform, more favorable shock isolation characteristics are predictable in the transverse direction. Calculations also indicated response accelerations well below the 6g minimum transverse unidirectional load allowed by the DDAM procedure.

Influence coefficients were calculated for the launcher and missiles during EDM launcher development. A structural computer program designated STIFF was used to calculate cell structural deflections and was found very accurate without joint degradation factors. The missiles were treated separately as distributed bodies on their supports and then lumped into single elements for equivalent loading. Elements such as the stand, pedestal, truss, gear system and bearings were analyzed separately and utilized appropriate joint reduction factors. Influence coefficients were also updated based on experimental natural frequency and mode information obtained during EDM launcher shock and vibration tests.

The accuracy of the dynamic model and influence coefficient mass inertia matrices in representing the stiffness and inertia of the launcher, was demonstrated by experimental frequencies, found during hard mounted launcher vibration tests, which agreed with analytically predicted frequencies within 0.5 Hz.

A total of 11 frequencies with corresponding modes were used in the DDAM analyses such that full launcher dynamic mass was represented. In addition to the 79,000 lbs/in. (13.8 $(10)^6$ N/m) plate platform stiffness found during experimental tests, stiffnesses of 17.5$(10)^6$ N/m, 21.9$(10)^6$ N/m and 26.3$(10)^6$ N/m were used in the analyses for parametric purposes. The EDM platform which was compared analytically by the DDAM method had a stiffness of 147,000 lbs/in. (25.7$(10)^6$ N/m). Inputs specified by NRL 1396 of Reference 2, were used in the DDAM analyses.

Figure 9 shows a comparison of predicted response at the launcher base (element 16 in Figure 9) and the inboard and outboard missiles (elements 5, 6 and 2, 3 respectively) plotted versus the first mode frequency of the launcher system on the EDM barge test platform and on the plate platform. The results indicate that the plate platform provides better attenuation of underwater shock than the EDM platform particularly on the missiles and launch cells. The dependence of shock isolation on the fundamental frequency is inherent in this data, and was further supported by the parametric studies with various platform stiffnesses.

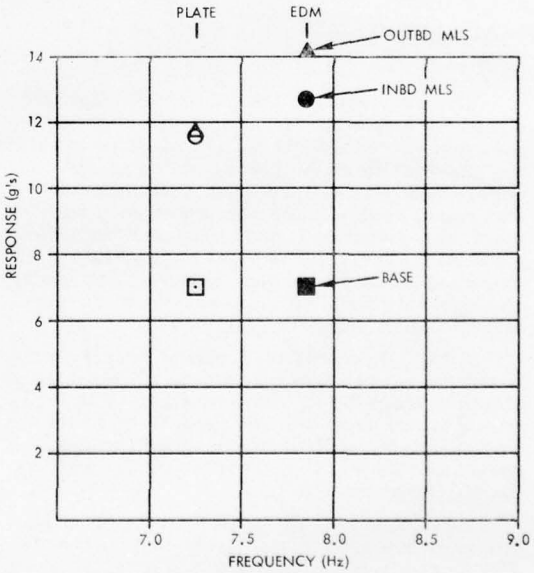

Figure 9 - DDAM Response

DDAM LOADS

Resulting design loads at each element obtained from the DDAM analyses, on both the EDM and plate platform, are listed in Table 1. Loads obtained from the EDM platform barge tests, described in the next section, which were used for structural analyses, are also listed in Table 1.

Table 1

DDAM versus Barge Test Vertical Loads

ELEMENT	WEIGHT KG	EDM DDAM G	PLATE DDAM G	EDM BARGE G
1	152	10.5	9.2	8.0
2	282	14.2	11.5	10.1
3	282	14.2	11.5	10.1
4	229	7.7	7.2	4.4
5	282	12.5	11.4	9.3
6	282	12.7	11.5	9.3
7	438	7.2	7.2	7.8
8	152	10.5	9.2	8.0
9	282	14.2	11.5	10.1
10	282	14.2	11.5	10.1
11	229	7.7	7.2	4.4
12	282	12.5	11.4	9.3
13	282	12.7	11.5	9.3
14	438	7.2	7.2	7.8
15	1927	7.3	7.3	7.8
16	535	7.1	7.0	8.9
PLATFORM LOAD $= \frac{\Sigma WG}{W}$		9.6	8.8	8.3

The comparative DDAM loads in Table 1 show about nine percent lower shock loads on the plate than the EDM platform, substantiating the superiority of the plate platform from an underwater shock standpoint. The DDAM structural design loads also show good agreement with structural loads obtained from the EDM barge tests. The EDM barge loads averaged about 86 percent of the DDAM loads on the EDM platform and loads showed consistent trends between elements.

A total down vertical load of 8.8g referred to the overall 14,000 lbs launcher weight was obtained from the DDAM analyses. The load was obtained from the weight data in Table 1, by multiplying each element weight by the design G load and then dividing by the 14,000 lbs (6356 kg) total weight.

Resulting overall loads from the DDAM analyses are 8.8g vertical and 6g transverse. The 6g transverse load is the least allowed by DDAM in the transverse direction and was used since preliminary checks indicated lower loads from the analytical procedure.

The DDAM procedure does not require summation of vertical and transverse loads since as noted previously, peak shock responses in the two directions at various locations do not occur simultaneously. A conservative procedure with respect to the 8.8g vertical and 6g transverse loads is to determine stress for the 8.8g unidirectional peak as well as for the 6g peak and then use an SRSS resultant stress such that:

$$\sigma = \sqrt{(\sigma_{8.8g})^2 + (\sigma_{6g})^2}$$

The peak stress using this approach was close to the stress using combined EDM platform barge test loads discussed in the next section.

BARGE LOADS

Underwater shock loads on the EDM launcher and missiles during Mil-S-901C barge tests were used for structural analyses of the plate platform. This was considered conservative since it was shown by DDAM analyses that about 9 percent lower shock loads would occur on the plate platform.

The Mil-S-901C test requires that the launcher with 8 missiles be mounted on the 28 x 16 ft (8.5 x 4.9 m) floating shock platform as shown on Figure 7, and then be subjected to a 27.2 kg explosive charge suspended at a water depth of 7.32 m for each of five shots. Horizontal distances to the charge from the side of the barge along its transverse centerline, are 18.3, 12.2, 9.1, 7.6 and 6.1 meters respectively for each of the five shots.

Shock inputs are progressively more severe at the closer distances with the closest 6.1 meter standoff being most severe. This is shown on Figure 10 by vertical velocity histories measured on the barge for the five shots. Velocities at the launcher base were substantially less than on the barge, varying from 26 percent at the 18.3 meter standoff to 57 percent at the closest 6.1 meter standoff.

Acceleration data were measured versus time through the underwater blast response period at 17 locations including the launcher base, the upper pedestal structure, extremities of cell structure both toward and away from the blast and both inboard and outboard missiles.

Since shock response peaks occur at different times at various locations in the vertical direction and at still different times in the transverse direction, detailed analyses of the shock response data are required to determine maximum simultaneous loads on the platform.

Acceleration time histories measured on the launcher and missiles in the vertical direction for the most severe 6.1 meter standoff charge, are plotted on Figure 11. Similar acceleration time histories in the transverse direction are plotted on Figure 12. It is evident from these data that both vertical and transverse peak accelerations are reached at the launcher base and pedestal first, and that peaks on the cell structure and on the missiles occur considerably later. Vertical and transverse peaks at the same locations also generally occur at different times.

The approach used to determine the maximum simultaneous vertical plus transverse load on the EDM platform, from the data on

AD-A074 701 NAVAL RESEARCH LAB WASHINGTON DC SHOCK AND VIBRATION--ETC F/G 20/11
THE SHOCK AND VIBRATION BULLETIN. PART 3. STRUCTURE MEDIUM INTE--ETC(U)
SEP 79

UNCLASSIFIED BULL-49-PT-3 NL

2 OF 2
ADA 074701

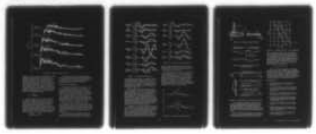

END
DATE FILMED
11 -79
DDC

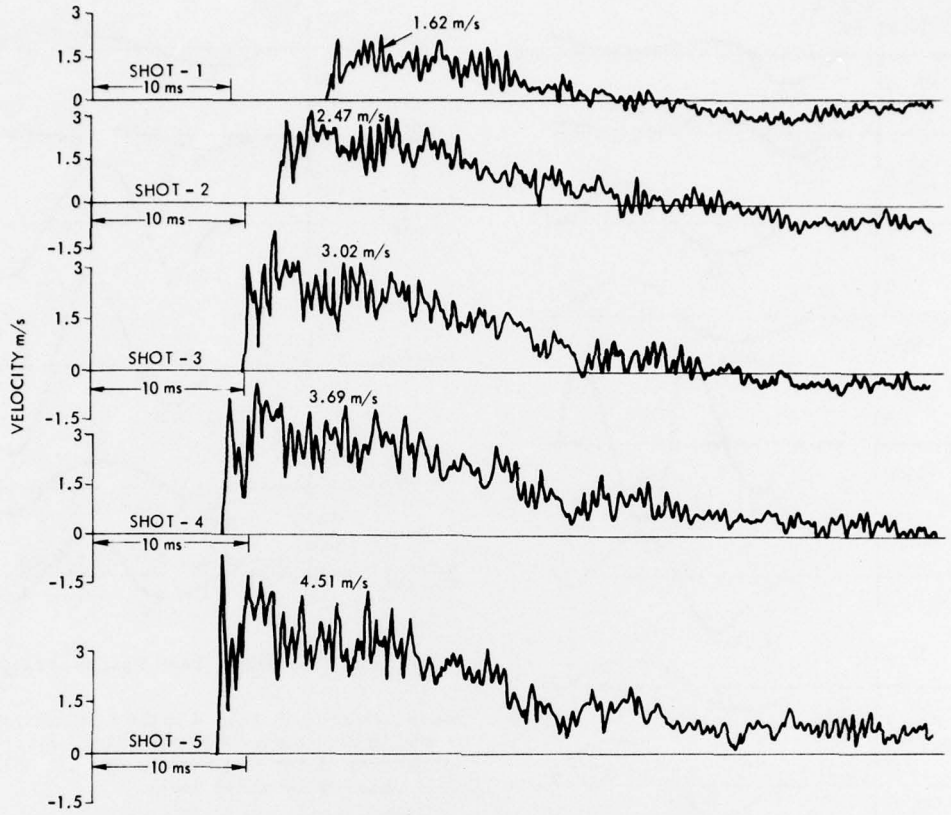

Figure 10 - Barge Vertical Velocity

Figures 11 and 12, was to determine the overall load acting on the platform at each instant through the blast period. The instantaneous g load at each location was multiplied by the effective weight at that location for all launcher missile weight elements. The sum of the element weights, times their accelerations was then divided by the total weight W to obtain the overall load acting on the platform based on the launcher missile weight. The element weights used in this analysis are the same as listed in Table 1 for the DDAM analyses.

$$G = \frac{\Sigma W_n G_n}{W}$$

Results of the barge test loads analyses are shown on Figure 13, in terms of the overall launcher vertical and transverse g loads with time, during the peak shock load period. The maximum load combination is a peak vertical shock load of 4.5g which acts simultaneously with a transverse load of 4.6g. Adding the 1g static weight acting down to the 4.5g dynamic load gives the following simultaneous underwater shock loads on the EDM platform:

Vertical	5.5g
Transverse	4.6g

Since the plate platform would undergo lower shock loads than the EDM platform, based on DDAM analyses, the above EDM experimental loads were considered conservative for structural design of the plate platform.

STRUCTURAL ANALYSIS

The ASSAS computer model of Figure 14 was used for early parametric studies to optimize the platform plate and for structural analyses of the final configuration. Elements were taken in six layers throughout the plate as well as in the launcher base and outer mounting ring. Smaller elements were taken in the region of plate, launcher and ring interfaces. The effect of gaskets, such as between the plate and launcher base, was considered by softening elements immediately adjacent to the plate.

Deflection analyses indicated that the tapered plate, 7.62 cm at the center and 2.54 cm at the outer periphery provided the soft vertical and sufficiently high moment stiffnesses desired. A sketch of plate deflection patterns under down vertical and rocking moment loads is shown in Figure 15.

Stress analyses of the platform were conducted under the 5.5g vertical and 4.6g transverse rocking loads developed in the previous

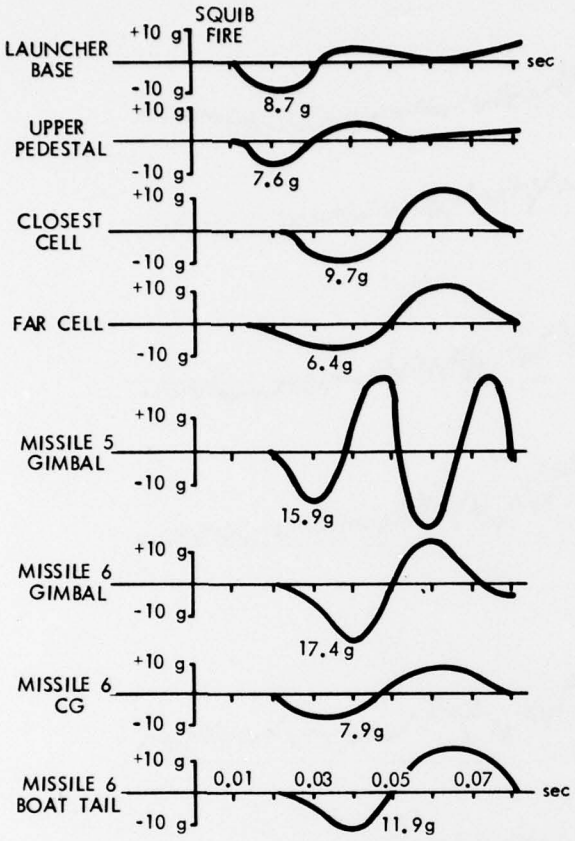

Figure 11 - Barge Test Vertical g's

section under barge loads. Calculated radial and tangential stress distributions versus plate radius, are shown in Figure 16, due to the axial and moment loads. It is seen that tangential stresses are highest, for both type loads and that peak stresses occur in the region of the launcher bolt circle.

The computer model considered axisymmetric geometry, and did not specifically take the plate bolt holes or localized introduction of loads through the bolts, into consideration. Strain gauge data, measured during static tests in critical areas of the launcher bolt circle, were therefore used for plate structural verification under maximum underwater shock loads. Experimental stresses were less than calculated at the bolt centerline but were higher just forward and aft of the bolts due to load transfer resulting from the bolt clamping action.

In addition to the plate, structural analyses were made on other principal platform elements such as the outer steel angle ring, the launcher base, 2.54 cm launcher hold down bolts, 1.27 cm shoulder bolts and damper attachments. Stiffness and bearing load analyses of the elastomeric seals and bushings were also conducted and found satisfactory. Analyses were also

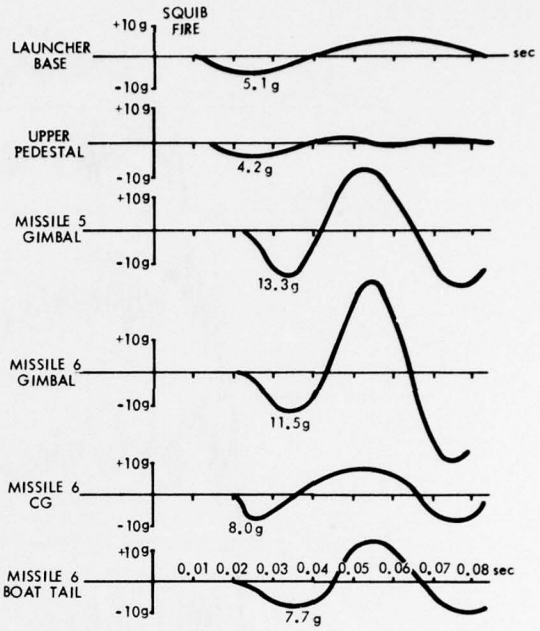

Figure 12 - Barge Test Transverse g's

made to verify that peak loads due to other environments such as green water, gun blast, vibration and sea state conditions did not exceed underwater shock loads.

With the peak 5.5g vertical and 4.6g transverse underwater shock loads, considering elastic material behavior, a peak combined stress of 306,100Pa at the 14.5 inch (35.8 cm) radius was obtained from the platform static test strain gauge data. This point, noted on Figure 17, is below the 317,200Pa elastic allowable and well below the 427,500Pa modulus of rupture allowable considering some plastic deformation of the 6061 T6 material.

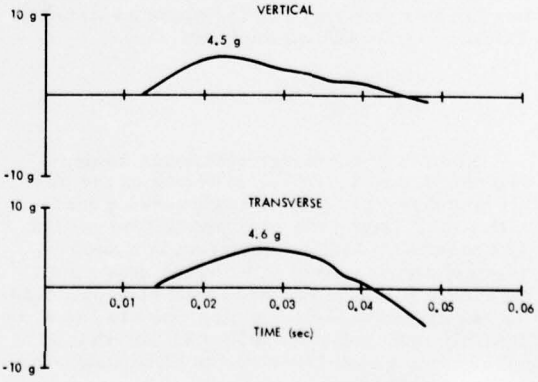

Figure 13 - Barge Test Load Summary

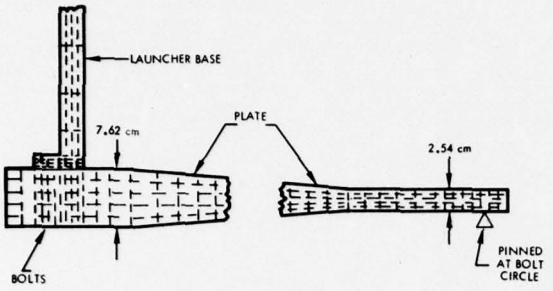

Figure 14 - AASAS Computer Model

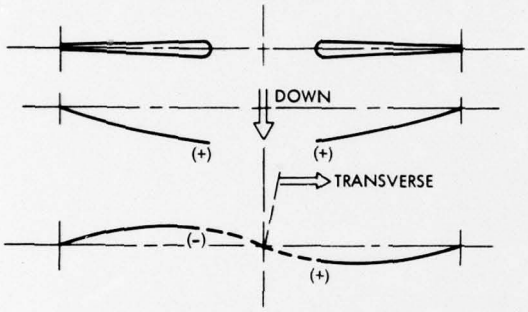

Figure 15 - Deflections Due Down and *Transverse Loads*

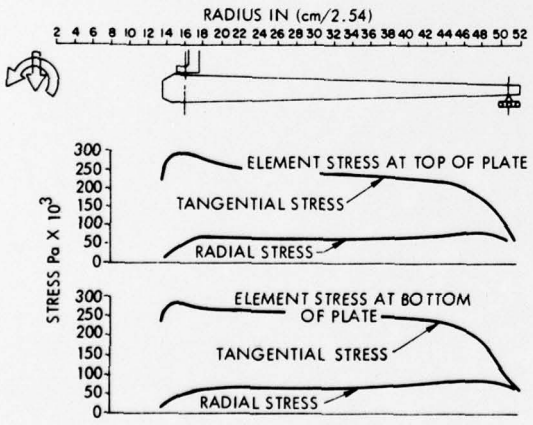

Figure 16 - Combined Load - Moment and Axial

It is evident from Figure 17 that stresses due to the unidirectional 8.8g vertical and 6g transverse DDAM loads would be below the 317,200Pa allowable. The SRSS resultant of 308,900Pa using the DDAM 8.8g and 6g stresses is close to the stress using the combined barge loads.

The 317,200Pa plate allowable of Figure 17 is based on material certification data obtained from Aluminum Company of America for the

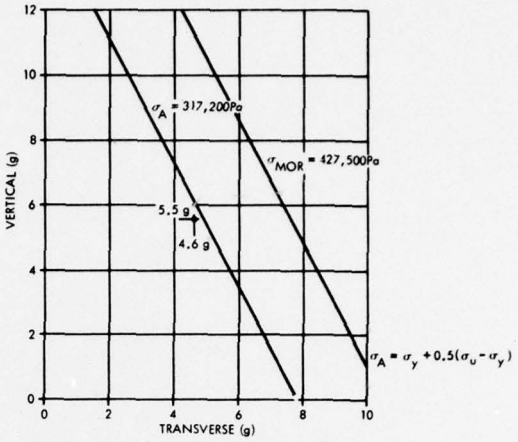

Figure 17 - Maximum Stress versus Allowable

6061 T6 plate material used in the platform. The certification data indicates minimum stress allowables of σ_u=332,300Pa ultimate, σ_y = 302,000Pa yield and 13 percent to 15 percent elongation. For shock applications involving short period dynamic loads, a stress allowable σ_A between yield and ultimate is allowed as follows. The factor F = 0.5 for typical plate cross sections.

$$\sigma_A = \sigma_Y + F\,(\sigma_u - \sigma_y)$$

From a practical standpoint, the higher allowable of σ_A = 427,500Pa could be used for the plate configuration. This higher allowable is based on the modulus of rupture approach wherein major unyielded areas of the plate prevent significant permanent deformations due to localized yielding in small surface areas.

REFERENCES

(1) Nav Ships 250-423-30, "Shock Design of Shipboard Equipment Dynamic Design Analysis Method", May 1961.

(2) G. O'Hara and R. Belsheim, NRL Memorandum Report 1396, "Interim Design Values for Shock Design of Shipboard Equipment", February 1963. (Confidential)

(3) Enclosure (1) to NRL letter 6260-7:ROB:kep, "Preliminary Shock Design Criteria for Floating Shock Platform", 18 February 1964.

(4) Enclosure (1) to NRL letter 8440-114:ROB:kep, "Measured Rigid-Body Motions of the Floating Shock Platform for Testing Heavyweight Shipboard Equipment", 1969.

(5) G. O'Hara and P. Cunniff, NRL Report 6002, "Elements of Normal Mode Theory", November 1963.

(6) Military Specification, "Shock Tests, H.I. (Hi Impact) Shipboard Machinery, Equipment and Systems, Requirements for U.S. Navy", Mil-S-901C, 15 January 1963.

(7) Technical Memorandum NS-TM-108, "NSSMS Launcher Platform Verification Analysis", 10 May 1976 (Raytheon).

*U.S. GOVERNMENT PRINTING OFFICE : 1979 0-281-484/97